SEARCH FOR DARK MATTER AND W' IN THE FINAL STATE WITH ONE MUON AND MISSING TRANSVERSE ENERGY WITH CMS

VON

SÖREN ERDWEG

MASTERARBEIT IN PHYSIK

VORGELEGT DER
FAKULTÄT FÜR MATHEMATIK, INFORMATIK UND
NATURWISSENSCHAFTEN DER RWTH AACHEN

IM DEZEMBER 2013

ANGEFERTIGT IM
III. PHYSIKALISCHEN INSTITUT A

BEI
PROF. DR. THOMAS HEBBEKER

ZWEITGUTACHTER
PROF. DR. CHRISTOPHER WIEBUSCH

ABSTRACT

This thesis describes the search for new physics in the transverse mass spectrum of events with one muon and missing transverse energy in the final state of proton-proton collisions. The studied data were recorded 2012 with the CMS detector at the LHC accelerator at a center of mass energy of $\sqrt{s} = 8\,\text{TeV}$ and correspond to an integrated luminosity of $20\,\text{fb}^{-1}$. The transverse mass spectrum of the observed data was compared to a simulation of Standard Model processes.

As no indication for new physics beyond the Standard Model of particle physics was found, exclusion limits were set. Two models of new physics were studied in this analysis, first the production of new heavy charged vector bosons W', which decay into a muon and a neutrino and second the pair production of particles χ which are Dark Matter candidates, which recoils against a Standard Model W boson that decays into a muon and a neutrino.

On the W' model a mass limit of $M_{W'} > 3.35\,\text{TeV}$ was set, while on the interaction scale Λ of the Dark Matter pair production, different limits from $\Lambda > 300\,\text{GeV}$ to $\Lambda > 1050\,\text{GeV}$ were set. Limits were also set on the proton-proton cross section and the Dark Matter-nucleon cross section for the Dark Matter model.

ZUSAMMENFASSUNG

Diese Arbeit beschreibt die Suche nach neuer Physik im transversalen Massenspektrum von Ereignissen mit einem Myon und fehlender Transversalenergie im Endzustand von Proton-Proton Kollisionen. Die untersuchten Daten wurden 2012 mit dem CMS-Detektor am LHC-Beschleuniger mit einer Schwerpunktsenergie von $\sqrt{s} = 8\,\text{TeV}$ aufgenommen und entsprechen einer integrierten Luminosität von $20\,\text{fb}^{-1}$. Das transversale Massenspektrum der beobachteten Daten wurde mit Simulationen von Standardmodell-Prozessen verglichen.

Da keine Hinweise auf neue Physik gefunden wurden, wurden Ausschlussgrenzen gesetzt. Zwei Modelle für neue Physik wurden in dieser Arbeit untersucht, erstens die Produktion von neuen schweren geladenen Vektorbosonen W', die in ein Myon und Neutrino zerfallen, und zweitens die Paarproduktion von Teilchen χ die Kandidaten für Dunkle Materie sind und zur Impulserhaltung die gleichzeitige Produktion eines Standardmodell W Boson , dass dann in ein Myon und Neutrino zerfällt.

Auf das W' Modell wurde eine Massengrenze von $M_{W'} > 3.35\,\text{TeV}$ gesetzt und auf die Wechselwirkungsskala Λ der Paarproduktion von Dunkler Materie Teilchen wurden verschiedene Grenzen von $\Lambda > 300\,\text{GeV}$ bis zu $\Lambda > 1050\,\text{GeV}$ gesetzt. Auch auf die Proton-Proton und Dunkle Materie-Nukleon Wechselwirkungsquerschnitte wurden Grenzen gesetzt.

CONTENTS

1 INTRODUCTION

The Standard Model of particle physics is a very successful theory which withstands every test of measurement since its finalization in the 1970s, but leaves some open questions. To answer these questions, it is worthwhile to search for physics beyond the Standard Model, in which this analysis is a small part.

This thesis presents the results of the search for new physics in proton-proton collision events, recorded with the CMS detector at the CERN LHC accelerator. The data was recorded in 2012 at a center of mass energy of $\sqrt{s} = 8\,\text{TeV}$ and corresponds to an integrated luminosity of $20\,\text{fb}^{-1}$. In this thesis, the results of the analysis of collision events with one high energy muon and missing transverse energy are presented. The results are interpreted in two new physics models. The first model is the production of new heavy charged gauge bosons W' which decay into a muon and a neutrino. The second model is the pair production of two undetectable Dark Matter candidate particles χ, recoiling against a Standard Model W which decays to a muon and a neutrino.

This analysis is the latest in a series of W' analyses started with an analysis at the Tevatron [1, 2] in the electron channel at a center of mass energy of $\sqrt{s} = 1.96\,\text{TeV}$ which resulted in a W' mass limit of $M_{W'} > 1.12\,\text{TeV}$. With the first LHC collision data at $\sqrt{s} = 7\,\text{TeV}$ in 2010 [3, 4] a mass limit of $M_{W'} > 1.4\,\text{TeV}$ was derived, and was improved in 2011 [5] to $M_{W'} > 2.5\,\text{TeV}$. The analysis of 2012 data presented in this thesis was published in combination with the complementary analysis in the electron channel in Ref. [6], where also other possible interpretations of the single muon plus missing transverse energy like helicity non conserving contact interactions or split-universal extra dimensions are studied.

For the Dark Matter model this is the first analysis in the muon plus missing transverse energy final state and it was published in combination with the electron channel in Ref. [7].

This thesis is structured by first introducing the experimental setup of the LHC accelerator and the CMS detector (Sec. 2). In Sec. 3 the theoretical aspects of the analysis are summarized, starting with the Standard Model (Sec. 3.1) which describes the background for this analysis. This is followed by the open questions of the Standard Model which lead to theories beyond the Standard Model, which are studied in this analysis, W' and Dark Matter (Sec. 3.2). The object reconstruction, identification and correction of the muon and missing transverse energy are explained in Sec. 4. In the following section (Sec. 5) the data and simulation samples used for this analysis are introduced. In Sec. 6 the kinematic selection of signal events is explained which results in the final transverse mass distribution. The systematic uncertainties and the procedure to calculate limits from the transverse mass distribution is also introduced. The limits on the W' and Dark Matter theory are summarized in Sec. 7. Conventions that are used in this analysis are explained in Sec. A.4 in the Appendix.

2

EXPERIMENTAL SETUP

In this section the experimental setup for this analysis is summarized. The first part gives a short introduction in the LHC accelerator (section 2.1) and the second part introduces the CMS detector and its infrastructure (section 2.2).

2.1 LHC

The Large Hadron Collider (LHC) is the particle accelerator with the highest beam energy in the world and is located at the European center for nuclear research (CERN) near Geneva, Switzerland. Detailed information on the accelerator can be found in Ref. [8].

At the beginning of the accelerator chain, protons are produced by ionizing hydrogen. The protons are then accelerated in bunches first by a linear accelerator (LINAC 2) and then by three ring accelerators (BOOSTER, PS, SPS) before they are accelerated in the LHC to their final energy of 4 TeV (in 2012) and brought to collision at 4 points in the LHC ring. An overview of this whole accelerator chain and also the other beam targets, users and sources at CERN are shown in Fig. 2.1.

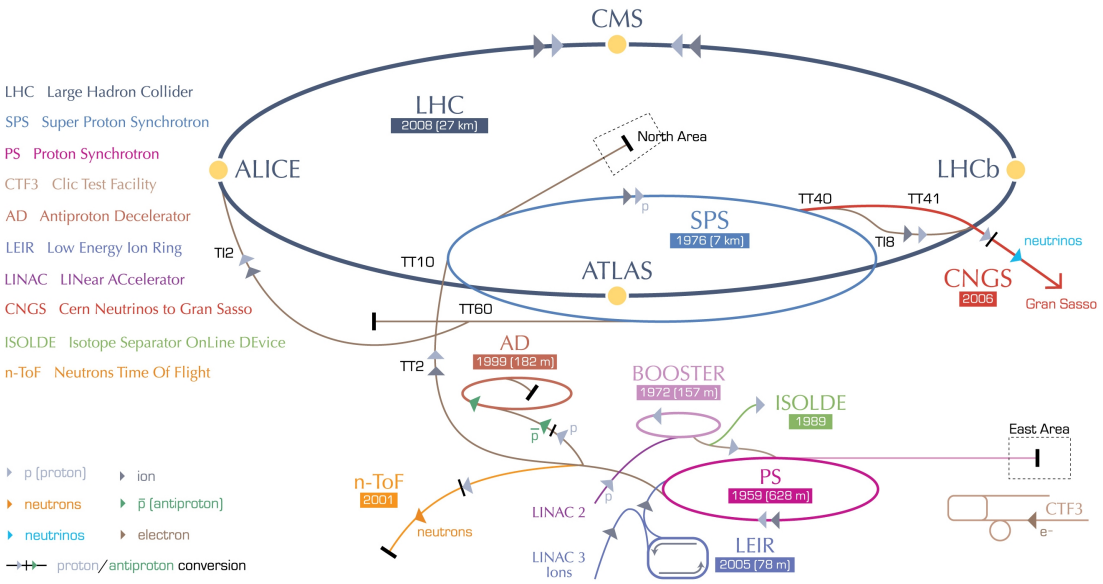

Figure 2.1: CERN accelerator complex: shown are the different accelerators at CERN, their year of construction and for ring accelerators their circumference [9].

At one of the collision points of the LHC the CMS detector is located, which recorded the data used in this analysis. In 2012, the LHC delivered an integrated luminosity of $\sim 24\,\mathrm{fb}^{-1}$ (from which $20\,\mathrm{fb}^{-1}$ were recorded) at a center of mass energy of $\sqrt{s} = 8\,\mathrm{TeV}$ of proton-proton collisions which is the dataset in this analysis. This data was recorded with a peak instantaneous luminosity of $7.67 \times 10^{33}\,\mathrm{cm}^{-2}\mathrm{s}^{-1}$ and a bunch spacing of 50 ns, which results in many collisions (mean $\sim$ 16) at the same bunch crossing. These interactions occur in addition to the interesting physics events and are called pile-up events.

2.2 CMS

The Compact Muon Solenoid (CMS) is a multi-purpose detector at the LHC. An overview picture of CMS is shown in Fig. 2.2 (for the definition of the coordinate system see Sec. A.4.1). CMS is designed to have a large geometric coverage of the interaction region and is divided into a barrel region and two endcaps. This general design concept is driven by the choice of the magnet which bends the tracks of charged particles to measure there momentum. The magnet in CMS is a superconducting solenoid which produces a homogenous magnetic field parallel to the beam direction at a field strength of 3.8 T inside the solenoid. Inside the solenoid is first, nearest to the interaction point, the silicon tracker (section 2.2.1) followed by the electromagnetic calorimeter (ECAL) and the hadronic calorimeter (HCAL). The tracker is used to measure the tracks of charged particles to reconstruct the momentum, the calorimeters are used to measure the energy of particles, via electromagnetic showers in the ECAL and via hadronic showers in the HCAL. Outside of the solenoid are the iron layers of the return yoke for the magnetic field. Integrated into the iron layers is the muon system (section 2.2.2) to detect muons which are the only Standard Model particles which can reach this part of the detector.

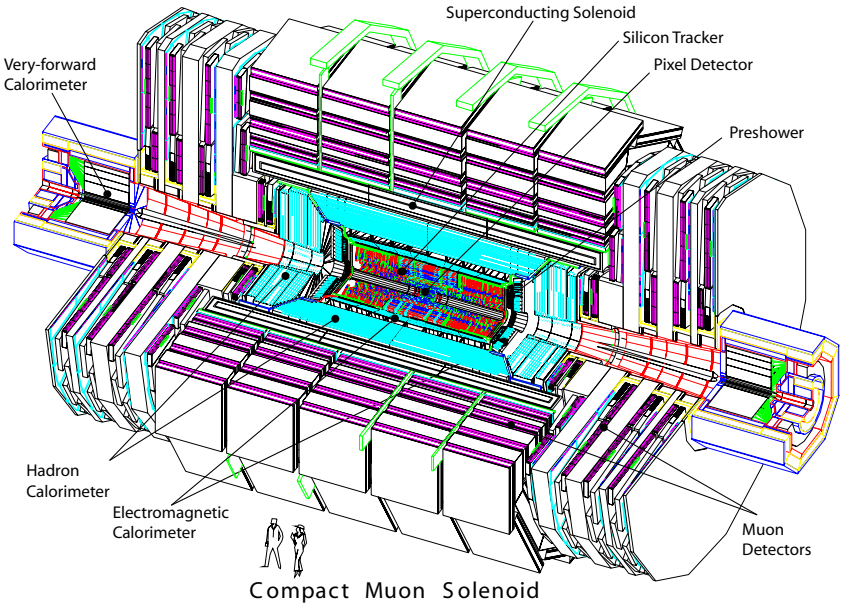

Figure 2.2: Overview picture of CMS: The different sub-detectors of CMS are shown [10].

For this analysis, especially important are the capabilities of CMS to detect and reconstruct muons (reconstructed in the tracker and muon system) and missing transverse energy (the energy imbalance in the transverse plane, reconstructed with the whole detector). This sub-detectors are therefore introduced in the following sections. This summary is based on Ref. [10].

2.2.1 *Tracker*

The silicon tracker is divided in a barrel and two endcaps and covers a polar angle of $|\eta| < 2.5$ and extends from a radial distance of 4.4 cm from the interaction point to 1.1 m. It is

further divided into three layers of pixel detector to get precise track information close to the interaction point and about 10 layers (depending on η) of silicon strip detector surrounding the pixel detector where, due to lower occupancy, a high granularity is not necessary. The tracker layout in the $r-z$-plane is shown in Fig. 2.3.

The whole tracker is based on silicon detector technology which is fast, measures precisely hits from charged particles and works in this area in spite of the high radiation level. The momentum resolution for a muon with $p_T = 100\,\text{GeV}$ is about 1.5 % (for $\eta \sim 0$) to 3 % (for $\eta \sim 2$).

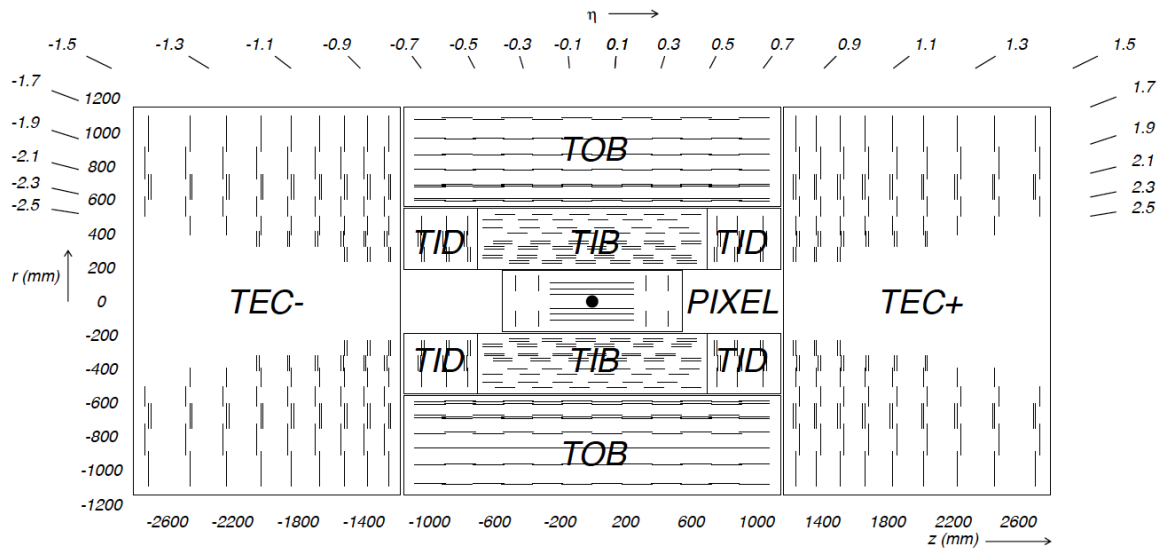

Figure 2.3: Silicon tracker layout: In the $r-z$-plane, the different sub-detector parts are shown: Tracker End-Caps (TECs), Tracker Outer Barrel (TOB), Tracker Inner Disks (TIDs), Tracker Inner Barrel (TIB) and the Pixel detector [10].

2.2.1.1 *Pixel Detector*

The pixel detector is the sub-detector closest to the interaction point, and is used to get the first hits for a track reconstruction, which are important for the reconstruction of possible secondary vertices or to match tracks to a specific vertex. Close to the interaction point the flux of particles is very high ($1\,\text{MHz/mm}^2$ for the first pixel layer at design luminosity). In order to avoid two particles hitting the same detector element, it has to have a high granularity. This granularity is achieved by using pixel detectors which can resolve a hit in three dimensions (η and ϕ plus the position r of the pixel sensor) and a pixel size of $100 \times 150\,\mu\text{m}^2$. The pixel detector consists out of 3 barrel layers and two endcap disks on both sides. It covers a sensitive area of about $1\,\text{m}^2$ and has 66 million pixels.

2.2.1.2 *Strip Detector*

The silicon strip detector covers the radial range from 20 cm to 116 cm and each element can reconstruct a hit in two dimensions (η or ϕ and the position r of the strip sensor). Because the flux decreases rapidly with the distance from the interaction point ($60\,\text{kHz/mm}^2$ at 22 cm to $3\,\text{kHz/mm}^2$ at 115 cm for the design luminosity), the occupancy is small enough to get a precise measurement with a strip detector. By combining two modules which are tilted against each other they can also reconstruct hits in three dimensions.

The whole strip detector consists of 10 barrel layers and 12 endcap disks with a sensitive are of about 198 m^2 and 9.3 million strips.

2.2.2 *Muon System*

The muon system is a combination of three types of gaseous detectors to reconstruct muons which are the only Standard Model particles that can reach this part of the detector. Other particles (punch-through) traversing the magnet are stopped by the iron yoke between the different detection layers. The layout of the CMS muon system with its three sub-components, Drift Tubes (DTs), Cathode Strip Chambers (CSCs) and Resistive Plate Chambers (RPCs) is shown in Fig. 2.4. Three different detector types are used for different tasks of the reconstruction. The RPCs are used to give a fast trigger signal and to cover the large area needed and get precise measurements of the muon hits, DTs and CSCs are used. DTs are used in the barrel region, where the particle flux is low, while the CSCs are used in the endcaps where the particle flux is higher. The different detector components are briefly explained in the following sections. How the information from the different sub-systems are used to reconstruct the muon track is explained in Sec. 4.1. The muon p_T resolution of the muon system for a muon with $p_T = 100\,\text{GeV}$ is about 10 % (at $\eta \sim 0$) to 30 % (at $\eta \sim 2$).

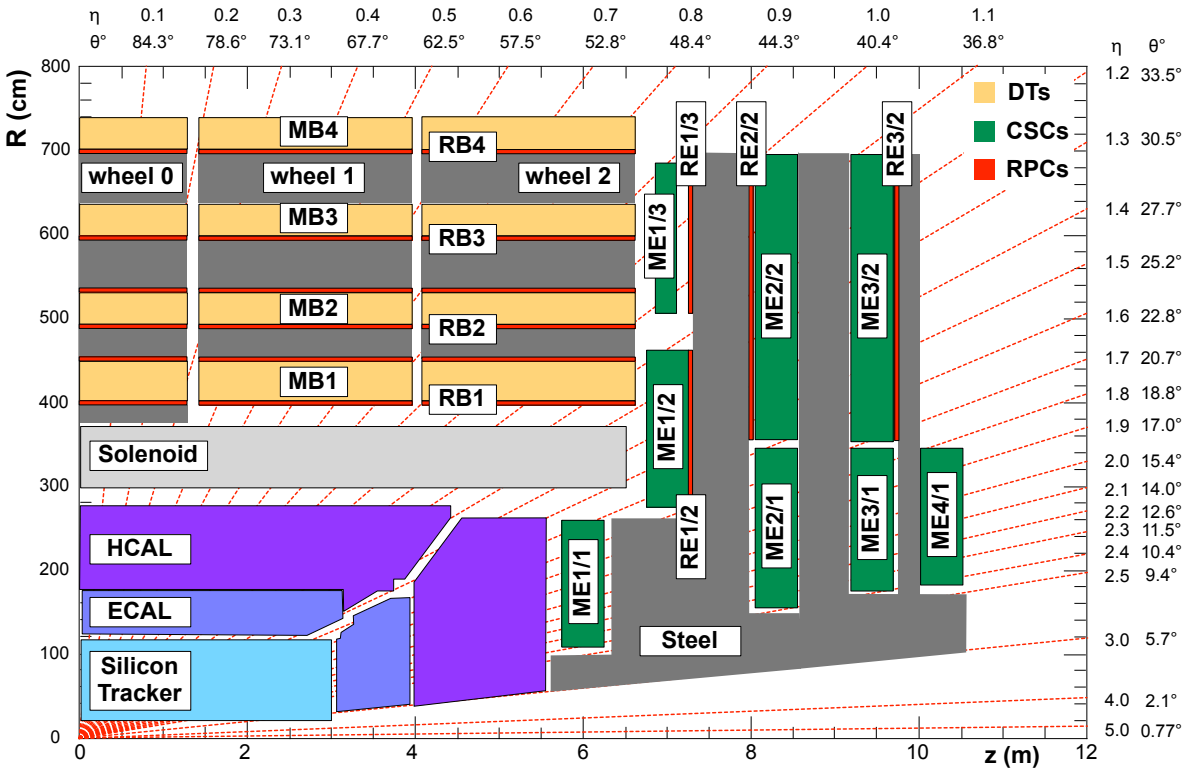

Figure 2.4: Overview of the muon system in the r-z-plane [11].

2.2.2.1 *Drift Tubes*

Drift Tubes (DTs) are detectors which are installed in the barrel region where the particle flux is low and a large area has to be covered.

One drift cell with the electric field configuration is shown in Fig. 2.5-right. The volume is filled with an $Ar - CO_2$ gas mixture, where passing muons produce electrons and ions which are separated in the electric field and collected at the central wire giving a signal. The voltage applied to the wire is $+3600\,V$, $+1800\,V$ to the strips and $-1200\,V$ to the cathodes.

This drift cells are combined to a drift tube chamber, shown in Fig. 2.5-left. The DT consists out of 3 (or 2) superlayers (SLs), each made of 4 layers of drift cells to measure the ϕ position and the z position of the hit. In the barrel, each muon has to cross four muon DTs before leaving the detector.

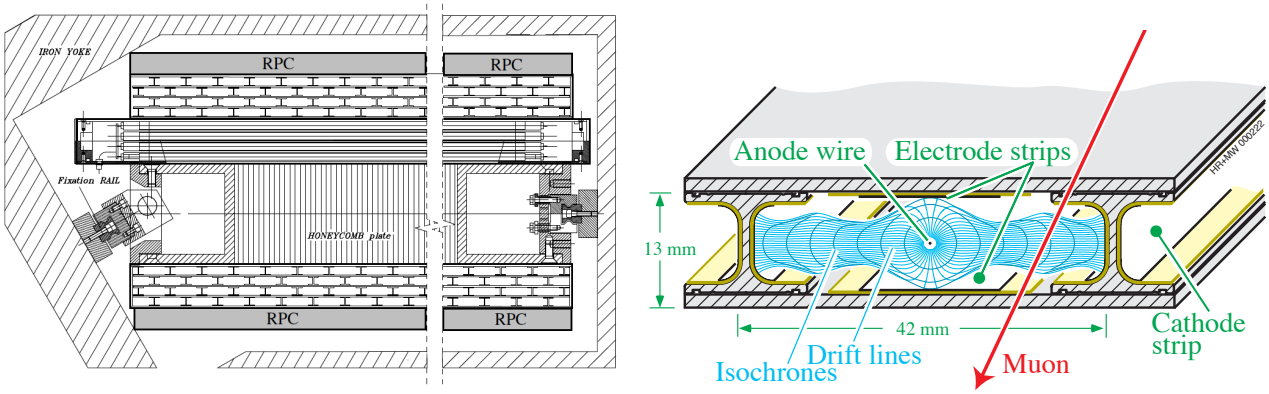

Figure 2.5: Drift Tubes: The left picture shows the layout of a DT chamber in the iron yoke in the $r - \phi$ plane consisting out of three SLs. To support the whole structure in between the SLs, a honeycomb plate is attached to the yoke. The right picture shows the layout of one drift cell: the electrodes, the isochrones and the drift lines [10].

2.2.2.2 *Cathode Strip Cambers*

The Cathode Strip Chambers (CSCs) are multiwire proportional chambers and are used as tracking detectors in the endcaps.

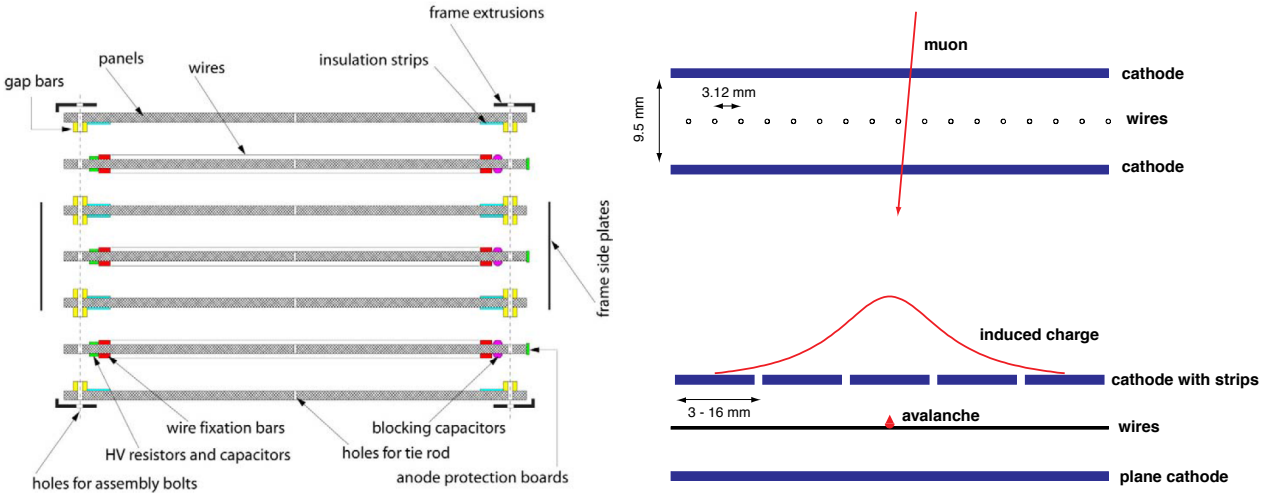

Figure 2.6: Cathode Strip Chamber: In the left picture the mechanical design of a CSC, with the 6 wire planes and 7 cathode panels is shown in an exploded view. The right picture shows the basic detection principle of the CSCs. A electron avalanche induces charge in the cathode strips and therefore allows to locate the avalanche along the wire direction [10].

The basic principle of a CSC is illustrated in Fig. 2.6-right. A muon crosses the gas volume and produces electrons and ions. The electrons are detected by the wires. The avalanche of electrons induces a charge in the cathode strips which can also be detected. By combining the two pieces of information, a two dimensional ($\phi - \eta$) hit can be reconstructed.

The chambers are made of 6 anode wire planes and 7 cathode panels shown in Fig. 2.6-left. Muons in the endcap region have to cross 4 (or 3, depending on η) CSCs before they leave the detector.

2.2.2.3 *Resistive Plate Chambers*

Resistive Plate Chambers (RPCs) are used in the barrel and endcaps. The main task of the RPCs is to provide a fast trigger signal (~few ns). The RPC modules are made of 2 gaps, operated in avalanche mode and common read-out strips in the middle, shown in Fig. 2.7. In the RPC, crossing muons produce electrons and ions. The ions drift in the electric field between the two resistive plates (bakelite) and induce a charge in the readout strip.

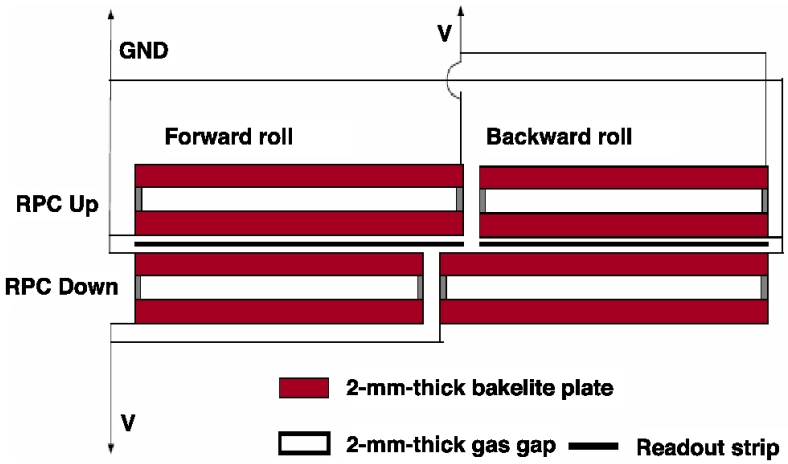

Figure 2.7: Resistive Plate Chamber: The principle design of the RPCs is shown, two bakelite plates with an electric field between them (voltage between V and ground GND). Two RPCs are combined to a module with a single readout strip in the middle [11].

2.2.3 *Calorimeters*

The other sensitive parts of the detector are the calorimeters, which are important for the measurement of the missing transverse energy and are briefly outlined in the next sections. In order to have little material in front of the calorimeters, they are placed inside the solenoid, surrounding the silicon tracker.

2.2.3.1 *ECAL*

The electromagnetic calorimeter is made of about 69 000 lead tungstate $PbWO_4$ crystals which are absorber and detection material for electromagnetic showers. The energy of the primary particle is measured via the scintillation light of the shower particles which is detected by Avalanche photodiodes (APDs) in the barrel and by vacuum phototriodes (VPTs) in

the endcaps. The thickness of the calorimeter corresponds to about $26\,X_0$ radiation lengths, to fully contain the electromagnetic shower. The energy resolution of the ECAL is given by

$$\left(\frac{\sigma_E}{E}\right)^2 = \left(\frac{2.8\,\%}{\sqrt{E}}\right)^2 + \left(\frac{0.12}{E}\right)^2 + (0.3\,\%)^2 \tag{2.1}$$

2.2.3.2 *HCAL*

The hadronic calorimeter consists of the barrel and endcap parts, and also a detection layer outside of the solenoid (Hadron Outer, HO), and two parts cover the high η region (Hadron Forward, HF). The HCAL is a sampling calorimeter with brass absorber plates and scintillator plates as detection element. The scintillation light is detected with hybrid photodiodes (HPDs). The thickness of the calorimeter is about $6\,\lambda_I$ radiation length at $\eta = 0$ and increases with η.

2.2.4 *Data Acquisition, Trigger and Computing*

The signals detected by the different systems mentioned in the previous section need to be filtered, processed and distributed to users. This is done by the Trigger, the Data Acquisition (DAQ) and the computing grid.

At the LHC collisions occur every 50 ns (a rate of 20 MHz), not enough time to read the information from the whole detector, process and store them (a rate of $\sim 10^2$ Hz). Not every collision contains interesting physics events, the events are therefore filtered by the Trigger to only select interesting events for processing. This trigger decision has to be fast, between two collisions, and uses therefore only partial information from the muon system and the calorimeters in the first step. Details on triggering and especially the muon trigger used in this analysis are described in Sec. 4.1.1.

In the first trigger stage, the event rate is reduced to $\sim$ 100 kHz which is then further processed in the High Level Trigger (HLT) that runs on a computer farm. The detector data have to be collected and sent to this computer farm at a $\sim$ 100 kHz rate by the DAQ system for the HLT processing ($\sim$ 100 GByte/s). If the HLT decision is positive, the event is recorded (at a rate of $\lesssim$ 100 Hz for each HLT trigger). All the necessary data transfer and communication and synchronization between the different systems is provided by the DAQ system.

The full reconstruction of the whole event and all following steps are done by the Worldwide LHC computing Grid (WLCG) [12]. This grid-based network of computing centers all over the world provides the computing power to reconstruct recorded events and for the simulation of Monte Carlo[1] events. It also provides the storage capacity for data and Monte Carlo events to be accessible from all over the world. The first steps of the analysis done in are also performed on the WLCG, to filter all data and all necessary Monte-Carlo samples and to reduces the file size, by only keeping the information necessary for the analysis. The analysis of this necessary information can be done on local computing resources on a reasonable time scale ($\mathcal{O}$ (hours)).

1 To compare the measurement to the expectation of the theory, events are simulated using Monte Carlo techniques. These events are mostly called Monte Carlo or MC events.

3

THEORY

In this section, the theoretical aspects of this analysis are briefly summarized. The first part (Sec. 3.1) summarizes the Standard Model of particle physics which is the basis for the background description of this analysis. The focus of this section lies on the charged weak interactions (Sec. 3.1.2.1) as this is the most important background process. Parton density functions (PDFs) are important in the environment of a hadron collider and are in the framework of this analysis a theoretical input and are therefore introduced in Sec. 3.1.3. The last part on the Standard Model is about the remaining open questions in the Standard Model (Sec. 3.1.4) which leads to the theories beyond the Standard Model (BSM). The theories which are studied in this analysis are presented in Sec. 3.2: new heavy charged vector bosons (W', Sec. 3.2.1) and effective dark matter theory (DM, Sec. 3.2.2). This summary is based on Ref. [13, 14, 15].

3.1 STANDARD MODEL

The two basic concepts of modern particle physics are special relativity and quantum mechanics. These two concepts can be combined in a quantum field theory (QFT) like the Standard Model (SM) of particle physics. In its mature form, the idea of quantum field theory is that quantum fields are the basic ingredients of the universe, and particles are just bundles of energy and momentum of the fields. Quantum field theory leads therefore to a more unified view of nature than the old dualistic interpretation in terms of both fields and particles [16]. The Standard Model describes the known elementary matter particles as shown in blue and green in Fig. 3.1 and there interactions. The matter particles are all fermions which means they have spin $\frac{1}{2}$.

The known fundamental forces or interactions of nature are gravity, electro-magnetism, the weak and the strong force. Gravity is too weak to play a role in today's particle physics, but the other three are included in the Standard Model and are mediated by the particles shown in red in Fig. 3.1. The force mediating particles are all bosons and have spin 1.

The strong force is described by the quantum chromo dynamics (QCD) and is mediated by gluons. The QCD describes the interaction of particles carrying color charge, the charge of the strong interaction, which are quarks (color or anti-color) and gluons (color and anti-color).

The weak force mediated by the W and Z bosons and electromagnetism mediated by the photon are described by the electroweak theory, sometimes called quantum flavor dynamics (QFD) [17, 18, 19, 20]. Electromagnetism couples to all particles carrying electric charge, quarks, W bosons and the charged leptons while the weak interaction couples to all particles of the Standard Model except the photon and gluon.

The particles of the Standard Model except the gluon and photon which are massless acquire there mass due to the Brout-Englert-Higgs mechanism which results in the additional

Higgs boson, shown in yellow in Fig. 3.1. The Higgs boson is the only particle in the Standard Model with spin 0 [21, 22, 23, 24, 25, 26][1].

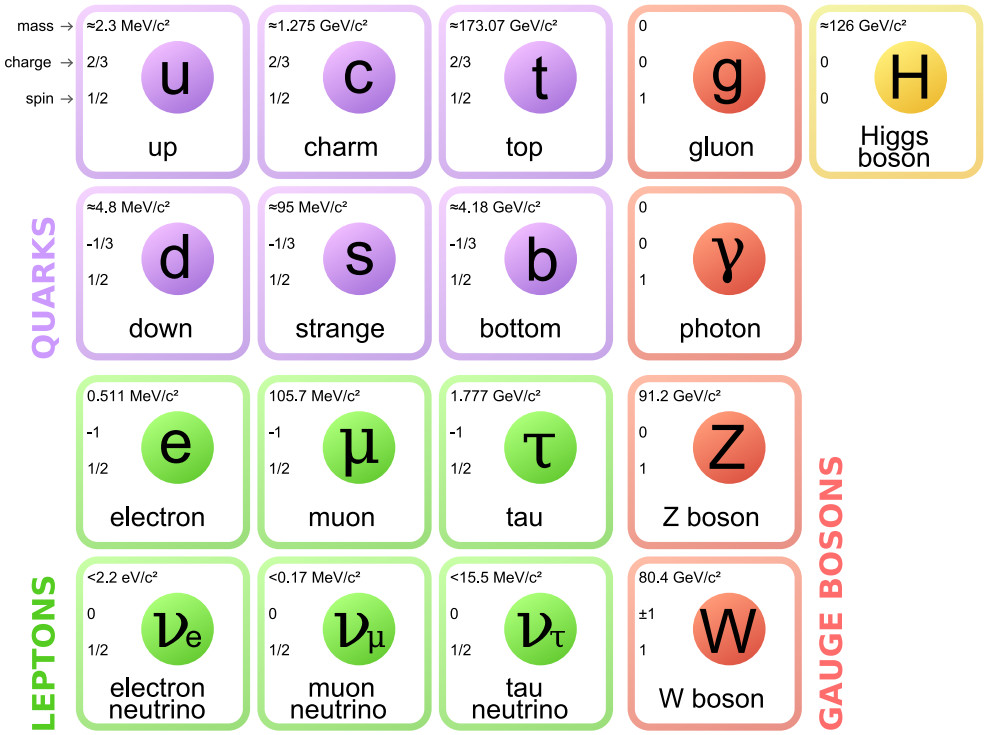

Figure 3.1: Particle content of the Standard Model: Shown are all matter particles of the Standard Model (quarks in blue and leptons in green), the force carrying particles in red and the Higgs boson in yellow. As additional information the mass, electric charge and spin are shown for every particle [29].

The fields that make up the SM are:

- The electroweak boson field represented by the vectors W_1,W_2,W_3 and B (vector in the sense that they transform like a four-vector under Lorentz transformation).
- The gluon fields represented by the vectors G_a with the index a for the eight gluon color combinations.
- The fermion field represented by the spinor Ψ (spinors transform under Lorentz transformation, but rotations turn it only by half the angle a vector would).
- The Higgs field represented by the scalar φ.

The dynamics of the quantum state and the fields are determined by the Lagrangian density $\mathcal{L}$ (or Lagrangian). In combination with the Euler-Lagrange equation

$$\frac{\partial}{\partial x_\mu}\left(\frac{\partial \mathcal{L}}{\partial\left(\partial\phi/\partial x_\mu\right)}\right) - \frac{\partial \mathcal{L}}{\partial \phi} = 0 \tag{3.1}$$

1 The Higgs particle was the last particle of the Standard Model to be discovered in 2012 [27], and parallel to this analysis the properties of the Higgs particle were measured [28].

it can be used to derive the equations of motion. Another possibility is to extract the so called Feynman rules or Feynman diagrams from the Lagrangian and use them to calculate properties of physical processes.

The Standard Model has many important properties, which are listed in the following.

- The Standard Model is a perturbative theory in the high energy regime so that solutions which are difficult to calculate exactly can be expressed by a power series and as long as the expansion parameter α is small enough can give very precise results. In the Standard Model, Feynman diagrams are used as special calculation techniques to systematically sum the power series terms.
- The Standard Model is a gauge theory, which means there are degrees of freedom in the mathematical formalism which do not correspond to changes in the physical state. The gauge group of the standard model is $U(1) \times SU(2) \times SU(3)$, where $U(1)$ acts on B and φ, $SU(2)$ acts on W and φ, and $SU(3)$ acts on G.
- The Standard Model is renormalizable, meaning that all divergent integrals in the perturbation series can be compensated by divergent not measurable bare quantities in the theory which result in finite physical quantities which are not constant but vary with the energy scale of the process (running constants).
- The Standard Model gives many precise predictions, a global fit of the theoretical predictions to precision measurement give a p-value of 0.07 where the comparison between fit and measurement is shown in Fig. 3.2a [30].

Important for this analysis is the electroweak part of the Standard Model as this describes the main background contribution, the other important part is QCD which is always important at hadron colliders, where the initial state consists out of quarks and gluons. This is illustrated in Fig. 3.2b where the cross sections for different Standard Model processes are shown, spanning 10 orders of magnitude from QCD processes (σ_{jet}), weak boson production (σ_W,σ_Z) to Higgs production (σ_{Higgs}). Due to their importance, the QCD and electroweak theory are explained in more detail in the following, with special focus on the different phenomena which arise from the theory.

3.1.1 *Quantum Chromo Dynamics*

QCD is described by the Lagrangian

$$\mathcal{L}_{SU(3)} = -\frac{1}{4} F^i_{\mu\nu} F^{i\mu\nu} + \sum_r \bar{q}_{r\alpha} i \not{D}^{\alpha}_{\beta} q^{\beta}_r \tag{3.2}$$

Where $F^i_{\mu\nu}$ is the field strength tensor of the gluon fields

$$F^i_{\mu\nu} = \partial_\mu G^i_\nu - \partial_\nu G^i_\mu - g_s f_{ijk} G^j_\mu G^k_\nu \tag{3.3}$$

g_s is the QCD gauge coupling constant and $f_{ijk}\,(i,j,k = 1,\cdots,8)$ are the structure constants of $SU(3)$. The first term of $\mathcal{L}_{SU(3)}$ describes therefore the kinetic energies and self-interactions of the gluon. The second term of $\mathcal{L}_{SU(3)}$ is the gauge covariant derivative for the quarks q_r (quark flavor r and color indices $\alpha, \beta = 1,2,3$)

$$D^{\alpha}_{\mu\beta} = (D_\mu)_{\alpha\beta} = \partial_\mu \delta_{\alpha\beta} + i g_s G^i_\mu L^i_{\alpha\beta} \tag{3.4}$$

with L^i being the Gell-Mann-Matrices times 1/2 and describes the kinetic energy of the quarks and their interaction with the gluons. The whole QCD theory leads to two phenomena especially due to the fact that gluons carry color and can therefore interact with each other and with quarks.

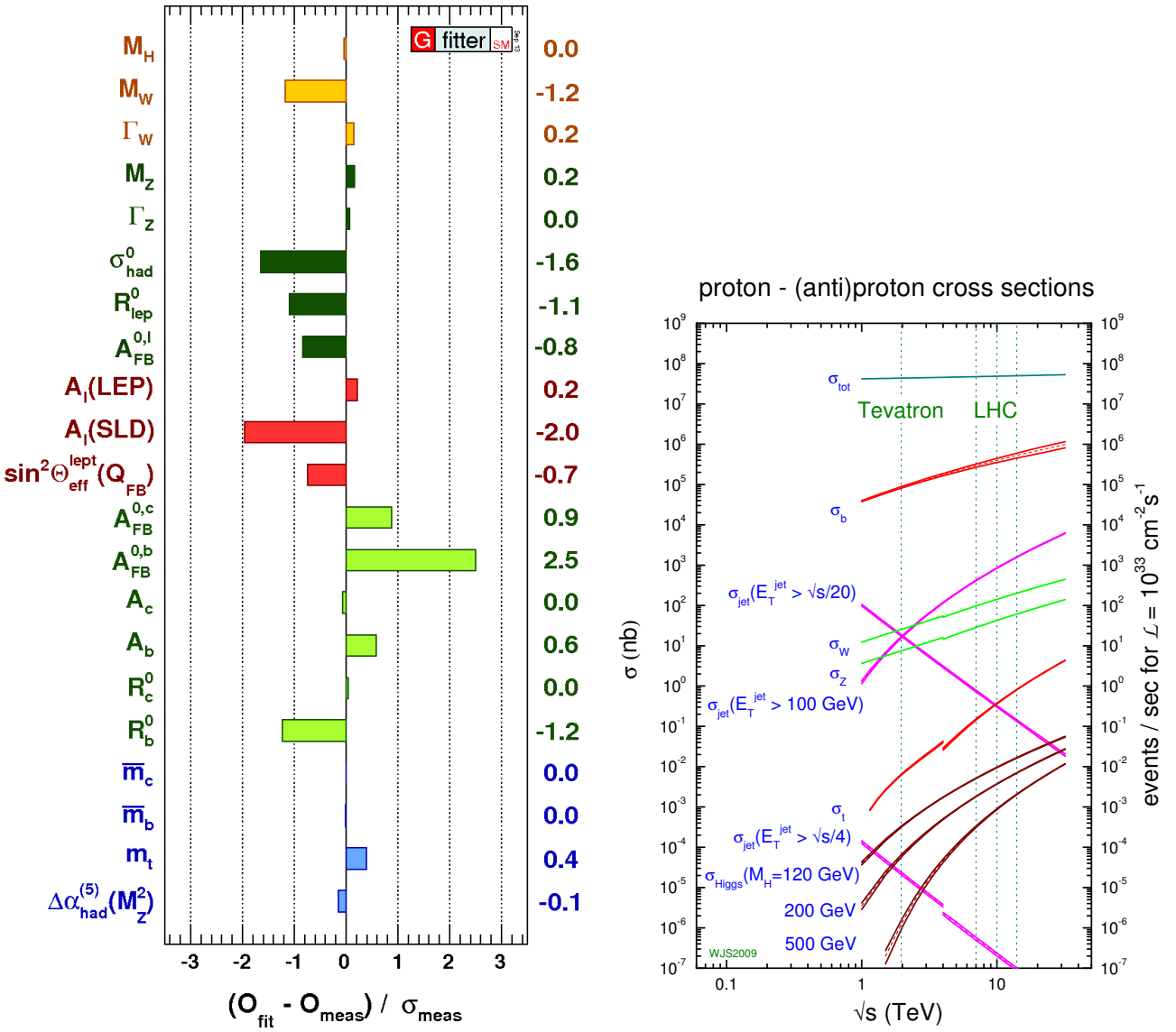

(a) Pull comparison of the fit results with the direct measurements in units of the experimental uncertainty [30].

(b) Cross sections for different Standard Model processes at different center of mass energies $\sqrt{s}$ for $p\bar{p}$ collisions (Tevatron) and pp collisions (LHC) [31].

Figure 3.2: Predictions by the Standard Model: The left plot shows a comparison of theory and measurement for different parameters. In the right plot cross sections for different processes are shown.

- Asymptotic freedom: It means quarks and gluons interact weakly at high energy transfer, and QCD processes can be calculated perturbatively in this high energy regime.
- Confinement: It means that the force between two quarks or gluons does not decrease if you try to separate them (the coupling gets stronger for lower energies / bigger distances). This results in the effect that quarks and gluons can not be observed as

free particles, but if they are produced at high energies they form hadrons if they are separated. This hadrons result in a collimated bunch of particles, called jet, which can be measured in the detector.

3.1.2 *Electroweak Theory*

The Electroweak theory is described by the Lagrangian

$$\mathcal{L}_{SU(2)\times U(1)} = \mathcal{L}_{gauge} + \mathcal{L}_{\varphi} + \mathcal{L}_{f} + \mathcal{L}_{Yukawa} \tag{3.5}$$

Where the gauge part, which describes the kinetic energy and self-interaction of $W^{\pm}$,Z and γ, is

$$\mathcal{L}_{gauge} = -\frac{1}{4}F^{i}_{\mu\nu}F^{\mu\nu i} - \frac{1}{4}B_{\mu\nu}B^{\mu\nu} \tag{3.6}$$

with the field strength tensors $F_{\mu\nu}$ and $B_{\mu\nu}$ which consist of the $SU(2)$ gauge fields W^{i}_{μ} $(i = 1, 2, 3)$ and the $U(1)$ gauge field B_{μ}

$$B_{\mu\nu} = \partial_{\mu}B_{\nu} - \partial_{\nu}B_{\mu} \tag{3.7}$$

$$F_{\mu\nu} = \partial_{\mu}W^{i}_{\nu} - \partial_{\nu}W^{i}_{\mu} - g\epsilon_{ijk}W^{j}_{\mu}W^{k}_{\nu} \tag{3.8}$$

with the gauge couplings g and g' for $SU(2)$ and $U(1)$. B and W_3 will mix to photon and Z boson with the weak mixing angle θ_W (Weinberg angle), while the $W^{\pm}$ bosons are linear combinations of the fields W_1 and W_2.

The scalar part of the Lagrangian describes the $W^{\pm}$, Z, γ and Higgs masses and couplings and is

$$\mathcal{L}_{\varphi} = \left| \left(i\partial_{\mu} - g\frac{1}{2}\tau^{i}W^{i}_{\mu} - g'\frac{Y}{2}B_{\mu} \right) \varphi \right|^{2} - V(\varphi) \tag{3.9}$$

with τ^{i} being the Pauli matrices. $\varphi = \begin{pmatrix} \varphi^{+} \\ \varphi^{0} \end{pmatrix}$ is a complex Higgs scalar and $V(\varphi)$ is the Higgs potential of the Form

$$V(\varphi) = +\mu^{2}\varphi^{\dagger}\varphi + \lambda\left(\varphi^{\dagger}\varphi\right)^{2} \tag{3.10}$$

For $\mu^{2} < 0$ there will be spontaneous symmetry breaking because the vacuum expectation value of this potential is non zero which results in $\varphi_{min} \to \frac{1}{\sqrt{2}}\begin{pmatrix} 0 \\ v \end{pmatrix}$ with the vacuum expectation value v with the minimum of the potential $V(v)$. This breaks the $SU(2)$ symmetry but not the $U(1)$ one, which leaves the photon massless. The $W^{\pm}$ and Z boson on the other hand acquire masses of $M_W = \frac{gv}{2}$ and $M_Z = \sqrt{g^2 + g'^2}\frac{v}{2}$. The requirement of $\lambda > 0$ is necessary for the vacuum to be stable. A summary of the whole mechanism and derivation of the masses is given in Ref. [32].

The fermion term which describes the kinetic energies of lepton and quarks and their interaction with $W^{\pm}$, Z and γ is

$$\mathcal{L}_{f} = \bar{L}\gamma^{\mu}\left(i\partial_{\mu} - g\frac{1}{2}\tau^{i}W^{i}_{\mu} - g'\frac{Y}{2}B_{\mu} \right) L + \bar{R}\gamma^{\mu}\left(i\partial_{\mu} - g'\frac{Y}{2}B_{\mu} \right) R \tag{3.11}$$

The last term describes the lepton and quark masses and their coupling to the Higgs and is

$$\mathcal{L}_{Yukawa} = -\left(G_1 \bar{L} \varphi R + G_2 \bar{L} \varphi_C + h.c.\right) \tag{3.12}$$

with $G_{1,2}$ being the couplings of the fermions to the Higgs which are proportional to their mass.

3.1.2.1 *Details on charged current processes*

The charged current process of the weak interaction is the most important Standard Model process for this analysis, therefore here are some more details summarized. In the charged current weak interaction, a W boson couples to either a charged lepton and a neutrino $\left(W^{\pm} \to \ell^{\pm} \nu_\ell\right)$ or two different types of quarks $\left(W^{\pm} \to q\bar{q}'\right)$.

The propagator describing the exchange of a W boson is

$$\frac{-i\left(g_{\mu\nu} - q_\mu q_\nu / \left(M_W^2 - iM_W\Gamma_W\right)\right)}{q^2 - M_W^2 + iM_W\Gamma_W} \tag{3.13}$$

with the W mass $M_W = 80.385 \pm 0.015\,GeV$ [33], the width $\Gamma_W = 2.09 \pm 1.14\,GeV$ of the W, the momentum q and the flat minkowski metric $g_{\mu\nu}$.

The W vertex factor describes a V-A-coupling (vector - axial-vector coupling) which results in the maximal parity violation of the weak interaction (the W couples only to left-handed particles or right-handed antiparticles)

$$\frac{-ig}{2\sqrt{2}} \gamma^\mu \left(1 - \gamma^5\right) \tag{3.14}$$

with the Dirac matrices γ^μ and γ^5 and the weak coupling strength $g = 0.653$ or $\alpha_W = \frac{g'^2}{4\pi} = \frac{1}{29.5}$ which is 5 times larger than the fine structure constant α. The weakness of the weak interaction comes from the propagator which is suppressed by the mass of the W boson squared and not from a small coupling constant. If the W couples to two quarks it is suppressed by the corresponding element of the CKM matrix V_{ij} for the quarks i and j.

The main background process for this analysis at leading order is a combination of W production via quarks and the decay into μ and ν_μ

$$ud \to W^{\pm} \to \mu^{\pm} \nu_\mu \tag{3.15}$$

At hadron colliders like the LHC, all undetectable particles like the neutrino can be reconstructed indirectly and only as a vector sum in the plane perpendicular to the beam direction, as the boost of the quarks along beam direction is not known (Sec. 3.1.3). Therefore, the W can not be reconstructed fully in a leptonic decay. The reconstruction of the mass in the $r - \phi$-plane results in a so called jacobian peak which has its maximum at the W mass (half the W mass in the p_T or $\not{E}_T$ spectrum). The shape of this peak is shown in Fig. 3.3. In this analysis the transverse mass

$$M_T = \sqrt{2 \cdot p_T \cdot \not{E}_T \cdot \left(1 - \cos\left(\Delta\phi(\mu, \not{E}_T)\right)\right)} \tag{3.16}$$

is used as the final discriminating variable.

3.1.3 *PDFs*

The initial state particles for all physics processes at the LHC are quarks and gluons, but they are confined to the protons which collide in the LHC. The proton consists out of two up and one down quark (called valence quarks), but all quark and anti-quark flavors (called sea quarks) and gluons can be found inside the proton with a certain probability. Parton distribution functions (PDFs) are used to describe these probabilities (details can be found in Ref. [34]). The parton density function $f_i\left(x, Q^2\right)$ gives the probability of finding a parton with flavor i inside the proton carrying a fraction x of the proton momentum with Q being the energy scale of the hard interaction. Since the theory does not predict the x dependence of the PDFs, they are determined by fits to measurements of different processes, using the DGLAP evolution equation which relates the PDF for different Q scales [35]. This is either done by making assumptions on the analytical form of the PDF or by using neural-net technology. Because there are many different ways to choose the input data, the assumptions which are made, the treatment of heavy quarks and the treatment of uncertainties, there are different PDF sets available. The most commonly used are MSTW (Martin-Stirling-Thorne-Watt) PDFs [36, 37], the CTEQ (Coordinated Theoretical-Experimental Project on QCD) PDF [38, 39] and the NNPDF (Neural Net PDF) [40]. Different versions of the CTEQ PDFs are used for the simulation of the physics processes used in this analyses, and all three PDF sets are used to determine the systematic uncertainty coming from the PDF sets (see section 6.5). In Fig. 3.4 the PDFs are shown for different parton flavors, and the x and Q dependence for the up quark is displayed for the MSTW PDF as an example. All PDF related parts in this analysis were done with the LHAPDF [41] package.

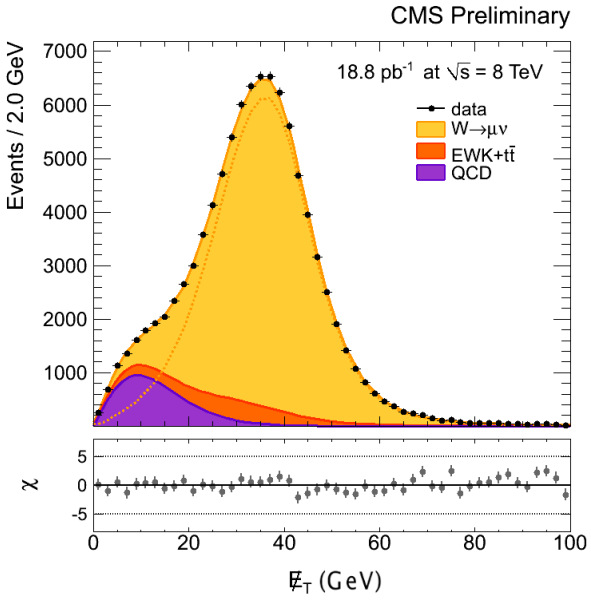

Figure 3.3: Jacobian peak: The measurement of the W jacobian peak in the muon channel is shown in the $\not{E}_T$-spectrum. The ratio χ is defined via the number of observed events N_{obs} and the number of expected events N_{exp} as $\chi = (N_{obs} - N_{exp})/\sqrt{N_{obs}}$ [42]. In this plot the background prediction is shown as a stacked histogram and the observed data is shown with black markers. This style is used throughout this analysis for many histograms.

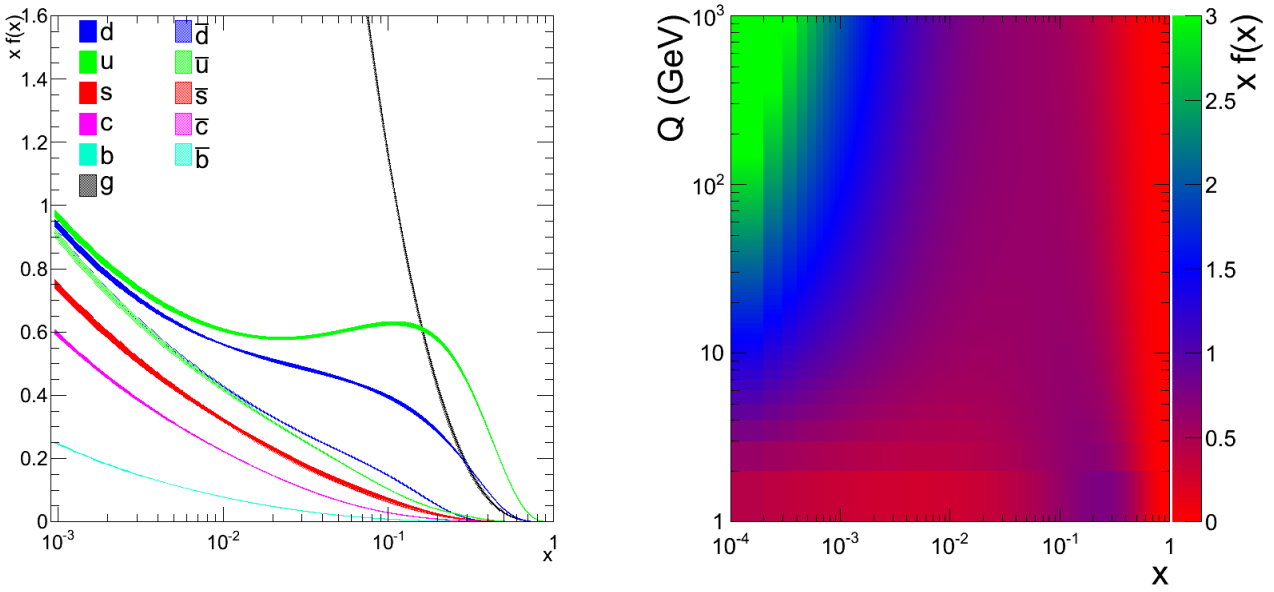

(a) Parton distribution function $x\,f(x)$ for $Q = 10\,GeV$ for the different parton flavors.

(b) Parton distribution function $x\,f(x)$ against x and Q for the up-quark.

Figure 3.4: Example distributions for MSTW PDFs, made with LHAPDF.

3.1.4 *Open questions of SM*

The Standard Model is well confirmed by experimental data (as indicated in section 3.1) but it leaves some open questions and unexplained phenomena. Some examples are listed in the following.

- The Standard Model contains at least 19 parameters which are a lot of parameters that can only be determined by experiment. This leaves the question if the number of parameters can be reduced by determining the parameter value from theory.
- Gravity is not included in the Standard Model. When the strength of gravity coupling becomes comparable to the other forces, new physics is expected to occur. Often a unification of the forces is suggested. The natural energy scale for this unification is the Planck scale $\Lambda_{Planck} \sim 10^{19}\,GeV$.
- Hierarchy/fine-tuning problem: The quantum corrections to the Higgs mass from the fermions can be calculated to be

$$\Delta m_H^2 = -\frac{|\lambda_f|^2}{8\pi^2}\left[\Lambda_{UV}^2 + \cdots\right] \tag{3.17}$$

  with the couplings to fermions λ_f and the scale of new physics Λ_{UV}. If the scale of new physics is the Planck scale, then Λ_{UV} is about $10^{19}\,GeV$ and the corrections to the Higgs mass are huge. The bare Higgs mass must be precisely tuned to this correction, to get the observed mass of $126\,GeV$.
- Vacuum stability: Extrapolating the Standard Model with the measurement of the Higgs mass to very high energies indicate that $\lambda \approx 0$. This results in a meta-stability of

the electroweak vacuum and a lifetime longer than the age of the universe [43]. This indicates physics beyond the Standard Model at least at a scale of $\Lambda \sim 10^{12}$ GeV (see Fig. 3.5).

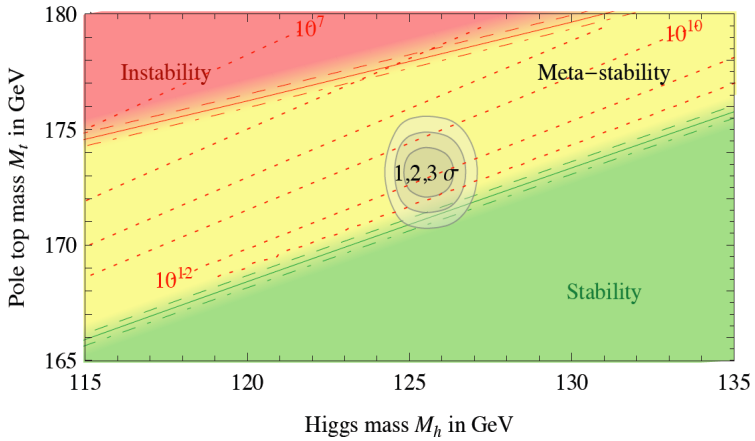

Figure 3.5: Phase diagram of the Higgs potential: The observed point of the Standard Model and its uncertainties $(1, 2, 3\,\sigma)$ are shown in gray. The red dotted lines show the instability scale Λ in GeV [44].

- Other open questions or unexplained phenomena come from precise cosmological observations in the universe and can be explained by new theories of particles physics or extensions to the Standard Model:
  - It is observed that the universe is flat, homogeneous and isotropic. To account for this and other observations the concept of inflation was introduced, which describes an epoch in the early universe with rapid exponential expansion of the universe. This concept is not explained by the Standard Model but could be physics beyond the Standard Model [45].
  - Baryonic asymmetry of the universe: The observed universe consists mostly of matter but in the early universe the same amount of matter and antimatter should be produced. The necessary symmetry violation between matter and antimatter in the Standard Model is commonly believed to be too small to account for the observation of this asymmetry and needs therefore physics beyond the Standard Model [46].
  - The Standard Model describes only $4.82 \pm 0.11\,\%$[2] of the energy density of the universe [47].
  - Dark Energy, a hypothetical form of energy that accelerates the expansion of the universe, is the most accepted hypothesis to explain the cosmological observations and makes up $69.2 \pm 0.1\,\%$[2] of the energy density of the universe [48].
  - Dark Matter is a form of matter that explains different cosmological and astrophysical observations (some of them are listed below). Because a big part of this analysis is the search for Dark Matter candidates (section 3.2.2), some of the observations and hints on Dark Matter are listed below (a summary is given in Ref. [49]).

2 This values are not constant over the age of the universe, the values listed here are the ones observed today.

* The measurement of the cosmic microwave background (CMB) can be used to determine the total amount of Dark Matter to be $25.82 \pm 0.69\,\%$[2] of the energy density of the universe [47].
* Galaxy rotation curves: Observations of the velocity of matter in galaxies can not be explained by Newtonian gravity and the observed matter density (labeled disk and gas in Fig. 3.6a). If newtonian dynamics is assumed to be the correct description of the observation an additional gravitational component (labeled halo in Fig. 3.6a) has to be introduced which couples not via electromagnetism and is therefore called Dark Matter.
* The cluster $1E0657-558$ which consists of two matter concentrations (two galaxy clusters after a collision) requires Dark Matter to explain the observations. By comparing the measurements of the normal matter via X-ray radiation with the whole matter via gravitational lensing (Fig. 3.6b) one can see a clear distinction between the center of observed matter and the center of gravitational matter. This can only be explained by additional Dark Matter and not by a modified law of gravity.

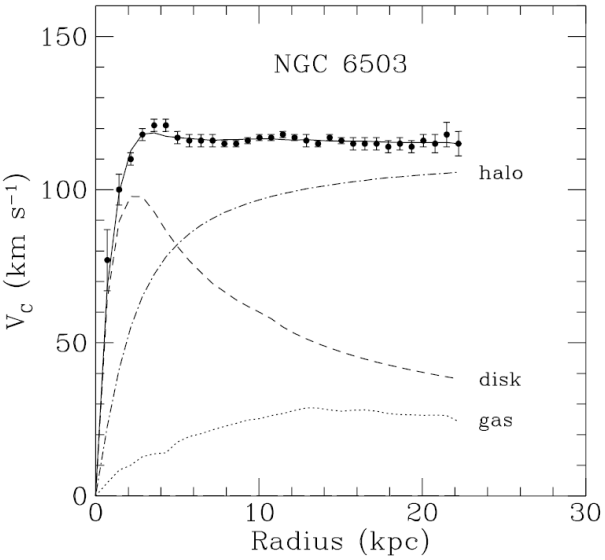

(a) Rotation curve of the galaxy NGC 6503, showing the observed rotation velocity as a function of the distance from the galactic center. The dotted lines are the contributions of gas, disk and the dark matter halo [50].

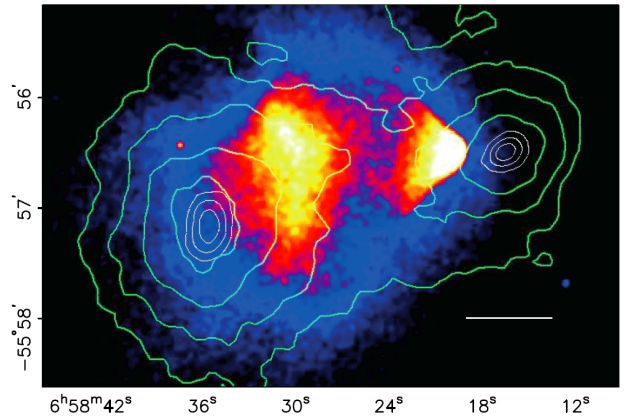

(b) X-ray image of the galaxy cluster $1E0657-558$ as a colored image. The contour lines indicate the distribution of matter observed with gravitational lensing. The white bar indicates a distance of 200 kpc [51].

Figure 3.6: Observations on Dark Matter.

* WIMPs: If we assume an additional, undiscovered, stable (or long-lived) weakly-interacting massive particle (WIMP) χ, there are some interesting consequences. In the early universe at very high temperatures ($T \gg m_\chi$), χ's are in equilibrium with the Standard Model particles converting into each other ($\chi\bar{\chi} \longleftrightarrow f\bar{f}$, where $f\bar{f}$ means all particle anti-particle combinations which are kinematically allowed $m_\chi > m_f$). If the universe expands, the temperature drops, the number density of χ's drops exponentially and at some point the χ's cease to

annihilate (freeze out). A relic cosmological abundance remains. The WIMP abundance can be approximated with

$$\Omega_\chi h^2 = \frac{m_\chi n_\chi}{\rho_C} \simeq \left(\frac{3 \times 10^{-27}\, cm^3 sec^{-1}}{\sigma_A v} \right) \tag{3.18}$$

with the number density n_χ, the critical density ρ_C, the annihilation cross section σ_A and the relative velocity v. The WIMP velocities at freeze out are some fraction of the speed of light. If the cosmical abundance is at the order of unity, from Eq. 3.18 follows the annihilation cross section is roughly $10^{-8}\, GeV^{-2}$. This is the same order of magnitude one would expect from a typical electroweak cross section

$$\sigma_{weak} \simeq \frac{\alpha^2}{m^2_{weak}} \tag{3.19}$$

with $\alpha \simeq \mathcal{O}(0.01)$ and $m_{weak} \simeq \mathcal{O}(100\, GeV)$. The value that comes from Eq. 3.18 needed to get $\Omega_\chi \sim 1$ comes essentially from the age of the universe which should not be related to electroweak physics. This suggest that a WIMP particle with electroweak interactions may exist which would be a natural Dark Matter candidate [52, 53].

3.2 BEYOND STANDARD MODEL

In this section, the theories beyond the Standard Model which are studied in this analysis are summarized. These theories were developed to answer some of the open questions of the Standard Model.

3.2.1 *Sequential standard model W′*

A number of extensions of the Standard Model predict new heavy charged vector Bosons W'. Three examples are

- The Standard Model can be extended to be left-right symmetric by an additional $SU(2)_R$. This symmetry must be broken at low energies to account for the observation that the weak force couples only to left handed particles [54].
- In the so called little Higgs models, based on the idea that the Higgs boson is a pseudo-Goldstone boson arising from global symmetry breaking at a TeV energy scale, also additional $SU(2)$ groups are introduced [55].
- Grand unified theories (GUTs) are theories which try to unify the electromagnetic, the weak and the strong interaction by including the Standard Model gauge group in a bigger group, for example $SU(5)$ or $SO(10)$ ($SO(10) \supset SU(5) \supset SU(3) \times SU(2) \times U(1)$) [56].

The reference model by Altarelli et al. [57], in which the W' is a carbon copy of the Standard Model W-boson is used to model the signal. This sequential standard model (SSM) W' does not depend on specific model assumptions by the different extensions to the Standard Model, but is just assumed to have the same fermionic couplings as the Standard Model W. This

model has been used in the corresponding searches in the leptonic channels at the Tevatron [1, 2] and at the LHC [58, 59] and is also the baseline here. Decays of the W' bosons into the SM bosons W and Z are assumed to be suppressed. This suppression is possible if W' and W belong to different gauge groups, which would result in a suppression factor of $M_W^2/M_{W'}^2$. Thus, the W′ decay modes and branching fractions are similar to those of the W-boson, with the notable exception of the $\bar{t}b$ channel which opens up for W' masses beyond 180 GeV, yielding a branching fraction of 8% for each of the three leptonic channels ($W' \to \ell\nu$, with $\ell = e, \mu, \tau$) and 25% for each of the $q\bar{q}$ channels. Combining the three lepton and quark decay channels (assuming that the W′ does not decay to anything else), and neglecting all fermion masses except for the top and bottom quark, one obtains for the width

$$\Gamma_{W'} = m_{W'} \frac{g^2}{2} \frac{1}{48} \left(18 + 3F\left(\frac{m_t}{m_{W'}}, \frac{m_b}{m_{W'}} \right) \right) \tag{3.20}$$

with

$$F(x_1, x_2) = \left(2 - x_1^2 - x_2^2 - (x_1^2 - x_2^2)^2\right) \sqrt{\left(1 - (x_1 + x_2)^2\right) \cdot \left(1 - (x_1 - x_2)^2\right)} \tag{3.21}$$

The resulting width is $\Gamma_{W'} = \mathcal{O}(10\,\mathrm{MeV})$ for W' masses of $m_{W'} = \mathcal{O}(1\,\mathrm{TeV})$. An interference between the W and the W' Feynman graphs is not considered in this model (a study considering interference can be found in Ref. [60]). A Feynman graph of the studied process is shown in Fig. 3.7 and involves production of a W' via two quarks and decay of the W' into a μ and ν_μ. This signature results in the experiment as a high p_T muon balanced back to back in the transverse plane with missing transverse energy from the neutrino.

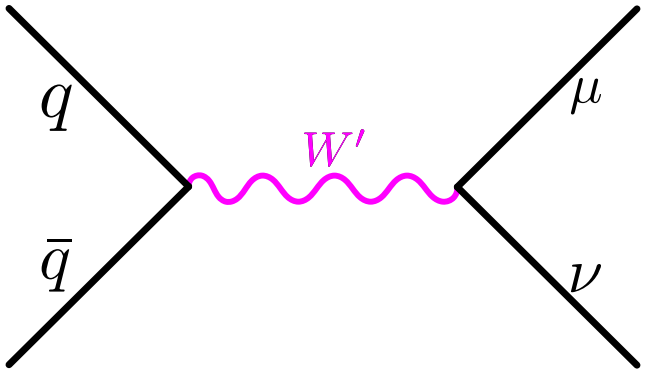

Figure 3.7: Feynman graph for the production of a W' boson and subsequent decay into a muon and a neutrino.

3.2.2 *Dark Matter*

As indicated in Sec. 3.1.4, a likely candidate for Dark Matter are weakly interacting massive particles (WIMPs), but this just describes the properties of the Dark Matter particle, and not an underlying theory. The particles have to be massive $\mathcal{O}(\mathrm{GeV} - \mathrm{TeV})$ and are only weakly interacting, which can, but must not, be the weak interaction of the Standard Model. Two example theories which can contain WIMPs are sketched in the following [61, 62, 63].

- SUSY WIMP: Supersymmetry is a class of proposed extensions of the Standard Model which relates fermions and bosons, by introducing for every fermion of the Standard

Model a boson as a superpartner and vice versa. Supersymmetric models have many theoretical advantages, they can solve for example the hierarchy problem (see Sec. 3.1.4). In many Supersymmetric models, the neutralino (electrically neutral fermion) is a candidate for WIMPs [53].

- KK WIMP: A Kaluza-Klein (KK) like theory is an extension to the Standard Model which tries by introducing extra dimensions to unify gravity and electromagnetism . In this theory, particles of the Standard Model are the first in a series (called KK-tower) of particles with increasing masses. One of theses KK-particles (e.g. the first excitation of the photon) would be a WIMP candidate [64].

To be as model unspecific as possible, an effective field theory (EFT) is used. In this EFT the basic process of WIMPs χ coupling via a particle ϕ to the Standard Model quarks is simplified to a four fermion interaction as illustrated in Fig. 3.8.

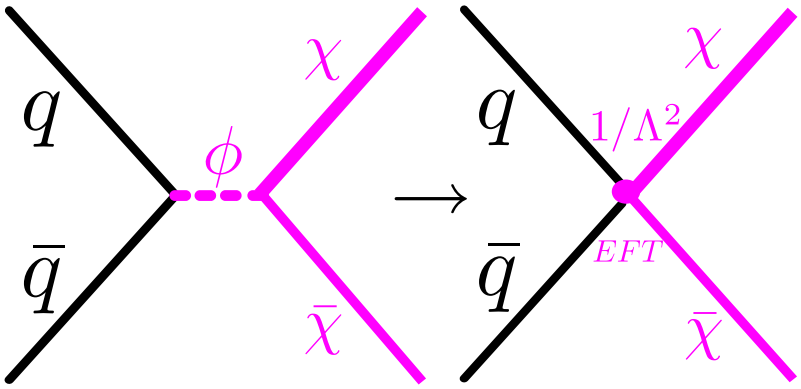

Figure 3.8: Effective field theory: The left Feynman graph shows the coupling of Dark Matter particles χ via the mediator ϕ to quarks. This coupling is simplified by an effective field theory shown in the right Feynman graph.

This simplification is based on three assumptions:

1. The WIMP particle is the lightest particle beyond the Standard Model accessible at the LHC. Any other new particle has a mass larger than the WIMP mass or a smaller coupling.
2. The WIMP interaction with Standard Model particles is dominated by only one type of coupling (see below: vector or axial-vector coupling).
3. The WIMP particles are fermions. Scalar WIMPs would also be possible but are not studied in this analysis. WIMPs with spin one or higher are in principle possible but the couplings of these WIMPs are usually restricted by gauge invariance and other symmetries [65].

In this effective field theory, the propagator of the heavy particle ϕ can be expanded in $(q/M)^2$ with the momentum q and mass M of the heavy particle. The two resulting couplings in first order of the expansion which are studied in this analysis are

$$\text{vector coupling (V):} \frac{1}{\Lambda^2}\bar{\chi}\gamma^\mu\chi \sum_i \xi_i \bar{q}_i\gamma_\mu q_i \tag{3.22}$$

$$\text{axial-vector coupling (AV):} \frac{1}{\Lambda^2}\bar{\chi}\gamma^\mu\gamma^5\chi \sum_i \xi_i \bar{q}_i\gamma_\mu\gamma^5 q_i \tag{3.23}$$

where Λ is the interaction energy scale which is related to the messenger particle ϕ via

$$\Lambda \sim \frac{M_\phi}{\sqrt{g_{SM} g_\chi}} \tag{3.24}$$

with the couplings g_{SM} and g_χ. ξ_i is the real relative coupling strength to the quark flavor i. These couplings are studied because they are similar to couplings in the Standard Model (Sec. 3.1.2.1) and can be introduced without further modification of the Standard Model. The vector coupling is spin independent, while the axial vector coupling is spin dependent via the γ^5 operator.

In order to get a stable WIMP, one usually introduces a new symmetry (e.g. R-parity of supersymmetry or KK-parity in extra dimensions). This only allows pair production of WIMPs.

At the LHC this theory results in two particles which can not be detected as they are leaving back-to-back the detector, so the pure process is not detectable. Through initial state radiation of Standard Model particles, a boosted pair of WIMPs is produced recoiling against a Standard Model particle. This signature is detectable. In the initial state radiation, a gluon can be radiated (this corresponds to the mono-jet search [66]), a photon (mono-photon [67]) or a $W^\pm/Z$ boson. If the radiated particle is a $W^\pm$ which decays into a charged lepton and a neutrino, the event signature is exactly the same as for the W' analysis, $\not{E}_T$ due to undetected particles back-to-back with a charged lepton. The studied process is shown in Fig. 3.9. The kinematic signature is the same as for W', but $\not{E}_T$ does not only correspond to the neutrino, but the neutrino plus the two undetectable WIMPs. Back-to-back are not muon and neutrino, but the W and the two WIMPs

$$p_T(W) = -(p_T(\bar{\chi}) + p_T(\chi)) \tag{3.25}$$

this results with $p_T(W) = p_T(\mu) + p_T(\nu)$ in

$$p_T(\mu) + p_T(\nu) = -(p_T(\bar{\chi}) + p_T(\chi)) \tag{3.26}$$

$$p_T(\mu) = -(p_T(\bar{\chi}) + p_T(\chi) + p_T(\nu)) = -\not{E}_T \tag{3.27}$$

which is the expected behavior, muon and $\not{E}_T$ are balanced and back-to-back, even when $\not{E}_T$ consists out of three instead of one undetectable particle.

The phenomenology is controlled by the scale Λ of the effective interaction, and the mass of the dark matter particle M_χ. In addition, a relative coupling ξ_i for each quark flavor i is possible. In searches at colliders where DM is produced in pp collisions, the difference between vector (V) and axial-vector (AV) coupling is less important as in direct DM-nucleon interaction searches. This is due to the large influence of the spin on the interaction at low Q^2 (in the order of 1 to 100 keV [33]). At the LHC half of the initial quarks originate from the quark-gluon sea and hence all spin configurations and light quark flavors are available in the production.

The nature of the DM coupling results in interference for this specific channel of an initial state $W^\pm$ radiation (see Fig. 3.10). The dominant initial state is $u\bar{d}/d\bar{u}$. The DM particles either couple to the up or the down type quark with the same initial and final state. The relative coupling strength can be parametrized by a single factor ξ between up- and down-type quarks. This simplifies Eqn. 3.22 & 3.23 to one single factor ξ (independent on i) illustrated in the Feynman graph in Fig. 3.10. The interesting values are $\xi = 0$ and $\xi = \pm 1$. If not stated

otherwise ξ is set to 1 in this analysis. A value of $\xi = 0$ results in a coupling only to one quark type while for the energies at the LHC it is irrelevant, if the factor modifies the coupling to up or down type quarks. The value $\xi = +1$ corresponds to destructive interference and $\xi = -1$ to constructive interference. The interference changes the total cross section and the steepness of the M_T spectrum.

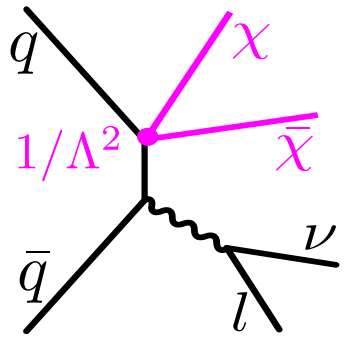

Figure 3.9: Dark Matter Feynman graph: The Feynman graph shows the studied process of this analysis, the pair production of two WIMPs recoiling against a Standard Model $W^{\pm}$ which decays into a muon and a neutrino.

To see where the interference comes from, depending on ξ, the vector-coupling can be simplified

$$\frac{1}{\Lambda^2}\bar{\chi}\gamma^{\mu}\chi\ \left(\bar{u}\gamma^{\mu}u + \xi\bar{d}\gamma_{\mu}d\right) \longrightarrow (a + \xi \cdot b) \tag{3.28}$$

with the definitions for the coupling to up and down type quarks

$$a = \frac{1}{\Lambda^2}\bar{\chi}\gamma^{\mu}\chi\ \bar{u}\gamma_{\mu}u \tag{3.29}$$

$$b = \frac{1}{\Lambda^2}\bar{\chi}\gamma^{\mu}\chi\ \bar{d}\gamma_{\mu}d \tag{3.30}$$

For the absolute square follows:

$$|(a + \xi \cdot b)|^2 = |a|^2 + |\xi \cdot b|^2 + 2 \cdot \xi \cdot |a| \cdot |b| \cdot \cos\Delta\varphi \tag{3.31}$$

with the complex phase difference $\Delta\varphi$ between the complex numbers a and b.

For the three studied values of ξ follows

- ξ = -1: $\Rightarrow |a|^2 + |b|^2 - 2 \cdot |a| \cdot |b| \cdot \cos\Delta\varphi$ (constructive interference if $|a| \cdot |b| \cdot \cos\Delta\varphi < 0$)
- $\xi = 0$: $\Rightarrow |a|^2$ (no interference)
- ξ = +1:$\Rightarrow |a|^2 + |b|^2 + 2 \cdot |a| \cdot |b| \cdot \cos\Delta\varphi$ (destructive interference if $|a| \cdot |b| \cdot \cos\Delta\varphi < 0$)

For $|a| = |b|$ and $\cos\Delta\varphi = 1$ there is a difference between no interference and constructive interference of a factor 4 and the destructive interference case goes to zero. As this equality is not exact, for the destructive interference the rate is not exactly zero and the constructive interference is not exactly four times higher. The comparison between the different values for ξ is given in Sec. 5.3.3.

In contrast to direct detection searches, the production via heavier quarks (s,c) is also considered, which are only accessible at collider DM searches. Other collider searches such as mono-jet or mono-photon are not sensitive to the quark type or the interference, because only same flavor initial states are possible.

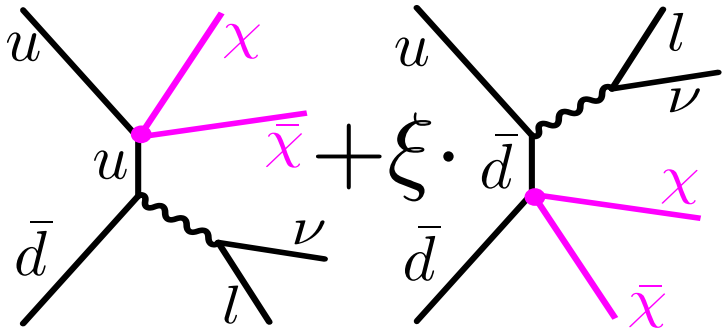

Figure 3.10: Dark Matter interference Feynman graph: This Feynman graph illustrates the interference between the process where the WIMPs couple to the up-type quarks and where they couple to the down-type quarks, resulting in two different Feynman graphs with the same initial and final state and therefore interference between them.

Additional jets can be produced via initial state radiation and the Feynman graph shown in Fig. 3.11. In this process a gluon is in the initial state. The process with one additional jet has a comparable cross section to the process without the additional jet (see Sec. 5.3.3).

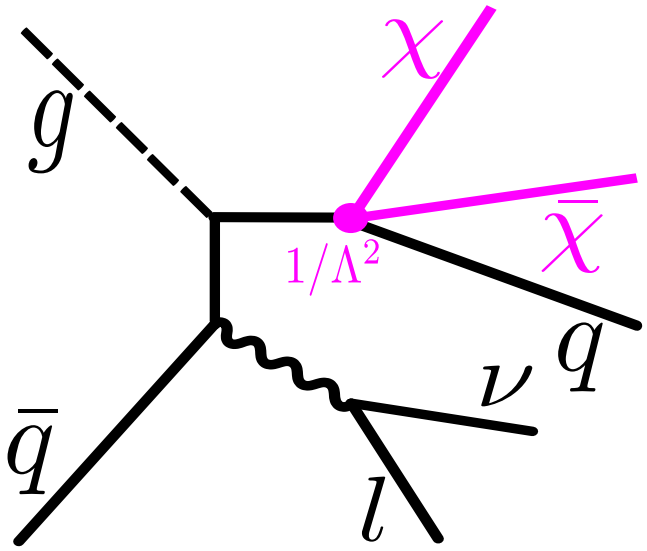

Figure 3.11: Dark Matter Feynman graph with an additional jet in the final state: The production of additional jets can happen via initial state radiation and vie the shown Feynman graph. The cross section for the process with one additional jet is comparable to the one without the jet (see Sec. 5.3.3).

4 OBJECTS

In this section, the objects which are used in this analysis, high-p_T muons (Sec. 4.1) and missing transverse energy $\not{E}_T$ (Sec. 4.2), their reconstruction and corrections are explained.

4.1 MUON

Muons are the only detectable particles which can travel through the whole detector and penetrate the iron of the magnet return-yoke. Therefore they can be identified with high efficiency and purity. Muons are very useful to trigger interesting events. Muons are minimum ionizing particles (MIPs)[1] and loose only little energy when the cross the detector. In this section, the muon trigger (Sec. 4.1.1), the muon reconstruction (Sec. 4.1.2) and the final muon selection (Sec. 4.1.3) are explained. The track reconstruction algorithm reconstructs from the different hits in the detector a trajectory and is basically the same on trigger level and fin the offline analysis, and it is explained in the following.

On HLT and muon reco level[2] the following algorithm is used to build the muon trajectory. The main difference between the different reconstructions is, which hits are taken into account for the fit [68, 69].

The algorithm works iteratively, starting with the best quality hits, reconstructs the track and removes hits associated to the track and starting all over again. For reconstructed tracks, a χ^2 can be calculated as measure for the fit quality. All track parameters have uncertainties, which are propagated to the physical parameters of the particle. Examples are momentum or direction. The resulting uncertainties are stored for every track. One can summarize the algorithm in four steps:

1. Seeding: Find a track seed to start the reconstruction. There are two possible seeds for the reconstruction, a hit-pair or hit-triplet compatible with the beam spot or a track segment with initial momentum and direction in the DTs or CSCs.

2. Trajectory building: Starting from the track seed, the trajectory is build by locating compatible hits on the next detector layer. The track finding and fitting is done by a combinatorial Kalman filter [70]. The Kalman filter starts with track parameters $\widetilde{p}_i$ and its covariance matrix $C(\widetilde{p}_i)$ and propagates them to the next detector layer. For this propagation, the magnetic field $\overrightarrow{B}$ and the effects of the detector material have to be taken into account. On this next detector layer, the trajectory state is updated with the information of a compatible hit and the propagation is continued.

3. Trajectory cleaning: Cleaning tracks to solve ambiguities which are produced by the trajectory building for tracks which share hits.

4. Trajectory smoothing: To take the information from the full covariance matrix for the final track fit into account a backward fitting is done when the informations for all hits are available at the end of the trajectory cleaning.

1 For muon momenta of $\mathcal{O}(0.1\,\text{GeV}) - \mathcal{O}(100\,\text{GeV})$.
2 Reco level means the reconstruction level.

4.1.1 *Muon Trigger*

The collision rate at the LHC is $2 \cdot 10^7$ collisions/s, which is too high to record and reconstruct every event. A preselection is necessary to select interesting events. This is done by the trigger system. The trigger is separated into two levels, the Level 1 (L1) trigger and the high-level-trigger (HLT), both are briefly explained in the following [71].

4.1.1.1 *L1 Muon Trigger*

The L1 trigger is implemented in hardware and analyses the hits from the muon systems' CSC, DT and RPC. In each subsystem a local reconstruction determines from which bunch crossing the event originates and reconstructs a track segment with the number of muon stations containing hits and a p_T-value. The global muon trigger then combines the information from the three subsystems to calculate the position, quality and p_T for the 4 muons with the best fit quality. These up to 4 different muons are combined by the global trigger with calorimeter information for triggers containing isolation. Depending on their p_T, the muons are selected if they pass the trigger or not[3].

4.1.1.2 *HLT Muon Trigger*

The HLT is implemented as software and runs on the online event filter parallel computer farm. The HLT muon reconstruction chain is started if one L1 trigger decision containing muons is positive. In principle, the muon reconstruction procedure on the HLT level is the same as for the final muon reconstruction, but optimized to save CPU time. The HLT trigger is divided into two levels, called L2 and L3.

On level 2, a muon reconstruction in the muon system is conducted with a momentum precision of about 15%. The seed for the reconstruction is taken from the L1 trigger. The L2 trigger decision is done depending on p_T and some quality criteria. On level 2 the isolation is calculated from calorimeter information.

On level 3 an additional track reconstruction is done in a slice of the tracker, determined from the extrapolated L2 muon track. With the additional information from the tracker, the momentum precision goes up to about 1% (for not too high p_T). It also allows to select the track impact parameter, and the track isolation can be calculated from nearby pixel hits.

The trigger used for the analysis is the so called `HLT_Mu40_eta2p1` which is seeded by the `L1_SingleMu16er` and requires a p_T greater than 40 GeV and a pseudorapidity $|\eta|$ smaller than 2.1. It is the single muon trigger with the lowest p_T-threshold which is not pre-scaled[4] or requires isolation.

4.1.2 *Muon Reco*

The reconstruction of muons with high momentum is difficult, because the transverse momentum is measured by the curvature of the muon track in the magnetic field, which is very small for high p_T. For a muon with a $p_T = 200\,\mathrm{GeV}$ the sagitta (the distance from the center of the arc to the center of its base) is about $0.1\,\mathrm{cm}$ in the Tracker alone and about $1\,\mathrm{cm}$ in

3 In the muon reco of course more than four muons can be reconstructed.

4 Pre-scaled triggers are only recorded for a fraction of the events where the trigger fired. This fraction is one over the so called pre-scale.

combination with the muon system. The probability to produce secondary particles and electromagnetic showers especially in the iron-yoke also increases exponential with p_T. Different algorithms take the problems which occur at high p_T into account. On the one hand there are the default reconstruction algorithms for global and tracker-muons [68], and on the other hand there are special refits to take the effects which occur at high momenta into account, TPFMS and Picky [72]. To take advantage of all algorithms, the TuneP algorithm is used in this analysis, which tries to select the best algorithm for each event. All these algorithms are shortly explained in the following:

4.1.2.1 *Tracker Muon*

To compensate for missing hits in the muon system due to low momentum or hit losses in the gaps between the muon wheels, the tracker muon algorithm was developed. For the tracker muon, the track is reconstructed in the tracker and matched to compatible segments in the muon system. The final muon track fit is done with information only from the tracker.

4.1.2.2 *Global Muon*

The muon momentum resolution is dominated by multiple scattering up to $p_T = 200\,GeV$ for muons reconstructed in the muon system. So the tracker muon is the best choice for this momentum range. Above that, the muon system allows to improve the momentum resolution by combining tracker and muon system information. For this algorithm, all hits from the tracker and from the muon system are taken into account for the final track fit.

4.1.2.3 *TPFMS Muon*

The muon momentum resolution is given by the curvature of the muon track and therefore by $\sim \frac{1}{(BL)^2}$ with the magnetic field B and the length L. Because of this relation, it is helpful to take the hits in the muon system into account. But multiple scattering and/or showering can corrupt the measurement due to hits that can not be connected to the track. Therefore using multiple muon stations is not always an advantage. To combine the information from the muon system, but avoid the problems of multiple muon stations, the tracker-plus-first-muon-station (TPFMS) algorithm takes the hits from the tracker and only the first valid hit in the muon system for the final track fit into account [73].

4.1.2.4 *Picky Muon*

Another approach to reduce accuracy loss due to showering in the muon system is to only take muon stations with no shower. Or use hits which are compatible with the muon track. In order to detect if a shower happened in a muon station, the occupancy of the muon stations is used. For these stations the χ^2/NDF of each hit with the muon track is calculated. If it is below the threshold (10 for DT, 150 for CSC and 1 RPC), the hit is taken into account for the track fit [74].

4.1.2.5 *TuneP Muon*

The TuneP or 'Cocktail'-algorithm is designed to extract the best muon candidate from the different reconstruction methods. For this Tracker, Global, TPFMS and Picky muons are considered. The algorithm is summarized in the following step by step list [75]:

1. Check if at least one muon with $\frac{\Delta p_T}{p_T} < 0.25$ exists, if not raise threshold by 0.15 and check again. The Δp_T is the uncertainty on p_T, resulting from the uncertainty on the track parameters in the track fit. The procedure is repeated until at least one muon is found the fulfills that requirement, all other muons are marked as invalid[5].
2. Start by choosing the Picky muon as default.
3. Check if Picky muon is valid[6]. If not, choose Tracker muon.
4. If the Picky muon is chosen, check if the probability $P(\mathrm{Picky}) - P(\mathrm{Tracker}) > 17$, where P is defined as :

$$P(\chi^2, \mathrm{NDF}) = -\log\left(\int_0^{\chi^2} \frac{t^{\frac{\mathrm{NDF}}{2}-1} e^{-\tilde{}\frac{t}{2}} dt}{\Gamma\left(\frac{1}{2}\mathrm{NDF}\right) \cdot 2^{\frac{\mathrm{NDF}}{2}}}\right) \tag{4.1}$$

   the negative logarithm of the probability to get the same or smaller χ^2 for the track fit
5. Check if Tracker muon is valid[6]. If not, choose TPFMS muon.
6. Check if TPFMS muon is valid[6]. If not, choose Global muon.
7. Compare the chosen muon to TPFMS and if $P(\mathrm{chosen}) - P(\mathrm{TPFMS}) > 40$ choose TPFMS.
8. If tracker p_T or chosen $p_T < 200\,\mathrm{GeV}$, choose the Tracker muon.

As a comparison the resolutions are shown in Fig. 4.1 for tracker, global and TuneP muons determined from cosmic muons (see Ref. [76]). Especially for high p_T the resolution of TuneP muons is significantly better compared to the other reconstruction algorithms.

4.1.3 *Muon selection*

For the final muon selection the recommendation is to use the "Tight Muon ID" plus some additional requirements for high momentum muons (referred to as "high-p_T muon ID") [77]. The different cuts are listed and explained in the following.

- The muon is required to be a global muon and a tracker muon at the same time, which reduces mismatches between tracker reconstruction and hits in the muon system.
- The muon must contain at least one hit from the muon detector in the global track, to avoid misreconstruction.
- The muon must at least have one hit from the pixel detector in the global track, to have a good estimation of the primary vertex.
- The muon track must have muon segments in at least two muon stations. This reduces punch-trough events (events with no muon which are not contained in the calorimeters and leave hits in the muon system).

5 This is important for this analysis, because just one mismeasured muon at high p_T can change the result of the analysis.

6 In this context, valid means that the reconstructed track exists and the reconstruction did not fail.

- The transverse impact parameter (smallest distance between track and beam spot in the $r-\phi$-plane) with respect to the beamspot has to be less than 0.2 mm in order to reduce cosmic background.

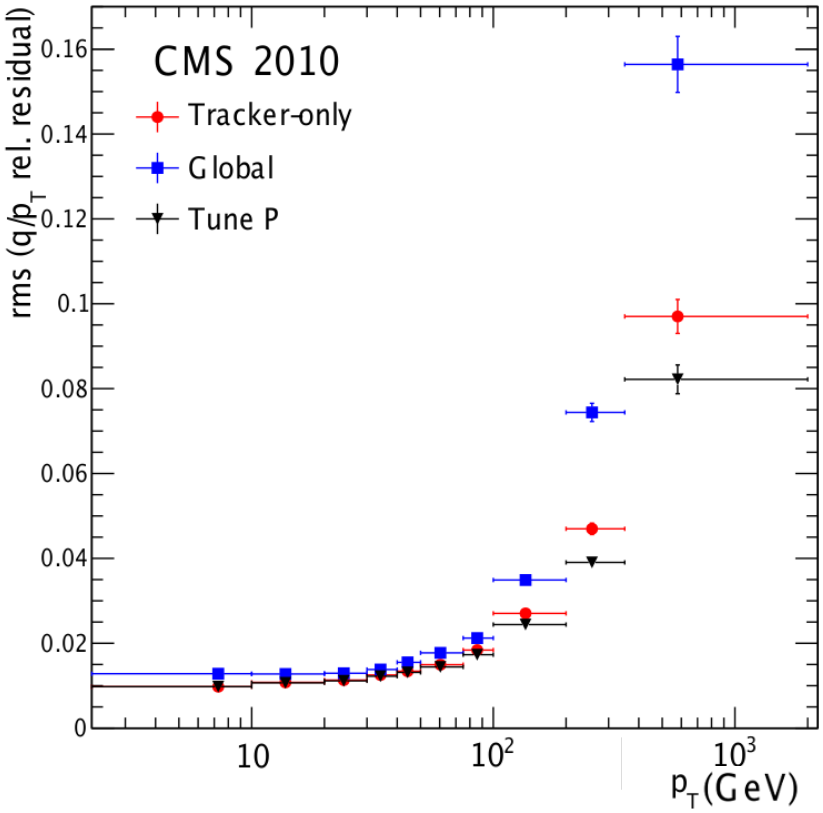

Figure 4.1: Muon p_T resolution: Shown are Tracker, Global and TuneP muon, calculated from cosmics events in 2010 [76] and confirmed with newer data of 2011 [11].

- The longitudinal distance of the tracker track with respect to the primary vertex has to be $d_z < 5$ mm.
- To guarantee a good p_T measurement, more than five tracker layers with hits are required.
- In order to suppress muons with largely mis-measured p_T, an additional requirement of $\Delta p_T/p_T < 0.3$ is applied.
- To account for the trigger acceptance, the muon is required to have $|\eta| < 2.1$.

Additional analysis cuts are applied and listed in the following.

- The leading muon has to have $p_T > 45$ GeV to avoid the trigger turn on region[7].
- To be sure that the muon is also the muon that fired the trigger, it is required to be in a cone of $\Delta R < 0.5$ around the trigger object ($\Delta R = \sqrt{\Delta\phi^2 + \Delta\eta^2}$).

7 The trigger turn on is the p_T range where the trigger efficiency increases from zero to its plateau value (Sec. 6.3).

- We require at least one good reconstructed vertex with $|z| < 24\,\mathrm{cm}$ (position of the vertex in z direction), $N_{dof} > 4$[8] and to have a valid fit for the vertex.
- No more than one global muons in the event with tracker track $p_T > 25\,\mathrm{GeV}$, in order to reduce Drell-Yan and cosmic background.
- A tracker-based relative isolation is applied, where the measured p_T of tracks in a $\Delta R < 0.3$ cone around the muon direction are summed up and divided by the muon p_T, it has to be smaller than 0.1.

$$\left(\sum_{\Delta R<0.3} p_T\right)/p_T^{\mu} < 0.1 \tag{4.2}$$

The cut on $\Delta p_T/p_T$ is new compared to previous analyses. It affects only very few events at high p_T, but these events are quite important, as the analysis is sensitive to very few events at high p_T where few background events are expected. To have a cross check on this $\Delta p_T/p_T$ cut, the values for $\Delta p_T/p_T$ are plotted against p_T in Fig. 4.2 and normalized for each p_T bin. The distribution is made without any requirements to the muon other than the trigger. It shows the few events at high p_T with a big mis-measurement and the cut on $\Delta p_T/p_T < 0.25$ from the cocktail algorithm. For low p_T ($\mathcal{O}\,(< 700\,\mathrm{GeV})$), most muons are reconstructed with small uncertainties ($< 10\,\%$), at higher p_T the number of muons reconstructed with small uncertainties is comparable to the number of muons with big uncertainties.

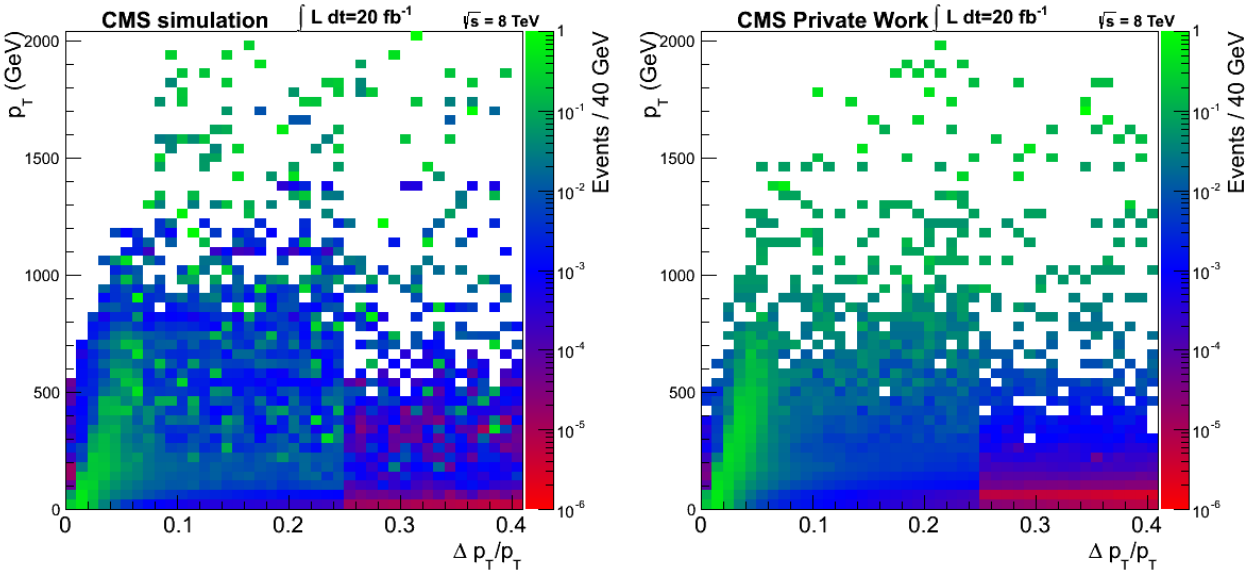

Figure 4.2: $\Delta p_T/p_T$ versus p_T distribution for background Monte Carlo (left) and data (right): Both plots are normalized in each p_T bin to make the center of the distribution visible. As expected the ratio of badly reconstructed muons ($\Delta p_T/p_T > 0.25$) to well reconstructed ones increases with p_T. At $p_T > 1000\,\mathrm{GeV}$ the numbers of good and bad muons are comparable. The cut at $\Delta p_T/p_T < 0.25$ of the cocktail algorithm is clearly visible.

8 The number of degrees of freedom for a three dimensional vertex that is only constraint by n tracks: $N_{dof} = 2 \cdot n - 3$ [78].

4.2 MISSING TRANSVERSE ENERGY

The missing transverse energy (MET) or $\not{E}_T$ is the measurable representation of not measured particles like neutrinos in the plane transverse to the beam direction. It can be reconstructed from calorimeter information only, called calo-MET[9] or by the particle-flow algorithm using all detector systems. In the following parts the reconstruction of $\not{E}_T$ (Sec. 4.2.1), the filtering of events with $\not{E}_T$ (Sec. 4.2.2) and the corrections to the ${\not{E}_T}^{raw}$ (Sec. 4.2.3) are discussed.

4.2.1 *MET Reco*

For the reconstruction of $\not{E}_T$ three different algorithms can be used: The so called Calo $\not{E}_T$, reconstructed only from calorimeter information[9], the PF $\not{E}_T$, reconstructed by the particle-flow algorithm and the TC $\not{E}_T$ which takes tracker information into account to improve the Calo $\not{E}_T$. Because it has the best $\not{E}_T$-resolution, the PF $\not{E}_T$ is used in this analysis [79].

The particle-flow algorithm reconstructs and categorizes all stable particles in an event (electrons, muons, photons, charged hadrons and neutral hadrons) by combining information from all CMS sub-detectors. The information from the sub-detectors are processed in form of particle tracks and calorimeter clusters. These basic building blocks are then used by the particle flow algorithm to reconstruct the stable particles (details in Ref. [80]).

The uncorrected PF $\not{E}_T$ is the negative vector sum of the momenta $p_{T,i}$ of all particle-flow objects in the event [81]:

$${\not{E}_T}^{uncorr} = -\sum_i p_{T,i} \tag{4.3}$$

There are known detector effects not included in this PF $\not{E}_T$, therefore different corrections need to be applied to it. They are explained in the following sections.

4.2.2 *Met Filters*

Many instrumental and reconstruction effects can be the cause of fake $\not{E}_T$ in the sense, that fake $\not{E}_T$ does not correspond to real undetected particles from collisions. To account for this effects a variety of filters is used. The $\not{E}_T$-Filters recommended by the JET/MET group are [82, 83]:

- CSC tight beam halo filter: Interaction of the proton bunches with the LHC or the rest gas in the beam pipe can produce particles with very high η. Theses so called beam halo particles can be the source of $\not{E}_T$. By using the information from the CSC these events can be vetoed [84].
- HBHE noise filter with isolated noise rejection: This filter tries to detect instrumental anomalous noise in the HCAL which can be a source of $\not{E}_T$ by looking at timing, pulse shape, hit multiplicity and other variables [85].
- HCAL laser filter: The laser used for calibrate of the HCAL has fired at times where it has influences on physics data. The events affected by this are rejected [86].

9 Calo-MET is corrected for reconstructed muons, therefore taken also information from the muon system into account.

- ECAL dead cell trigger primitive filter: Some crystals in the ECAL are masked in the reconstruction because they are either not operational or have a high level of noise. If a physical particle hits these crystals, their energy is not reconstructed, resulting in $\not{E}_T$ [87].
- Tracking failure filter: Due to events where the hard interaction does not happen in the center of the detector or events with too many clusters, which can make the tracking algorithm fail for some iterations. These events are vetoed by $\sum p_T^{track}/HT < 0.1$ with the sum of the jet energy HT[88].
- Bad EE Supercrystal filter: Two ECAL endcap supercrystals give anomalously high energies, resulting in very high $\not{E}_T$.
- ECAL Laser correction filter: Due to unphysical large transparency corrections factors for some crystals they became very energetic, resulting in $\not{E}_T$.
- Tracking POG filters: This collection of filters vetoes events where the tracking algorithm is aborted due to, for example, coherent noise [89].

Events where at least one of the recommended Filters fires are rejected[10].

4.2.3 *Met Corrections*

The $\not{E}_T$ must be corrected for a variety of known effects. The first is to correct the $\not{E}_T$ which is calculated from the particle-flow objects in the event for the difference between the muon reconstructed by the particle-flow algorithm and the muon reconstructed by the cocktail algorithm which is used in the analysis. This correction can be done by recalculating the $\not{E}_T$ with the cocktail muon.

The $\not{E}_T$ is also corrected for effects of the jet energy scale, called type-I correction, and the known ϕ-modulation by the formula:

$$\not{E}_T{}^{corr} = \not{E}_T{}^{uncorr} + C_T^{type1} - C_T^{\phi-corr} \tag{4.4}$$

This corrections are explained in more detail in the following. The last correction for $\not{E}_T$ is to correct for a discrepancy between the simulation and measurement of the hadronic recoil against W or Z boson production, which is explained in the last part of this section.

The $\not{E}_T$ is dominated by the high p_T muon for high M_T values, therefore the effect of the correction is smaller at high M_T. The ratio of the M_T distribution calculated with the corrected $\not{E}_T$ and the distribution calculated with the corrected $\not{E}_T$ is shown for data in Fig. A.3 and Monte Carlo events in Fig. A.4 in the appendix. As expected the effect of the correction is bigger for smaller M_T and only effects single events at high M_T.

10 About 1 % of the data events and 0.05 % of the Monte Carlo events are rejected. The Monte Carlo rate is a measure for good events, being rejected, because the effects that should be rejected are not included in the simulation.

4.2.3.1 *Type-1 correction*

The first term is the contribution to the particle-flow-$\not\!\!E_T$ from the particle-flow objects which are clustered as jets whose energies are above the threshold and which are corrected for the offset. The Type-I correction replaces $p_{T,jet}$ with $p_{T,jet}^{L123}$:

$$C_T^{type1} = -\sum_{p_{T,jet}^{L123}>10GeV} \left(p_{T,jet}^{L123} - p_{T,jet}\right) \tag{4.5}$$

This correction is a propagation of the L1, L2 and L3 jet energy corrections (JEC) to particle-flow-$\not\!\!E_T$ [90, 91], which can be split into three different levels:

- Level 1: Offset: This correction subtracts contributions from pile-up and electronic noise from the jet energy and it also accounts for energy losses due to energy thresholds in the detector.
- Level 2: Relative (η): This level corrects for jet response variations as a function of the pseudo rapidity η to get a flat response.
- Level 3: Absolute (p_T): This level corrects any overall offset which is left after the level 2 correction, to get a flat response with an absolute value of 1. This correction is a function of p_T.

All these corrections are derived from measured pp collision events.

4.2.3.2 ϕ-*correction*

As seen in 2011 data taking, there is a modulation in the $\phi_{\not\!\!E_T}$-spectrum in data and Monte Carlo because of not symmetric detector components and not fully simulated missing or not working detector parts [92]. This $\phi_{\not\!\!E_T}$ can be measured in $Z \to \mu\mu$ events and corrected, by applying the correction as indicated in Eq. 4.4:

$$C_T^{\phi-corr} = \begin{pmatrix} c_{x_0} + c_{x_s} \cdot N_{vtx} \\ c_{y_0} + c_{y_s} \cdot N_{vtx} \end{pmatrix} \tag{4.6}$$

The values of the parameters used for the ϕ-correction are determined by the JET/MET group [93, 94] and are listed in Tab. 4.1. The effect in this analysis is small because for high M_T, $\not\!\!E_T$ is dominated by the muon measurement.

Parameter	c_{x_0} (GeV)	c_{x_s} (GeV)	c_{y_0} (GeV)	c_{y_s} (GeV)
Data	0.048	0.249	−0.150	−0.083
Simulation	0.163	0.024	0.361	−0.130

Table 4.1: Parameters for ϕ-correction.

The effect of this correction can be seen in Fig. 4.3 where the uncorrected $\phi_{\not\!\!E_T}$-(left) and the corrected $\phi_{\not\!\!E_T}$-spectrum(right) are shown. The requirement for all events in the distributions is, that they fulfill the muon selection.

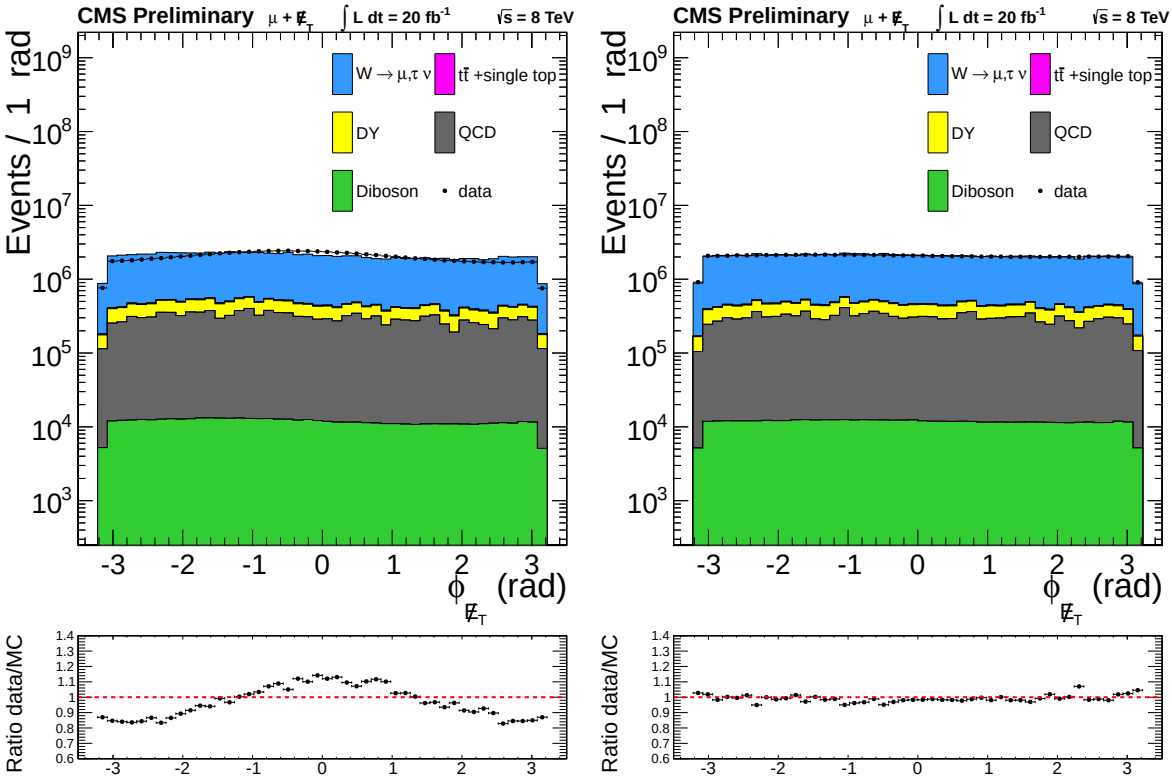

Figure 4.3: $\phi_{\not\!\!E_T}$-spectrum: before correction (left) and after correction (right). All events that fulfill the muon selection are shown, and Monte Carlo is scaled to data, to see the shape differences.

4.2.3.3 *hadronic recoil correction*

The hadronic recoil against a W or Z boson is defined as:

$$\vec{u} = -(\not\!\!E_T + \vec{q}) \tag{4.7}$$

with the boson momentum $\vec{q}$. Due to bad simulations of this recoil, especially for small values of $|\vec{u}|$ this can be a source of disagreement between the Monte Carlo simulation and the measurement. To study this further, the recoil $\vec{u}$ is split into the component $u_{\parallel}$ parallel to the direction of the boson and perpendicular to this direction $u_{\perp}$. The recoil parallel to the boson direction is defined as

$$u_{\parallel} = \frac{\vec{u} \cdot \vec{q}}{|\vec{q}|} = -q_T \tag{4.8}$$

while the perpendicular component is defined as

$$u_{\perp} = \frac{\vec{u} \times \vec{q}}{|\vec{q}|} = 0 \tag{4.9}$$

As already denoted in Eqn. 4.8 and 4.9 the expected value for the parallel component $u_{\parallel}$ is the negative of the boson transverse momentum q_T, while the expectation for the perpendicular component $u_{\perp}$ is zero. To compare the Monte Carlo prediction to data we use events with two muons which pass our selection and have an invariant mass around the Z boson mass ($80\,\text{GeV} < m_{\mu\mu} < 100\,\text{GeV}$). For this selected events we calculate $u_{\parallel}$ in Monte Carlo and in data as a function of the boson q_T shown in the left plots of Fig. 4.4. To get a

better description of this plots they are separated in slices of boson q_T and in each slice a gaussian is fitted to the $u_{\parallel}$-distribution. The negative mean $-\langle u_{\parallel} \rangle$ of these fitted gaussians is shown in the middle plots of Fig. 4.4. To compare this result to the prediction that the parallel recoil component $u_{\parallel}$ is proportional to the boson q_T in the right plots of Fig. 4.4 the ratio of the parallel recoil component $-\langle u_{\parallel} \rangle$ and the boson q_T is shown which lies around one, as expected.

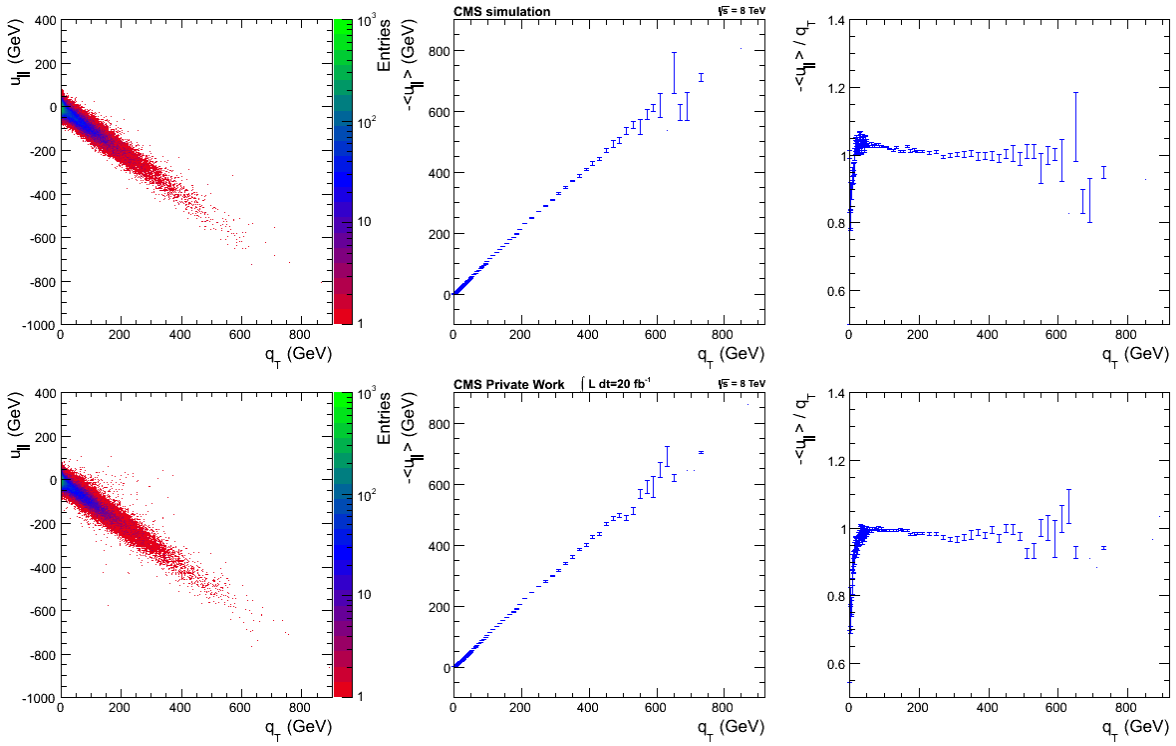

Figure 4.4: Parallel recoil component $u_{\parallel}$ for Z events ($80\,\text{GeV} < m_{\mu\mu} < 100\,\text{GeV}$) from Monte Carlo simulation (top row) and from data (bottom row): In the left column the parallel recoil component $u_{\parallel}$ is shown against the boson q_T. In the middle column the negative mean parallel recoil component $-\langle u_{\parallel} \rangle$ is shown against the boson q_T. This mean component is calculated by fitting a gauss function in every boson q_T slice, the mean of this gauss function gives the mean parallel recoil component $\langle u_{\parallel} \rangle$. In the right column the ratio of the negative mean parallel recoil component $-\langle u_{\parallel} \rangle$ and boson q_T against the boson q_T is shown, as expected it is very close to one.

To get a correction for the analysis, the difference between the Monte Carlo description and the data is important. For this correction the ratio of Monte Carlo and data events of the center plots in Fig. 4.4 is calculated. For the correction of the *W* simulation it is assumed, that kinematic of *W* production is comparable to Z production. As the recoil jet is QCD initial state radiation it is independent of the boson decay the assumption is reasonable.

This data/Monte Carlo ratio is then used to correct the parallel recoil component $u_{\parallel}$ of the simulated W events on generator level. The same uncorrected distributions as before for W events on generator level are shown in Fig. 4.5.

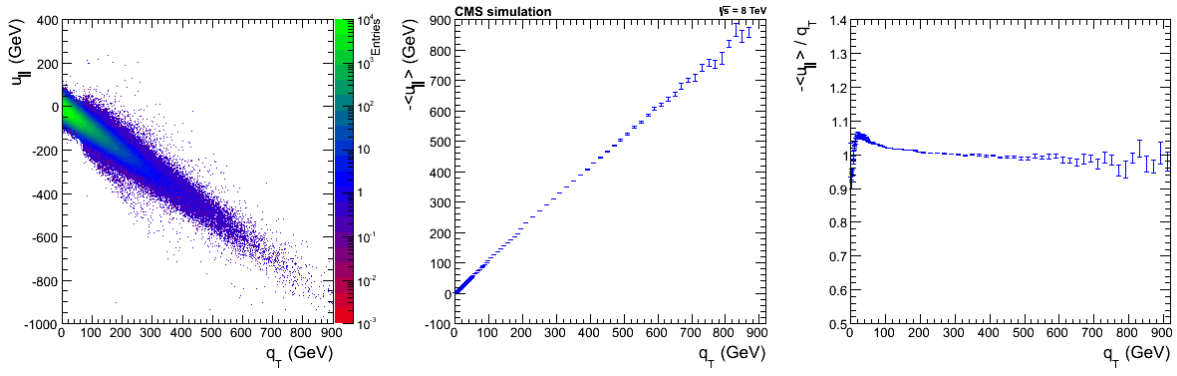

Figure 4.5: Uncorrected parallel recoil component $u_{\parallel}$ for W events on generator level: The plots show the same quantities as in Fig. 4.4, the parallel recoil component $u_{\parallel}$ against the boson p_T, the negative mean parallel recoil component $-\left\langle u_{\parallel} \right\rangle$ against the boson q_T and the ratio of negative mean parallel recoil component $-\left\langle u_{\parallel} \right\rangle$ and boson q_T against boson q_T.

To get a smooth description of this ratio, it is parametrised with the function $f(x = q_T) = a + e^{b+c\cdot x}$. The ratio, the parametrisation and its parameters are shown in Fig. 4.6. The difference to one of this correction is small and only for very small boson q_T relevant.

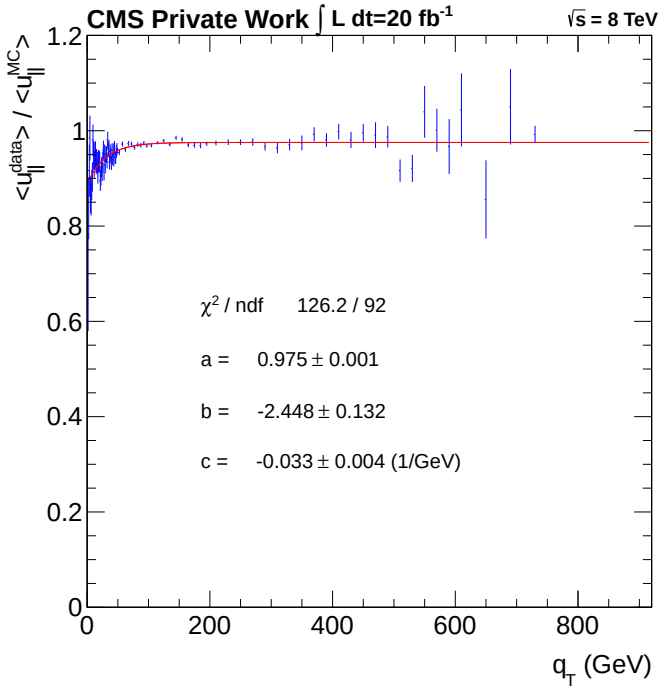

Figure 4.6: Ratio of the mean parallel recoil component against the boson q_T for Z events of Monte Carlo description and data: The distribution is than parametrised by the function $f(x = q_T) = a + e^{b+c\cdot x}$ to get a smooth description. The values for the parameters of the parametrisation and there errors are given in the plot. This parametrisation is then used to correct the *W* simulation.

5 SAMPLE

In this section the different data (Sec. 5.1), background Monte Carlo (Sec. 5.2) and signal Monte Carlo (Sec. 5.3) samples used in this analysis are introduced. One sample means a collection of events for some specific physical process simulated with one specific Monte Carlo generator, or a data sample, where events which have fired a specific trigger are collected.

All events that end up in the final M_T distribution have to pass all selection steps and corrections explained in Sec. 4 and have to pass the kinematic selection explained in Sec. 6. The search region in the final M_T distribution is $M_T > 220\,\text{GeV}$.

5.1 DATA

This analysis uses 2012 proton-proton collision data with a center-of-mass energy of $8\,\text{TeV}$. The datasets were reconstructed with the software CMSSW_5_3_x. The used dataset is not the so called prompt-reco (the data which are reconstructed just after recording), but the re-reco from 22.Jan.2013 (re-reconstruction with all available information on alignment and detector conditions from the whole data taking period).

Table 5.1 shows a summary of the chosen datasets with the corresponding triggers, run ranges and integrated luminosities.

Dataset	Trigger	Run Range	$\mathcal{L}_{int}$ $\left(\text{fb}^{-1}\right)$
/SingleMu/Run2012A-22Jan2013-v1/AOD	HLT_Mu40_eta2p1	190456-193621	1.1
/SingleMu/Run2012B-22Jan2013-v1/AOD	HLT_Mu40_eta2p1	193834-196531	4.9
/SingleMu/Run2012C-22Jan2013-v1/AOD	HLT_Mu40_eta2p1	198022-203742	7.4
/SingleMu/Run2012D-22Jan2013-v1/AOD	HLT_Mu40_eta2p1	203777-208686	7.7

Table 5.1: List of the datasets used in the analysis with the corresponding trigger, run ranges and integrated recorded luminosity.

To select good runs the JSON file provided by the data certification group is used

$$\texttt{Cert\_190456-208686\_8TeV\_22Jan2013ReReco\_Collisions12\_JSON.txt}$$

which corresponds to an integrated luminosity of $19.8 \pm 0.5\,\text{fb}^{-1}$. For events that are listed in the JSON file the certification group has checked that all parts of the detecter were working fine, and these certified events can be used for the analysis [95].

5.2 BACKGROUND MONTE CARLO

Monte Carlo (MC) simulated samples are used to evaluate signal and background efficiencies. Generated events are processed through the full GEANT4 [96, 97] detector simulation, trigger emulation and event reconstruction chain of the CMS experiment. Processes which contribute to the background need to contain a high momentum muon and $\not{E}_T$ or objects

which can be misidentified or misreconstructed as a muon and $\not{E}_T$. To pass the selection, they also need to have the kinematic properties of the signal, back-to-back muon and $\not{E}_T$. The processes which contribute to the background are listed in the following in decreasing order of importance (a detailed list of the used MC samples is given in the Appendix A.2). How much the different processes contribute to the background and how high the selection efficiency is for the different processes is shown in Tab. 5.2. The effect of the different selection steps on different background contributions and the comparison to data is illustrated in Fig. 5.1a. All Monte Carlo samples were generated with consisting PDF sets, meaning NLO samples were generated with NLO PDFs and LO samples were generated with LO PDFs.

- $W \to \mu\nu$: The main background is Standard Model W production with high transverse masses in the tail of the jacobian W peak. This process looks exactly like the studied signals, as it produces back-to-back a high p_T muon balanced with $\not{E}_T$ from the neutrino and is therefore indistinguishable from the signal. As this is the most important background, a more detailed view of the different available simulations is useful. There are three different samples available. The first is a PYTHIA [98] sample binned in $\hat{p}_T$ (scale of the hard interaction) into three samples ($\hat{p}_T > 500\,GeV$, $100 < \hat{p}_T < 500\,GeV$, and one sample produced over the full $\hat{p}_T$ range) separately for W decay into muon and decay into tau generated at leading order (LO). A correction factor (k-factor) binned in M_T is applied to the PYTHIA sample to correct the differential cross section for higher order effects (Sec. 5.2.1). The second is a combined μ, e, τ sample generated with MADGRAPH [99], also at LO. The third possibility is a POWHEG [100, 101, 102] sample, split into μ and τ, but also in W^+ and W^- generated in next-to-leading order (NLO). The transverse mass spectrum and ratio for all three possibilities is shown in Fig. 5.1b. It is clear that the MADGRAPH sample has not enough events at high transverse masses. The PYTHIA and POWHEG spectra are quite comparable, but the statistics in the PYTHIA sample is higher because the sample is binned in $\hat{p_T}$. Therefore, the PYTHIA samples are used to describe the W background. The NLO corrections to this LO sample are summarized in Sec. 5.2.1.

- $W \to \tau\nu$: This background process can be important if the W decays into a τ and ν_τ, and the τ subsequently decays into a μ and two ν. This has the same properties as the $W \to \mu\nu$ decay, and is also indistinguishable from the signal, but while the branching fraction of $W \to \tau\nu$ is the same as $W \to \mu\nu$, the branching fraction for a τ to decay into μ and ν's is only $17.41 \pm 0.04\,\%$ [33], reducing the contribution by more than a factor of 5. The other issue in this decay is that the 3 ν's can share any fraction of the initial energy, so while keeping the kinematic relations, the transverse mass is shifted to lower values, further reducing the contribution in the relevant M_T-region ($M_T > 220\,GeV$). The contribution of muons from tau decays is also relevant in signal processes and therefore studied in Sec. 5.3.2 for signal and background. The sample used is, as mentioned for $W \to \mu\nu$, the PYTHIA sample binned in three $\hat{p}_T$-bins and corrected with the binned k-factor.

- Top: The production of top quarks can be either pair production ($t\bar{t}$) or single top production. Both processes can contribute to the background as the top decays in all of the cases to a W and a lighter quark and the W can subsequently decay into a muon and a neutrino. The process can contribute to the background because the W and therefore the muon is highly boosted due to the high top mass. But the kinematic relations are not the same as for the signal due to additional hadronic jets of the quarks. The

background contribution is therefore significantly reduced as can be seen in Fig. 5.1a. Single top production was simulated with POWHEG (hadronic showering simulated with PYTHIA) and scaled to an approximative next-to-next-to-leading order (NNLO) cross section [103]. The pair production is simulated with MC@NLO [104] (hadronic showering simulated with HERWIG [105, 106]) and scaled to the latest NNLO cross section [107].

- Diboson: The production of two bosons WW, WZ and ZZ is also important if the W or Z decays into muons with $\not{E}_T$ from either neutrinos or mismeasured hadronic jets. The samples where produced with PYTHIA for the three boson combinations each time with two samples (with the minimum boson p_T greater than 500 GeV and over the full range) in LO. The samples were scaled to the NLO cross section.

- DY: The Drell-Yan process $q\bar{q} \to \ell\bar{\ell}$ can contribute to the background if $\ell = \mu$ and one muon is not correctly measured or $\ell = \tau$ and only one tau decays into a muon. In both cases, $\not{E}_T$ comes from the missing measurement of the second muon or the mismeasurment of the hadronic tau jet. The process where $\ell = \mu$ was simulated with POWHEG at NLO, while the process where $\ell = \tau$ was simulated with PYTHIA at LO and a uniform QCD k-factor of 1.26 was applied.

- QCD: The multijet background of jet production via the strong interaction (therefore called QCD) has the largest cross section but high p_T muons and $\not{E}_T$ are not produced with the signal kinematics at high rates. The requirement of only one high p_T muon reduces this background very much (see Fig. 5.1a: Single muon and $p_T > 110$ GeV cut). This background is simulated in a muon enriched sample produced with PYTHIA in LO. Because QCD can only be calculated with perturbation theory at high energies, the low energy part of the reaction has to be simulated with qualitative models (called hadronization). To avoid the difficulty in producing a good simulation for the QCD background, many analyses use a data driven approach to estimate QCD background from a signal free control region. An example for such a region would be a region with high p_T muons but only little $\not{E}_T$ (a high $p_T/\not{E}_T$ ratio). This region is shown in Fig. 6.1 where the data-Monte Carlo agreement is quite good even for large $p_T/\not{E}_T$ ratios. Because of that, the Monte Carlo description is used in this analysis to describe the QCD background. Another reason is that the QCD background contributes only $< 1\,\%$ to the whole background (Tab. 5.2) and a good background modeling is therefore less important than for the other processes.

All Monte Carlo samples were scaled to the integrated luminosity $\mathcal{L}$ of the data with the weight

$$w = \frac{\mathcal{L} \cdot \sigma}{N_{ev}} \tag{5.1}$$

from the cross section σ and the event number N_{ev} of the sample (the numbers for all used samples are given in Sec. A.2 in the appendix).

The simulation of pile-up (interactions that happen in the same bunch crossing, but do not contain interesting physics for this analysis) is included in all Monte Carlo samples by superimposing simulated minimum bias interactions (events with a much lower event rate, to not be biased by a trigger or other selections) onto all simulated events (details on the treatment of pile-up in this analysis is given in Sec. 6.2).

process	event numbers	fraction (%)	efficiency
$W \to \mu\nu$	$17\,275 \pm 170$	80.8	$4.90 \cdot 10^{-5}$
$W \to \tau\nu$	337 ± 4	1.8	$1.36 \cdot 10^{-6}$
Top	$2\,759 \pm 28$	12.9	$3.87 \cdot 10^{-4}$
Diboson	652 ± 8	3.0	$3.37 \cdot 10^{-4}$
DY	237 ± 7	1.1	$3.08 \cdot 10^{-6}$
QCD	87.8 ± 56.6	0.4	$1.46 \cdot 10^{-9}$
All BG	$21\,469 \pm 224$	100.0	$3.55 \cdot 10^{-7}$
Data	22 570		

Table 5.2: Different background contributions to the final M_T distribution: The different processes and the event numbers for $M_T > 220\,GeV$ with their statistical error are given. Also the fraction and efficiency for the different processes is listed, meaning which fraction of the produced events end up in the final distribution. As a comparison, the number of all background events and the number of observed data events is shown (all errors shown are statistical, the systematic error is $\geqslant 10\%$).

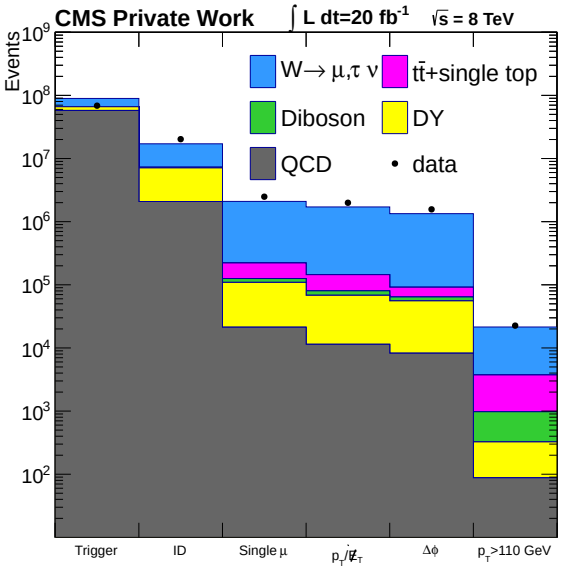

(a) Cutflow: This distribution shows the number of events after different selection steps, in a stacked histogram for the background Monte Carlo and with black markers for the data. The first bin shows the number of events that passed the trigger selection (Sec. 4.1.1) and in the second the muon ID (Sec. 4.1.3). In the third bin are the events with exactly one muon. The fourth and fifth bin are the kinematic selection (Sec. 6.1). In the last bin the muon is required to have $p_T > 110\,GeV$ which corresponds roughly to the search region of $M_T > 220\,GeV$. The different contributions in the last bin are listed in Tab. 5.2 in numbers. The distribution is also listed as a Table in the appendix (Tab. A.8).

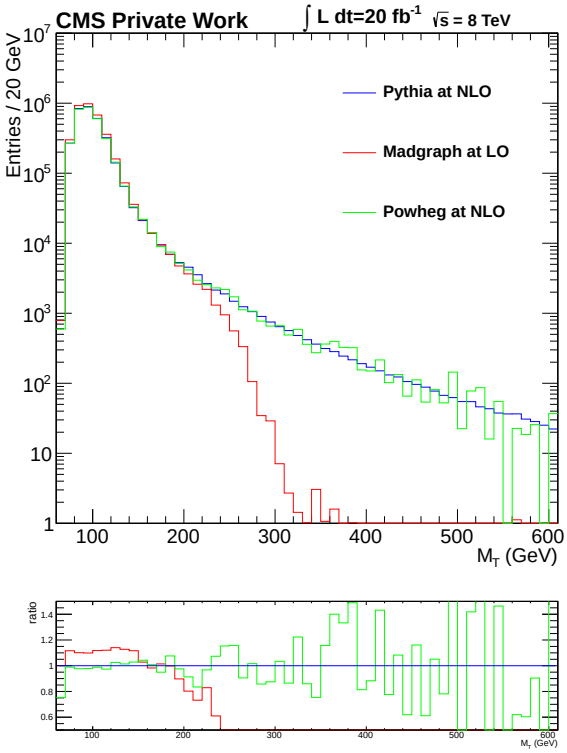

(b) Comparison of the different available W samples: Shown are the different transverse mass distributions for the PYTHIA, MADGRAPH and POWHEG sample. Also shown is the ratio compared to the PYTHIA sample. The agreement between PYTHIA and POWHEG is good, while the MADGRAPH sample does not have much events left for $M_T > 200\,GeV$, which is the interesting region for this analysis. The PYTHIA sample already contains the binned k-factor (Sec. 5.2.1), to account for NLO effects. All three samples were scaled to the same luminosity of $20\,fb^{-1}$.

Figure 5.1: Background Monte Carlo information: The cutflow (left) and the different W simulations (right) are shown.

5.2.1 *k-factor*

The Monte Carlo sample modeling the background events from W-boson production is generated using PYTHIA in LO. In order to incorporate higher order effects, a k-factor can be calculated, either for the whole distribution $k = \frac{\sigma_{(N)NLO}}{\sigma_{LO}}$ or binned for the parameter of interest M_T: $k(M_T) = \frac{\Delta\sigma_{(N)NLO}/\Delta M_T}{\Delta\sigma_{LO}/\Delta M_T}$. The calculation is derived from Ref. [108].

The NLO k-factor incorporates QCD and electroweak contributions and effects due to NLO PDF sets. The electroweak corrections were calculated by calculating the differential cross section with the event generator HORACE [109] which contains the electroweak NLO corrections. For the QCD corrections, the generator MC@NLO was used. It is also important to account for the effect of the PDFs, the correction therefore also includes the difference between the LO PDF (cteq6l1) used for the production of the sample and the NLO PDF (CT10) used to calculate the corrections. The contributions of electroweak and QCD corrections and the effect of the NLO PDF are shown in Fig. 5.2-left.

To combine the two different types of corrections, two different approaches can be applied [110]. From the electroweak differential cross section $\left[\frac{d\sigma}{d\mathcal{O}}\right]_{EW}$ and the QCD differential cross section $\left[\frac{d\sigma}{d\mathcal{O}}\right]_{QCD}$ an additive combination

$$\left[\frac{d\sigma}{d\mathcal{O}}\right]_{QCD\oplus EW} = \left[\frac{d\sigma}{d\mathcal{O}}\right]_{QCD} + \left[\frac{d\sigma}{d\mathcal{O}}\right]_{EW} - \left[\frac{d\sigma}{d\mathcal{O}}\right]_{LO} \tag{5.2}$$

and a factorized combination

$$\left[\frac{d\sigma}{d\mathcal{O}}\right]_{QCD\otimes EW} = \left(\frac{\left[\frac{d\sigma}{d\mathcal{O}}\right]_{QCD}}{\left[\frac{d\sigma}{d\mathcal{O}}\right]_{LO}}\right) \times \left[\frac{d\sigma}{d\mathcal{O}}\right]_{EW} \tag{5.3}$$

can be calculated. The k-factor is obtained by dividing this by the leading order differential cross section, shown at the bottom of Fig. 5.2-right.

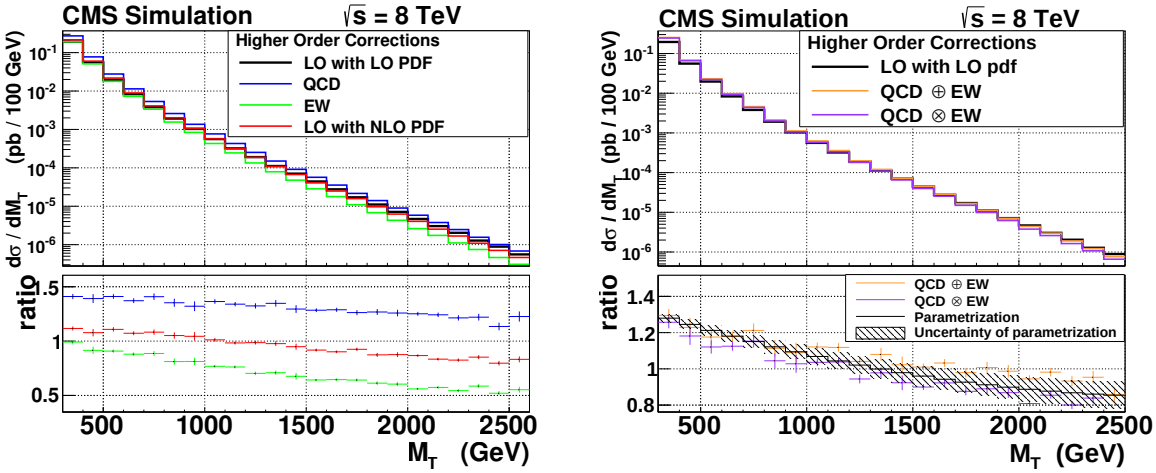

Figure 5.2: k-factor: The left plot shows the contribution of electroweak, QCD corrections, and the effect of the NLO PDF compared to the LO sample. The right plot shows both possibilities to combine electroweak and QCD corrections. In the bottom part of the right plot the parametrisation and its uncertainty are shown, it also corresponds to the actual NLO k-factor which is used in the analysis.

To avoid that statistical fluctuations have an influence on the used k-factor and therefore on the final M_T spectrum, both the additive and multiplicative combination are parametrised with a second order polynomial function. The mean of these two parametrisations is used as the final k-factor while the difference between this mean and both combinations is considered as a systematic uncertainty. Both combinations are shown in Fig. 5.2-right, the ratio, parametrisation and uncertainty is shown at the bottom of the plot.

5.2.2 *Parametrisation of the background*

The statistics of the background prediction is limited by the number of generated events. To get a smooth background prediction without the production of much more Monte Carlo events, a parametrisation of the Monte Carlo background prediction is used to avoid unphysical fluctuations in it. The function that is used for the parametrisation of the background in the range from $150\,\text{GeV} < M_T < 3500\,\text{GeV}$ is

$$f\,(x = M_T/\text{GeV}) = e^{a+b\cdot x+c\cdot x^2}\cdot x^d + e^{e\cdot x+f}\cdot\frac{100}{x} \tag{5.4}$$

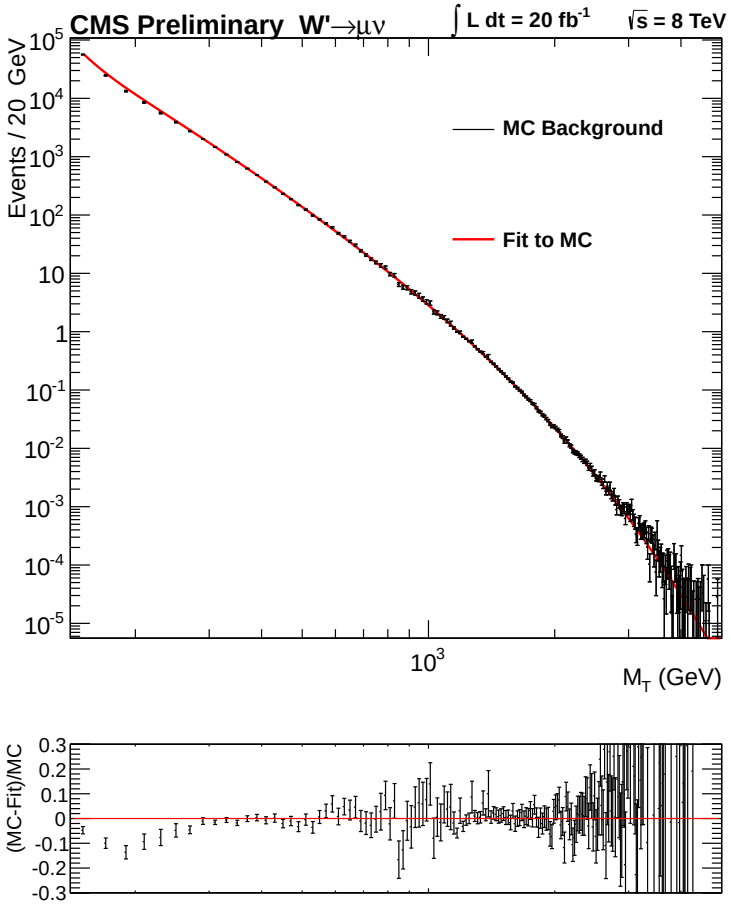

Figure 5.3: Parametrisation of the background Mote Carlo spectrum to get a smooth background prediction: The ratio at the bottom shows a good agreement between the Monte Carlo prediction with its statistical uncertainties and the parametrisation.

The first part of the function describes the spectrum in the high M_T region while the second part which is suppressed by $\frac{100}{M_T}$ at high M_T describes the edge of the W peak at lower M_T.

This parametrisation gives a smooth background prediction over the whole M_T range. The chosen function is well suited to describe the M_T distribution in MC because this function is not used to extrapolate the background but to parametrise it. The background expectation in a given search window can now be calculated using the parametrisation. As a crosscheck, these values are compared to the results of a simple cut and count of the simulated backgrounds. The agreement between both methods is good as can be seen in Fig. 5.3, especially in the ratio in the bottom of the plot. The χ^2's for the different fits are given in Tab. A.6 in the appendix. They range from $1.51 < \chi^2/\text{NDOF} < 2.92$ which indicates a reasonable agreement between the Monte Carlo prediction and the parametrisation.

5.3 SIGNAL MONTE CARLO

In this section, the Monte Carlo samples used to describe the signal are introduced. First the W' samples (Sec. 5.3.1) are summarized and especially the contribution to the signal from taus decaying into muons (Sec. 5.3.2). In the second part, the Dark Matter samples (Sec. 5.3.3) and the parametrisation of these samples (Sec. 5.3.4) are introduced. A complete list of all used signal Monte Carlo samples is given in the Appendix in Sec. A.2. In the shown plots, two example signal distributions are shown, one example for W' with a mass of $m_{W'} = 2000\,\text{GeV}$ and a Dark Matter sample with a mass $m_\chi = 300\,\text{GeV}$, $\Lambda = 600\,\text{GeV}$ and $\xi = +1$.

5.3.1 W'

Signal samples were produced for the W' decaying into a muon plus neutrino and tau plus neutrino with PYTHIA in LO. The samples were produced with $m_{W'}$ from 300 GeV up to 4000 GeV and have gone through the whole detector simulation.

Flat NNLO k-factors for $\sqrt{s} = 8\,\text{TeV}$ [111] were calculated and are listed together with the different samples and cross sections in Sec. A.2.

The generated events show a jacobian peak like the Standard Model W but at the W' mass $m_{W'}$. Three example distributions on generator level are shown in Fig. 5.4. An other feature that can be seen on generator level is the off-shell production, which increases with increasing $m_{W'}$. For high W' masses therefore the low and medium M_T part of the spectrum become important and not only the peak region around $m_{W'}$. This clear structure that can be seen in the generator information gets smeared out by the detector resolution and the clear peak structure is lost for high p_T, M_T and therefore high $m_{W'}$ after reconstruction.

5.3.2 *Contribution by $\tau \to \ell\nu$ to the signal*

As already indicated for the background processes, not only the direct production of a muon and a neutrino is interesting but also the indirect one from the decay of a tau lepton. A high p_T tau that decays via $\tau \to \mu\nu_\mu\nu_\tau$ can not be distinguished from the direct muon production process because the muon and two neutrinos are boosted in the tau direction [112].

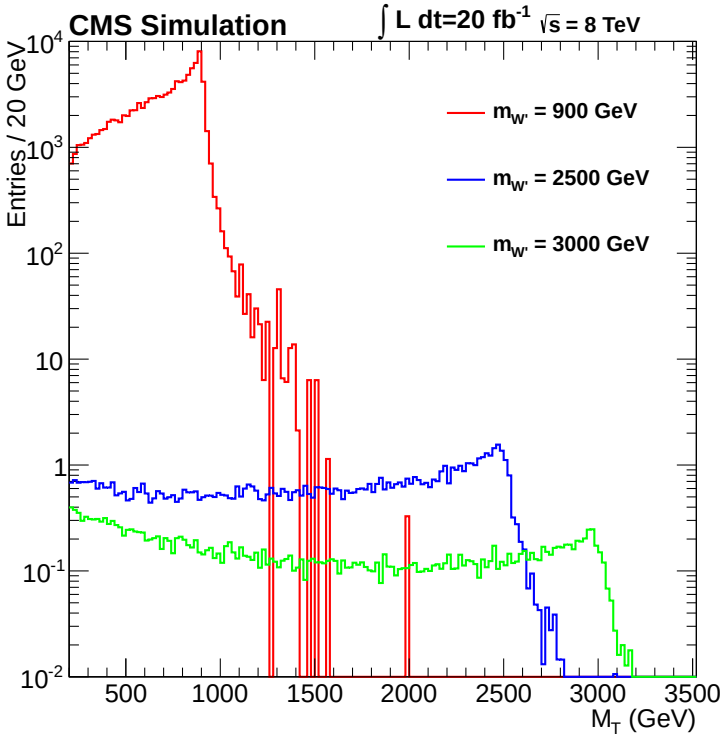

Figure 5.4: Generator level transverse mass signal distributions for three different W' masses for W' decaying directly to a muon and a neutrino: The jacobian peak structure and the increased off-shell production at low M_T for increasing W' masses can be seen clearly.

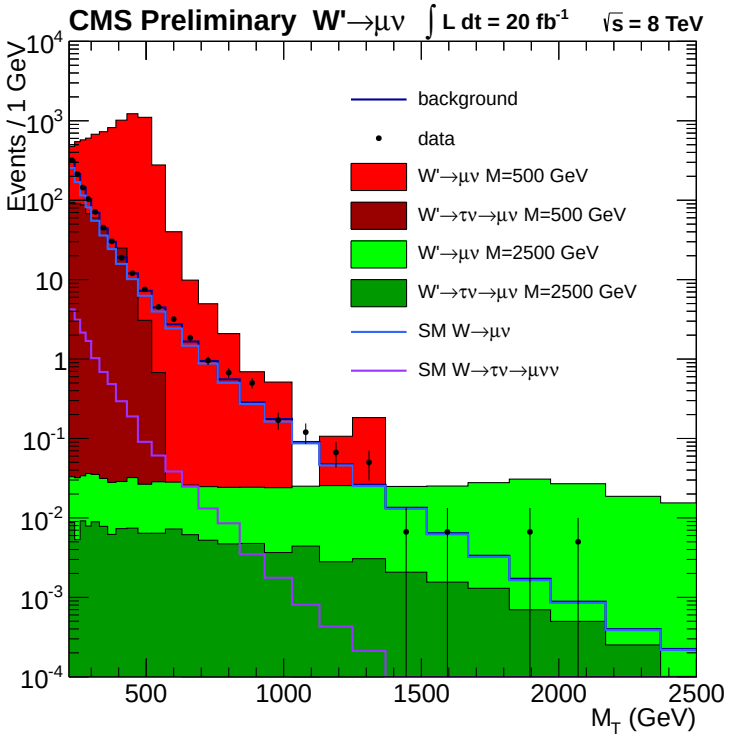

Figure 5.5: Contribution of muons from tau decays to the background (solid lines) and for two W' masses (filled histograms): As a comparison the complete background is shown in a dark blue solid line and the data in black markers.

The balanced back-to-back kinematic is conserved by the same argumentation as for the Dark Matter pair production (Sec. 3.2.2). The resulting transverse mass spectra for background and W' signal are shown in Fig. 5.5.

The ratio of indirect over direct muon production is about 1.6 % (at $M_T = 220\,\text{GeV}$) for the background and $> 19\,\%$ (also at $M_T = 220\,\text{GeV}$) for the W' signal. While the value for the signal is comparable with the branching fraction of about 17 %, the value for the background is about an order of magnitude lower. Both effects come from the fact that while the kinematic relations hold, the energy of the three neutrinos contribute to $\not{E}_T$, resulting in a shift to lower M_T compared to the direct decay, where the neutrino corresponds directly to $\not{E}_T$. In addition, one has to consider the different shapes of the transverse mass spectra for background and signal, the background spectrum is on the high energy tail of the W jacobian peak, while the signal is in the low energy tail or right on the jacobian peak. This results in the ratios for indirect over direct production at a fixed M_T value.

5.3.3 *Dark Matter*

For the Dark Matter signal 11 mass points have been generated for Dark Matter masses $1\,\text{GeV} < m_\chi < 2000\,\text{GeV}$ for vector and axial-vector coupling. A detailed list of all generated samples, their cross section and number of generated events is given in the appendix Sec. A.2. The samples were generated with MadGraph 5.1.5 [113] matched to pythia for showering and hadronization.

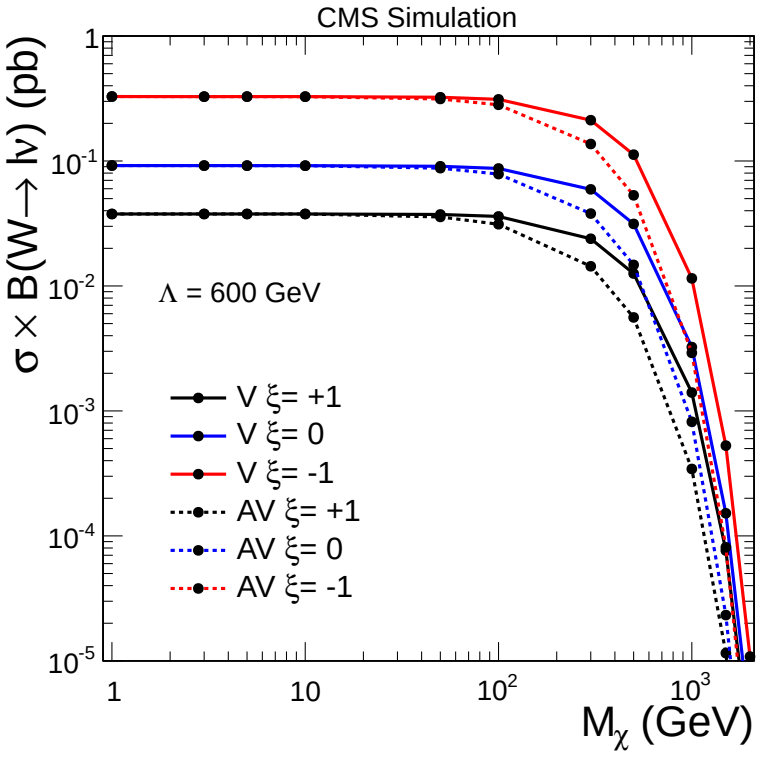

Figure 5.6: Cross section times Branching Fraction for the produced Dark Matter samples: All cross sections are for $\Lambda = 600\,\text{GeV}$. Vector coupling is shown with a solid line, while axial-vector coupling is shown by a dashed line. The colors indicate the different ξ values $\xi = 0, \pm 1$.

All samples were generated with up to one additional jet at matrix level because the process with one and the process with no additional jet have a comparable cross section. The balanced back-to-back kinematic is no longer valid if one jet is radiated, but it can still contribute to the signal and is therefore included in the simulation.

The cross sections for the two couplings and $\xi = 0, \pm 1$ are shown for the different masses m_χ in Fig. 5.6. For low masses m_χ no difference between vector and axial-vector coupling is observed. For masses above 100 GeV the axial-vector cross sections are lower than the vector cross sections, because of reduced spin phase space for the spin dependent axial-vector coupling at high x of the PDF.

The different transverse mass signal distributions are shown in Fig. 5.7. The signal has above $M_T = 220$ GeV no structure, just a flat falling spectrum. The difference between vector coupling (solid lines) and axial-vector coupling (dashed lines) is shown in Fig. 5.7-right and is dominated by the difference in cross section for high Dark Matter masses as seen in Fig. 5.6. The other much smaller difference is, that the vector coupling signal is slightly steeper. The effect of the different values of ξ is shown in Fig. 5.7-left for one example mass point. The steepness of the spectrum depends strongly on ξ. The interference scenarios can clearly be distinguished, while for $\xi = 0$ no interference occurs, the interference for $\xi = +1$ ($\xi = -1$) is destructive (constructive). Also shown is for the $\xi = 0$ case, that the Dark Matter particles coupling to up type quarks or coupling to down type quarks is comparable, which confirms the choice of one common factor ξ for the relative coupling strength between up type and down type quarks as introduced in Sec. 3.2.2.

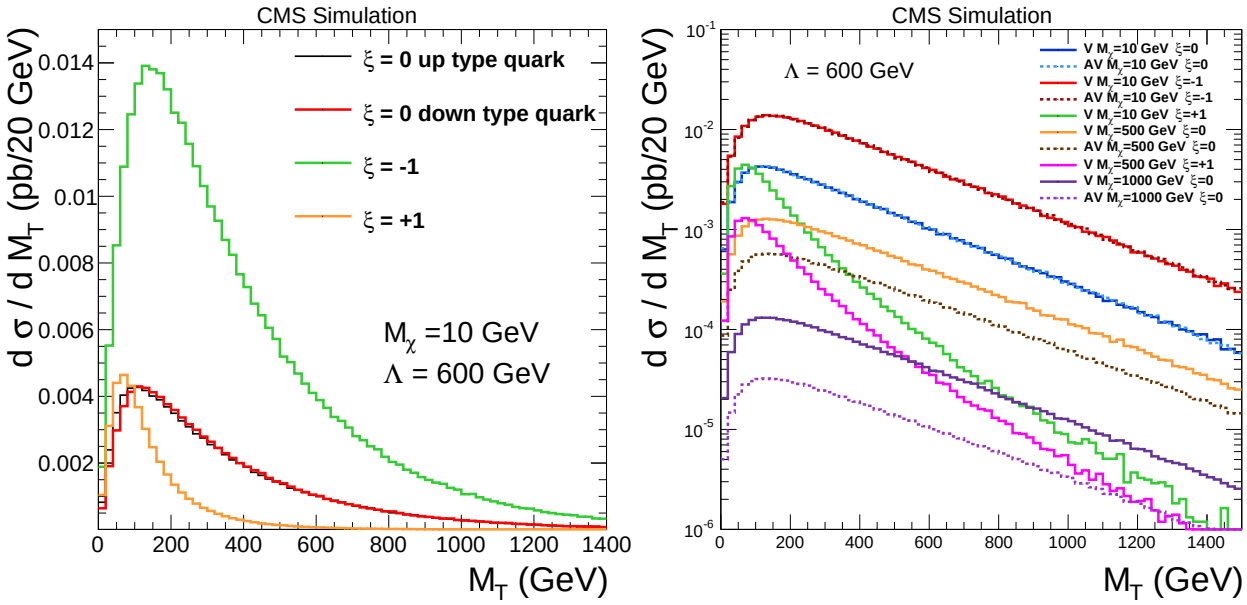

Figure 5.7: Generator level M_T distribution for different Dark Matter signal samples: The left plot shows the difference in ξ for a given mass $m_\chi = 10$ GeV. For the $\xi = 0$ case the difference between the Dark Matter particles coupling only to up type quarks and coupling only to down type quarks is shown. In the right plot in addition the effect of different Dark Matter masses is shown, which scales mainly the cross section, but does not change the shape of the distribution. The other shown effect is the difference between vector coupling (solid lines) and axial-vector coupling (dotted lines), which also just scales the cross section.

Also important to note is that the spectrum shape is independent of Λ, the signal simply scales with $\frac{1}{\Lambda^2}$, therefore the samples were all produced with a fixed $\Lambda = 600$ GeV. As there

is only a flat M_T spectrum for all values of ξ, the signals were produced for $\xi = 0, \pm 1$, but only the $\xi = +1$ samples were simulated with the full detector simulation. To get final samples for $\xi = 0, -1$, the $\xi = +1$ sample was scaled with the generator information with the reweighting factor x for each event

$$x\,(\xi, M_T\,(\text{at generator level})) = \frac{N_{ev}\,(\xi, M_T)}{N_{ev}\,(\xi = +1, M_T)} \tag{5.5}$$

5.3.4 *Dark Matter Parametrisation*

Due to a limited number of generated Monte Carlo events and the steeply falling spectrum there are not many simulated signal events with high M_T. To get a smooth prediction of the number of signal events at high M_T, the different simulated samples were parametrised with the function

$$f\,(x = M_T/\text{GeV}) = e^{a+b\cdot x} \cdot x^c \tag{5.6}$$

in the range from $150 < M_T < 2000\,\text{GeV}$. An example parametrisation is shown in Fig. 5.8-left. The cumulative comparison of the parametrisation with the Monte Carlo is shown in Fig. 5.8-right. The agreement between the fit and the Monte Carlo is quite good ($\chi^2/\text{NDOF} = 1.02$) and gives a smooth prediction of the signal at high M_T.

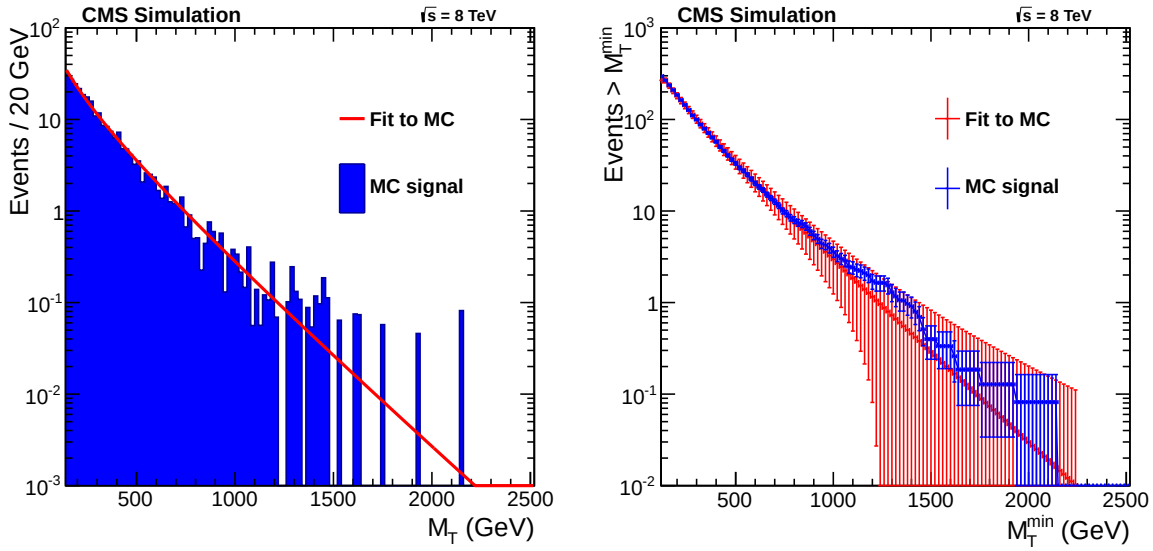

Figure 5.8: Example fit to the Dark Matter Monte Carlo sample: In the left plot the signal Monte Carlo and the parametrisation are shown. In the right plot the cumulative distribution of the Monte Carlo and of the parametrisation are shown. Both plots show good agreement between the Monte Carlo and the parametrisation. The χ^2/NDOF for this parametrisation is 1.02.

6

ANALYSIS

In this section the analysis is presented, beginning with the kinematic selection (Sec. 6.1). Then corrections on the simulation for pile-up (Sec. 6.2) and efficiencies (Sec. 6.3) are explained. The final distribution and choice of signal region is introduced (Sec. 6.4). At last the systematic uncertainties (Sec. 6.5) and the limit setting procedure (Sec. 6.6) are explained.

6.1 KINEMATIC SELECTION

Most of the background contributions can be reduced by exploiting the balanced back-to-back decay kinematics of the $W' \to \mu\nu$ decay which is also valid for the Dark Matter signal. All events are required to fulfill the muon selection as defined in Sec. 4.1.3 before there kinematic properties are studied.

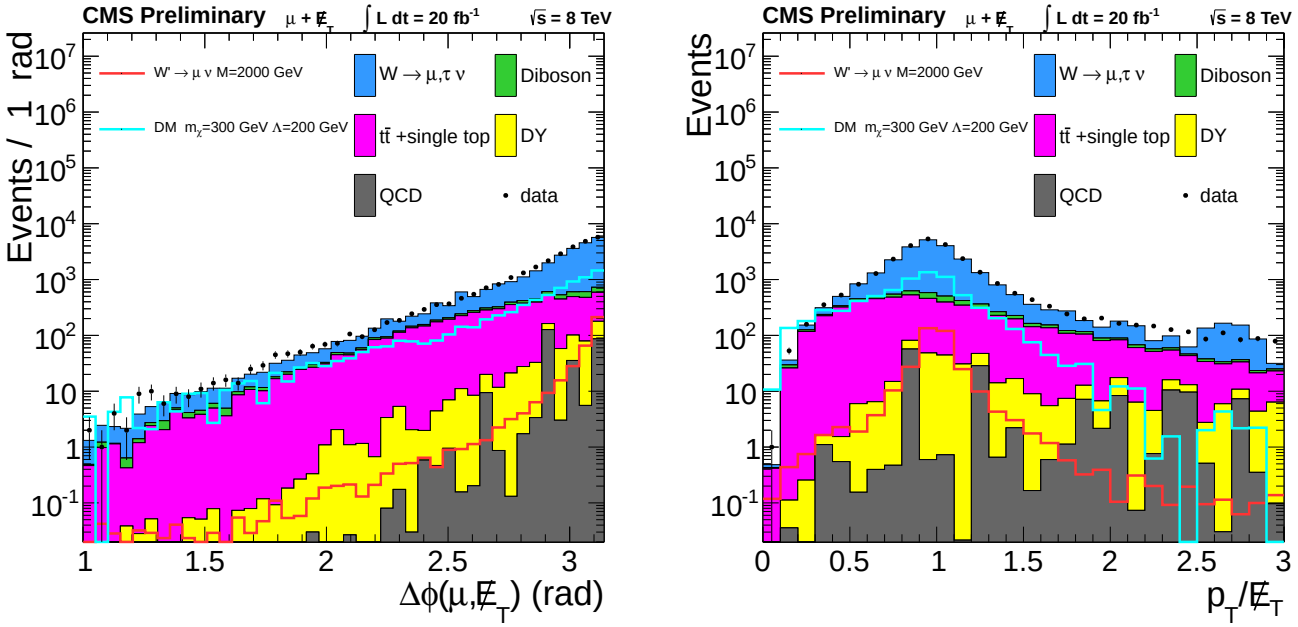

(a) Distribution of the ϕ-difference $\Delta\phi(\mu, \not{E}_T)$ between the muon and $\not{E}_T$. The background and also both example signal distributions show the expected peak at π. For the background it is mainly due to W and Diboson production.

(b) Distribution of the ratio of the muon p_T and $\not{E}_T$. The distribution shows a clear peak at one, as expected for the W and Diboson backgrounds and both example signals. The other background samples do not have a strong peak at one and can therefore be suppressed with a cut on this distribution. The cut values are $0.4 < p_T/\not{E}_T < 1.5$.

Figure 6.1: Kinematic distributions, $\Delta\phi$ (left) and $p_T/\not{E}_T$ (right).

The two kinematic distributions which describe the balanced back-to-back kinematic relation, are first the ratio of the muon momentum p_T over the missing transverse energy $\not{E}_T$ which should be one for a balanced back-to-back decay. The second distribution is the angular difference $\Delta\phi$ in the $r-\phi$ plane between the muon and $\not{E}_T$ which should be π for a

back-to-back decay. This ideal values are smeared out by detector resolution and initial and final state radiation. Both distributions are shown in Fig. 6.1.

To reduce the background contribution, while keeping most of the signal, two kinematic selections are applied. The ratio of the muon momentum p_T and $\not{E}_T$ peaks around one and events in the range $0.4 < p_T/\not{E}_T < 1.5$ are selected. In the transverse plane, the angle $\Delta\phi(\mu, \not{E}_T)$ between the muon and $\not{E}_T$ is nearly π and events with $\Delta\phi(\mu, \not{E}_T) > 0.8 \cdot \pi = 2.5$ are selected.

6.1.1 *Cross check of kinematic selection*

The kinematic distributions of $p_T/\not{E}_T$ and $\Delta\phi(\mu, \not{E}_T)$ (see Fig. 6.1) are different for the Dark Matter signal on the one side and for W' on the other side due to additional initial state jet radiation for the Dark Matter samples, so there might be the possibility to gain some additional sensitivity by optimizing these kinematic selections for the Dark Matter interpretation. Also for W' it can be helpful to have a look at the selection if there is potential for optimization because the selection was taken from previous Monte Carlo studies [114].

For this cross check, the background Monte Carlo samples were scaled to the luminosity of the dataset while the signal samples were scaled to the cross section that can be excluded with the used selection. As a measure for the sensitivity, the ratio $S/\sqrt{S+B}$ with the number of signal events passing the selection (S) and the number of background events passing the selection (B) are calculated. This is done for all possible selections of the three selection values to be optimized:

- The lower selection on $p_T/\not{E}_T$,
- The upper selection on $p_T/\not{E}_T$ and
- The selection on $\Delta\phi(\mu, \not{E}_T)$.

This method takes only the statistical uncertainty of the Monte Carlos into account, and not the systematic uncertainties, but for this simple crosscheck the $S/\sqrt{S+B}$ measure is sufficient.

The distribution of $S/\sqrt{S+B}$ for $M_T > 300\,\text{GeV}$ against all combination pairs of this three selections are shown in Fig. 6.2. To indicate the selection values with the highest sensitivity, as calculated from the three dimensional distribution, this point is marked with a blue marker in each plot. For comparison the used selections are shown with a black marker. What can be seen is that there is always a wide region where the sensitivity is nearly constant (green area) and changing the selection values would not gain much sensitivity. The point for the used selection is also always not very far off the optimized point in terms of sensitivity. For a dark matter signal, a loser selection and for W' a tighter selection is preferred.

To study this difference in sensitivity further, the ratio $S/\sqrt{S+B}$ is calculated for the optimized selection and for the used selection, depending on an additional cut on M_T, and are shown in Fig. 6.3. The uncertainty and value of these points are calculated by applying this procedure on the different generated mass points and calculating the mean and standard deviation from this different results to get a measure for the spread of the values. For Dark Matter, there is only a possible gain in sensitivity for a very low M_T-threshhold, but even this improved sensitivity would be lower than the sensitivity for a M_T-threshold of 300 GeV where the highest sensitivity is.

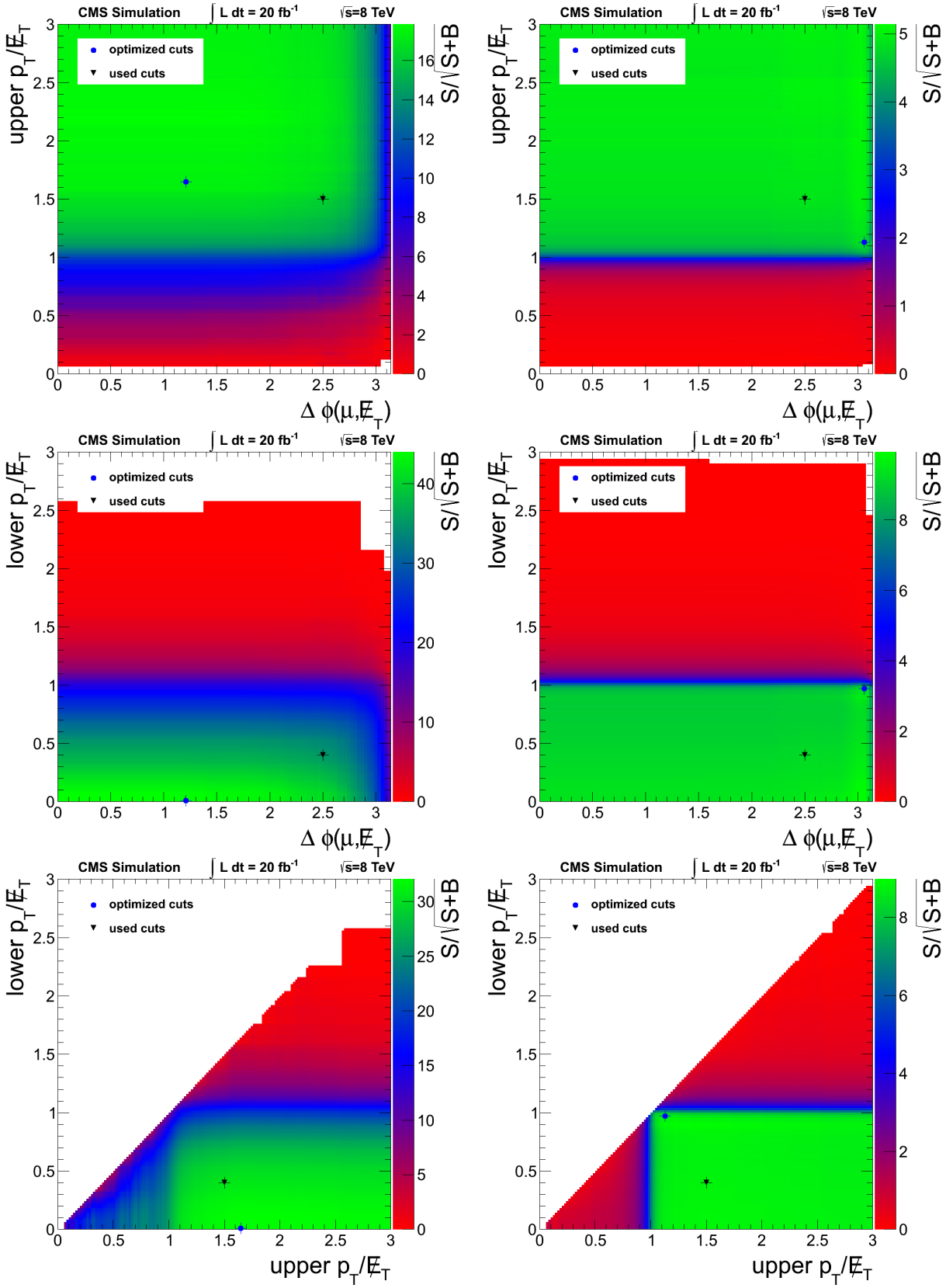

Figure 6.2: Sensitivity $S/\sqrt{S+B}$ distributions for different selection values and $M_T > 300\,\text{GeV}$: In the left column the distributions are shown for a Dark Matter signal and in the right column for the W' signal. In the top row the significance for the upper selection on $p_T/\not{E}_T$ against the selection on $\Delta\phi(\mu, \not{E}_T)$, in the middle row the lower selection on $p_T/\not{E}_T$ against the selection on $\Delta\phi(\mu, \not{E}_T)$ and in the bottom row the lower against the upper selection on $p_T/\not{E}_T$ are shown. In all distributions the selection values with the highest significance are indicated by a blue marker, the selection values used in the analysis are indicated by a black marker.

For W' there is even less gain in sensitivity by optimizing the cuts. This leads to the conclusion that the used cuts can be kept as they are and an optimization would not improve the result significantly.

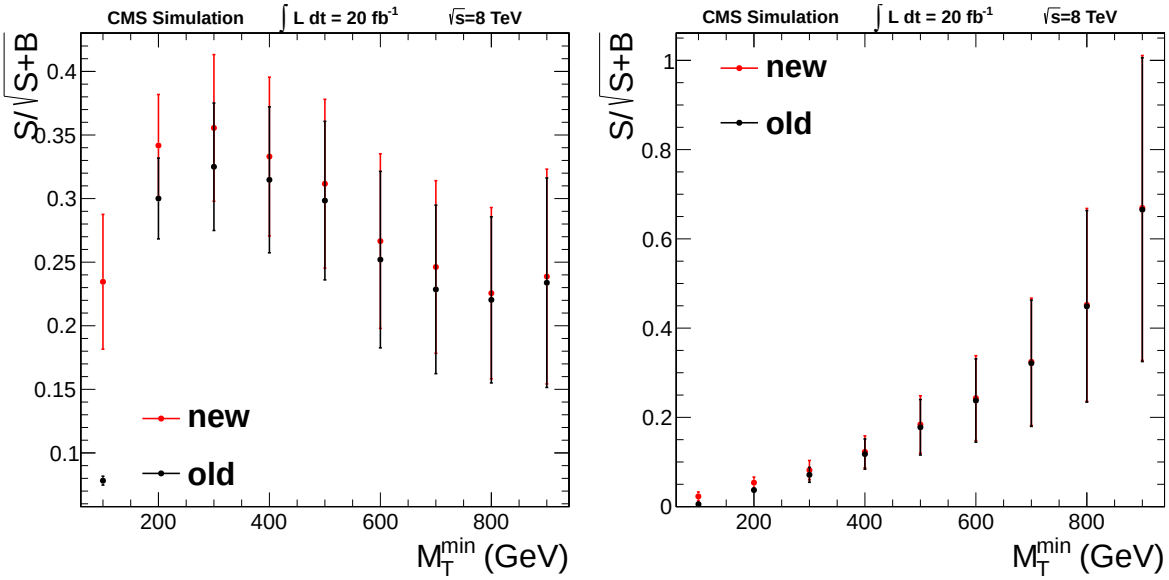

Figure 6.3: Sensitivity $S/\sqrt{S+B}$ distributions for the optimized and used selection values against an additional selection on M_T: The left distribution shows the results for a Dark Matter signal, the right one for a W' signal. The only region where one can gain some sensitivity above the spread of it is the low M_T-region for the dark matter sample, but even the improved sensitivity is smaller than the highest one achieved with the used selection. The points and there uncertainties were calculated by taking the mean and standard deviation of the $S/\sqrt{S+B}$ values for the different generated mass points.

6.2 PILE-UP REWEIGHTING

With the increase in instantaneous luminosity to very high values during the 2012 data taking (peak value: $7.67 \times 10^{33}\,cm^{-2}s^{-1}$), the number of additional interactions per bunch crossing has also increased up to ~ 50 (mean number of interactions is about 16). As the MC samples are generated beforehand with a different distribution of the number of pile-up interactions per event than observed in data, this has to be corrected.

The basic principle of the correction method is, to take the distribution of the number of interactions in data and the one used to produce the Monte Carlo sample and calculate the ratio. This ratio distribution can then be used to correct the Monte Carlo distribution for each event, resulting in a similar distribution in Monte Carlo and data. This method gives each event a weight, depending on the number of simulated interactions in the event, the so called pile-up weight.

The difficulty of this method is to know the distribution in data. There are two possibilities to get the data distribution. The first method is to just take the number of reconstructed vertices, corrected for the vertex reconstruction efficiency ($\sim 70\,\%$) and get the number of interactions. The second method is to use the measured instantaneous luminosity. Multiplying the instantaneous luminosity with the total inelastic cross section, gives the number of interactions per event.

The second luminosity-based method is used for this analysis due to its smaller uncertainties. For this method it is important to know the total inelastic cross section. The value taken for this analysis is 69.4 mb. The systematic uncertainties which come from this method are explained in Sec. 6.5 (documentation on the whole method can be found in Ref. [115]).

The final distribution of the number of reconstructed vertices after the reweighting is shown in Fig. 6.4, it shows a good agreement between data and Monte Carlo, showing that the pile-up reweighting method works.

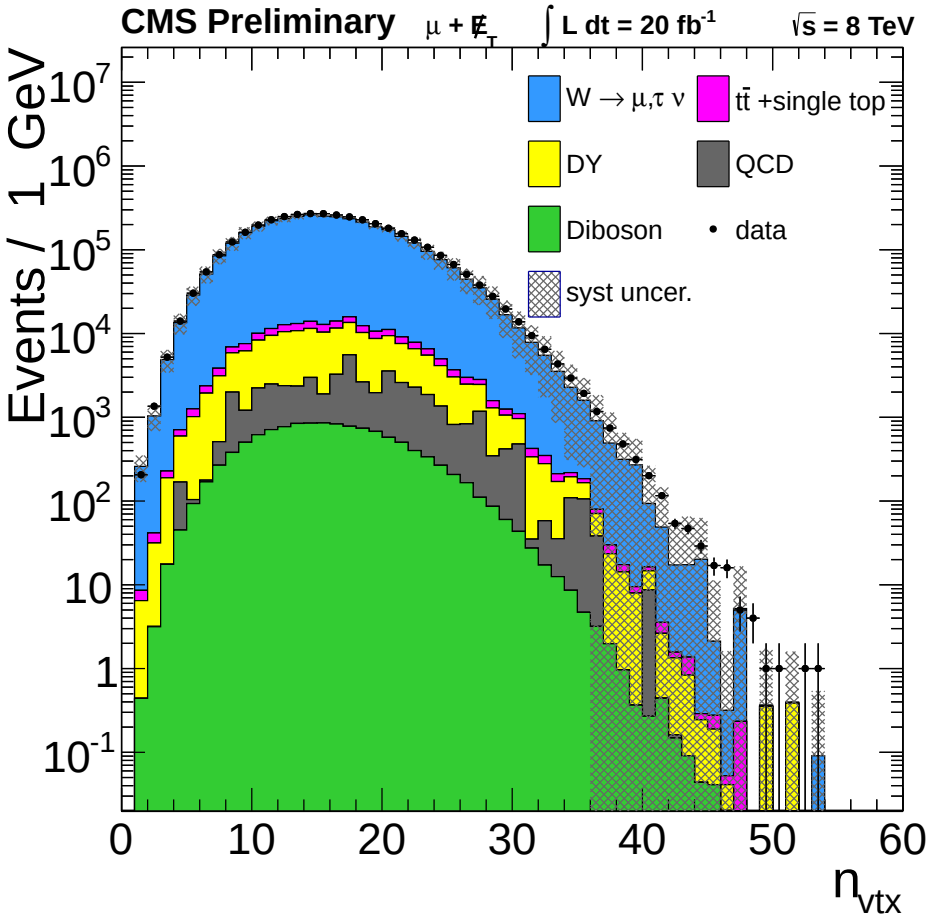

Figure 6.4: Distribution of the number of reconstructed vertices, after the pile-up reweighting: The agreement between data and Monte Carlo is good. The systematic uncertainties on the pile-up reweighting (Sec. 6.5) are shown as a gray shaded area and cover the disagreement between data and Monte Carlo.

6.3 EFFICIENCIES & SCALE FACTORS

Selection efficiencies are important to know for data and Monte Carlo samples, to correct for effects which are not simulated in the Monte Carlo samples. Therefore, the efficiency is factorized in 3 steps: $\epsilon_\mu = \epsilon_{ID} \cdot \epsilon_{ISO} \cdot \epsilon_{Trigger}$ with the trigger efficiency $\epsilon_{Trigger}$, the isolation efficiency ϵ_{ISO} and the muon ID efficiency ϵ_{ID}.

The ID, Isolation and trigger efficiencies used in this analysis are provided by the muon Physics Object Group (POG) [116]. They are calculated with the tag-and-probe method. This method measures efficiencies in data and Monte Carlo independently. The method uses the

Standard Model Z resonance decay in two muons which can clearly be identified. One muon passes a tight selection (tag), while the other passes a loose selection (probe). The probe is checked if it passes the studied analysis steps, while the tag is always required to pass. The efficiency of the analysis step is then the ratio of passing probes over all probes (passing + failing). This is done for the trigger requirement, the isolation requirement and the high-p_T muon ID, in three η bins ($|\eta| < 0.9$, $0.9 < |\eta| < 1.2$ and $1.2 < |\eta| < 2.1$). It is also binned in different muon p_T bins, but because there are not enough events at high p_T, the efficiency against p_T is parametrised with a constant and therefore extrapolated flat to high p_T[1].

These different efficiencies for data and Monte Carlo are listed in Tab. 6.1 and can be used to calculate a data/Monte Carlo scale factor. The different scale factors are also listed in Tab. 6.1. For the calculation of the trigger efficiency the isolation and muon ID criteria are already required and for the calculation of the isolation efficiency the muon ID is required..

Efficiency	Data (%)	Simulation (%)	Data/MC
$\|\eta\| < 0.9$			
High pT muon ID	95.54 ± 0.02	96.51 ± 0.02	0.9900 ± 0.0003
Rel. tracker isolation	99.46 ± 0.01	99.49 ± 0.01	0.9996 ± 0.0001
Trigger Mu40eta2p1	92.90 ± 0.02	95.10 ± 0.03	0.9768 ± 0.0004
$0.9 < \|\eta\| < 1.2$			
High pT muon ID	95.87 ± 0.04	96.61 ± 0.04	0.9923 ± 0.0006
Rel. tracker isolation	99.51 ± 0.01	99.58 ± 0.01	0.9994 ± 0.0001
Trigger Mu40eta2p1	83.14 ± 0.06	87.01 ± 0.03	0.9555 ± 0.0011
$1.2 < \|\eta\| < 2.1$			
High pT muon ID	95.06 ± 0.03	95.54 ± 0.03	0.9949 ± 0.0004
Rel. tracker isolation	99.56 ± 0.01	99.59 ± 0.01	0.9997 ± 0.0001
Trigger Mu40eta2p1	80.27 ± 0.05	81.56 ± 0.03	0.9842 ± 0.0009

Table 6.1: Trigger, isolation and ID efficiency in data and Monte Carlo simulation for three η bins: Also listed are the different data/Monte Carlo scale factors for trigger, isolation and ID in three η bins. All given uncertainties are purely statistical.

The final scale factors that are used in the analysis are binned in η, and have the values listed in Tab. 6.2. Each Monte Carlo event is weighted depending on the η of the muon in the event. The given uncertainties are statistical and are $\lesssim 0.1\,\%$ and can therefore be neglected compared to the systematic uncertainties ($\gtrsim 1\,\%$). The systematic uncertainties on the efficiencies and scale factors are explained in Sec. 6.5.

6.4 SIGNAL SELECTION

The final distribution is the transverse mass spectrum calculated from the muon and $\not{E}_T$, which is the main discriminating distribution. The analysis searches for an excess in the transverse mass spectrum by comparing the data distribution to the Standard Model expectation. As both signal models, Dark Matter and W', would show an excess at high M_T, the whole transverse mass spectrum above the threshold $M_T > 220\,\text{GeV}$ is used for the analy-

1 This extrapolation is conservative for the trigger and isolation efficiency and reasonable for the ID efficiency.

sis[2]. Every event that ends up in the final M_T distribution, has to pass the trigger selection (Sec. 4.1.1), the muon ID selection (Sec. 4.1.3) and the kinematic selection (Sec. 6.1). They are also corrected for $\not{E}_T$ effects (Sec. 4.2.3) and Monte Carlo events are corrected for pile-up (Sec. 6.2) and efficiencies (Sec. 6.3). The resulting M_T distribution is shown in Fig. 6.5.

$\lvert\eta\rvert < 0.9$	$0.9 < \lvert\eta\rvert < 1.2$	$1.2 < \lvert\eta\rvert < 2.1$
0.997	0.958	0.979

Table 6.2: Final data/Monte Carlo scale factors used in the analysis in three η bins.

The binning of the distribution is driven by the muon p_T resolution, which directly corresponds to the M_T resolution, because the $\not{E}_T$ and its resolution is dominated by the high energy muon. The binning is therefore chosen to have a bin width about 10 % of the M_T value.

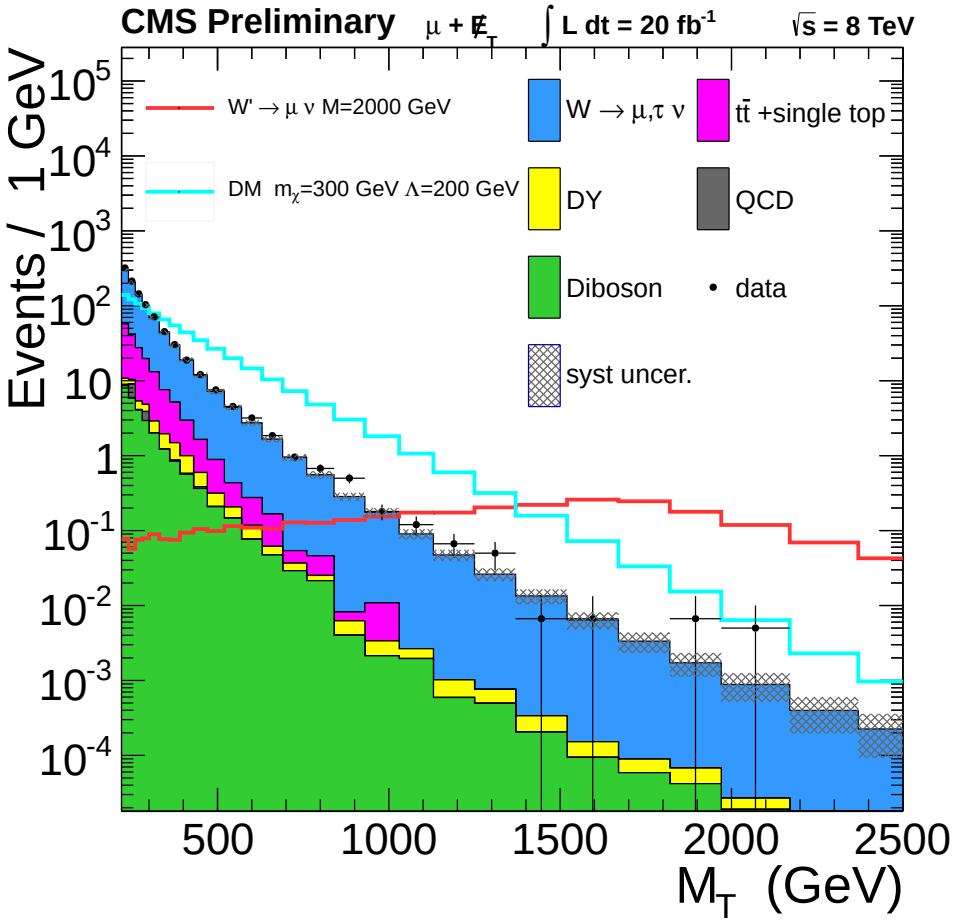

Figure 6.5: Final transverse mass distribution, calculated from all muons and $\not{E}_T$ that pass all selection steps: The Standard Model background is shown as a stacked histogram, the data as black markers and two signal examples as colored lines. The systematic uncertainty on the background is shown as a grey shaded band (details on the systematic uncertainties are given in Sec. 6.5).

The agreement between data and Monte Carlo is quite good. All deviations are smaller than one standard deviation σ of systematic uncertainty with one exception, one data point

2 The region with $M_T > 220\,\text{GeV}$ is chosen to be consistent with the electron channel, where the lower bound is given by the offline E_T selection of $E_T > 100\,\text{GeV}$.

at $M_T = 900\,\text{GeV}$ deviates more than one σ. Control plots for all events ($\not{E}_T$ of the events and p_T, ϕ and η for the muons) are shown in Sec. A.9, and confirm the good data/Monte Carlo agreement. Also control plots for the deviating region $840 < M_T < 920\,\text{GeV}$ are shown in Sec. A.9 and show no systematic of the deviation, indicating a statistical fluctuation. The observed event with the highest transverse mass $M_T = 2.1\,\text{TeV}$ is shown as an event display in Sec. A.1, and is dominated by the muon and $\not{E}_T$, and fulfills clearly the signal selection.

For a better comparison between data and Monte Carlo on this steeply falling spectrum the ratio of data measurement minus Monte Carlo prediction over Monte Carlo prediction, is calculated and shown in Fig. 6.6. Also in this plot the biggest data-Monte Carlo disagreement can be seen at $M_T \sim 900\,\text{GeV}$, but it is smaller than $2\,\sigma$, and therefore not a significant deviation. The good overall agreement between data and Monte Carlo, can be seen even better in the ratio. For the calculation of the ratio, bins were merged until each bin contained at least 20 Monte Carlo events, so that the calculation of the ratio is reasonable and not driven by single events.

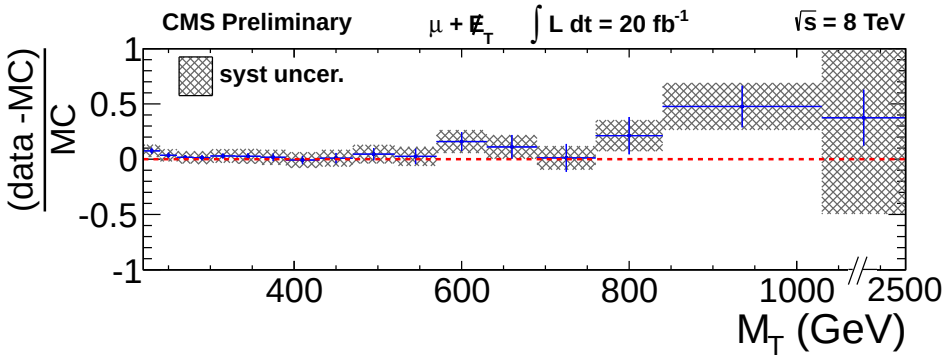

Figure 6.6: Ratio plot, showing the ratio of data minus Monte Carlo over Monte Carlo events: The binning is chosen in a way, that each bin contains at least 20 Monte Carlo events, and for the last bin the x-axis is broken. The biggest deviation is in the $M_T \sim 900\,\text{GeV}$ bin, as expected from the M_T plot.

Another way of comparing data and Monte Carlo especially at high M_T, with few data events, is to use the cumulative plot, which shows the integrated number of events above a M_T threshold, as a function of the M_T threshold. It is shown in Fig. 6.7. The good data/Monte Carlo agreement can clearly be seen, the only deviation ($> 1\,\sigma$) is at $M_T \sim 900\,\text{GeV}$ and therefore consistent with the standard M_T plot, while there are no additional deviations.

For the final selection, a high signal efficiency is important, to get a high signal over background ratio. The efficiencies for the background are listed in Tab. 5.2. For the signal the efficiencies are calculated in different selection steps.

For the W' signal they are shown in Fig. 6.8, depending on the W' mass. The efficiency is maximal for $1\,\text{TeV} < M_{W'} < 2\,\text{TeV}$ at about 70 %. For lower W' masses the efficiency decreases because the muon and $\not{E}_T$ from the W' decay do not have such high momenta and are not so concentrated in the central region, resulting in a loss of efficiency due to the p_T and η-acceptance selection. For higher W' masses the efficiency decreases due to higher off-shell production of the W', which has the same effect as light W's.

For the Dark Matter signal, the efficiency does not depend on the Dark Matter mass and type of coupling, as the shape of the signal does not depend on the mass and coupling (Sec. 5.3.3). It does depend on the parameter ξ and therefore on the steepness of the signal. For $\xi = +1$ the final signal efficiency is $13 \pm 2\,\%$.

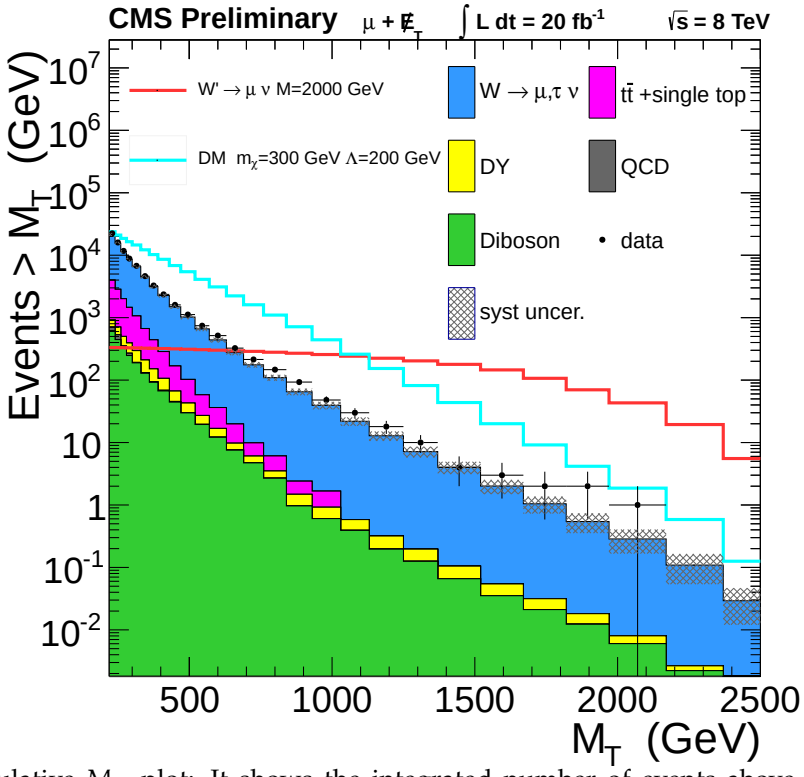

Figure 6.7: Cumulative M_T plot: It shows the integrated number of events above a M_T threshold, depending on the M_T threshold. The agreement for low M_T and very high M_T between data and Monte Carlo is good, the disagreement at $M_T \sim 900\,\text{GeV}$ is the biggest deviation.

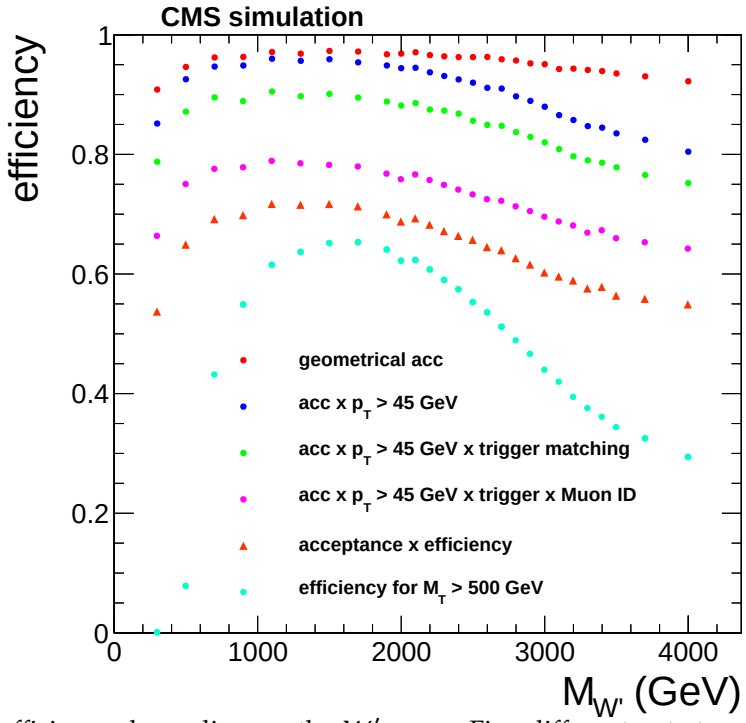

Figure 6.8: Signal efficiency depending on the W' mass: Five different cut stages are shown and an additional cut on $M_T > 500\,\text{GeV}$. The complete selection efficiency is denoted 'acceptance x efficiency'. At low $M_{W'}$ the efficiency is reduced mainly by the η and p_T cuts, due to low energy muons in the forward region. At high $M_{W'}$ the efficiency is reduced due to increased off-shell production of the W'.

For the other interference cases $\xi = 0, -1$, the spectrum extends to higher M_T and therefore the efficiency is also higher with $39 \pm 4\,\%$ ($\xi = 0$) and $42 \pm 4\,\%$ ($\xi = -1$). The given errors are the spread of the efficiency values for different Dark Matter masses.

6.5 SYSTEMATIC UNCERTAINTIES

In this section the different sources for systematic uncertainties are explained, and the effect on the final distribution is discussed. All systematic uncertainties are applied to the background simulation and the different signal simulations. For the calculation of the systematic uncertainties the analysis was redone with objects shifted or events reweighed according to their uncertainty. All systematically shifted distributions for the background (Sec. 5.2.2) and Dark Matter signals are parametrised (Sec. 5.3.4) and the difference to the final M_T distribution is taken as the systematic uncertainty. The uncertainties that contribute in this analysis are listed in the following section in increasing order of importance at high M_T.

6.5.1 *Luminosity:*

The luminosity is measured by the rate R of specific events (like Z bosons decaying to two muons)

$$\mathcal{L} = \frac{R}{\sigma_{vis}} = \frac{R}{\sigma_0\,(E)\,A\,(t, \mu, n_b, \cdots)} \tag{6.1}$$

with the visible cross section σ_{vis} of the process, which consists of the cross section σ_0 and the acceptance A, which depends on time t, pileup μ, filling scheme n_b and other parameters. A detailed study of this procedure and its systematic uncertainties is given in Ref. [117], which results in an overall systematic uncertainty of 2.5 % on the luminosity. As the background is scaled to the luminosity, the scaling factor is varied $\pm 2.5\,\%$ and the difference of this distributions to the final M_T distribution is taken as the systematic uncertainty due to the luminosity.

6.5.2 *Scale factors:*

For the final scale factors (Sec. 6.3), two uncertainties are taken into account. First the uncertainty due to the tag-and-probe method with Z events, which is used to determine the scale factors. The second uncertainty is due to the extrapolation, from Z decay energies to the highest energies in the M_T spectrum.

The muon Physics Object Group determined a systematic uncertainty of 0.5 % (ID), 0.2 % (isolation) and 0.2 % (trigger) on the scale factor [118]. Therefore, a systematic uncertainty of 1 % is assumed for the tag-and-probe method on the scale factor.

For the extrapolation of the scale factors from the region it is measured ($p_T \sim 100\,\text{GeV}$) to the search region ($p_T \sim 1000\,\text{GeV}$), it is assumed that the scale factor is flat versus p_T. The scale factor can be extrapolated from different points, this choice leads to an uncertainty due to the extrapolation. For the different scale factors, the dependence of the scale factors as a function of p_T are shown in Fig. 6.9.

	$\lvert\eta\rvert < 0.9$	$0.9 < \lvert\eta\rvert < 1.2$	$1.2 < \lvert\eta\rvert < 2.1$	
ID	0.9900 ± 0.0247	0.9923 ± 0.0163	0.9949 ± 0.0368	
ISO	0.9996 ± 0.0020	0.9994 ± 0.0016	0.9997 ± 0.0007	
Trigger	0.9768 ± 0.0132	0.9555 ± 0.0082	0.9842 ± 0.0021	combined
SF	0.9967 ± 0.0276	0.9476 ± 0.0176	0.9789 ± 0.0363	0.9688 ± 0.0194

Table 6.3: Scale factors for the different η regions (columns) and the three selection criteria (rows): The combined scale factor (SF) for the three η regions is given in the last row and is used in the analysis. For comparison, a combined scale factor is calculated by averaging the three scale factors, weighted with the number of events in each η region. The given error is the uncertainty due to the extrapolation uncertainty of the scale factor to high p_T. The additional uncertainty of 1 % due to the tag-and-probe method is not included.

Also shown are the lines which correspond to the highest p_T bin (green), to the second highest p_T bin (red) and also the fit of a constant (blue) to all points, the maximal difference between this three lines is chosen as the systematic uncertainty due to the extrapolation on the scale factor. The scale factor is determined by the parametrisation of all these points with a constant (blue). The resulting different scale factors and the projection uncertainty are listed in Tab. 6.3. In this analysis, a scale factor depending on η is used.

The systematic uncertainty for the scale factor consists out of the systematic uncertainty of the tag-and-probe method (~ 1 %) and the extrapolation uncertainty (1.9 %).

6.5.3 *Missing transverse energy:*

$\not{E}_T$ is a composite object, calculated of all objects in the event (Sec. 4.2), therefore all objects contribute to the uncertainty on $\not{E}_T$. The uncertainty on $\not{E}_T$ is calculated by splitting $\not{E}_T$ in this different objects, varying each objects scale and resolution by its systematic uncertainty, and recalculating $\not{E}_T$. The objects of $\not{E}_T$ are:

- Electrons and Photons: For the measurement of the momentum scale the invariant mass of Z boson decaying to electron pairs is used. The resulting systematic uncertainty is ± 0.6 % in the barrel and ± 1.5 % in the end caps [119].
- Tau: The tau uncertainty is based on the energy scale uncertainty for hadronically decaying taus. The tau energy scale was measured with data in $Z \to \tau\tau \to \mu\tau_h$[3], where the muon can be measured with high precision. The reconstruction of the invariant mass can then be compared to a Monte Carlo prediction, resulting in a tau energy scale uncertainty of 3 % [120]. The basic object which is used for the $\not{E}_T$ calculation is a PF-jet and not the reconstructed tau, just the tau uncertainty is applied.
- Muon: The muon contributes in this analysis not only to the $\not{E}_T$, but is its own object in the analysis, therefore the uncertainties on $\not{E}_T$ due to the muon uncertainties are not treated in the context of $\not{E}_T$ and are discussed in the μ resolution and μ scale sections (Sec. 6.5.6 and Sec. 6.5.8). The effect on $\not{E}_T$ is comparable to the effect on the muon because $\not{E}_T$ is dominated by the muon for high M_T.

3 In this context τ_h means, that the tau decays into hadrons.

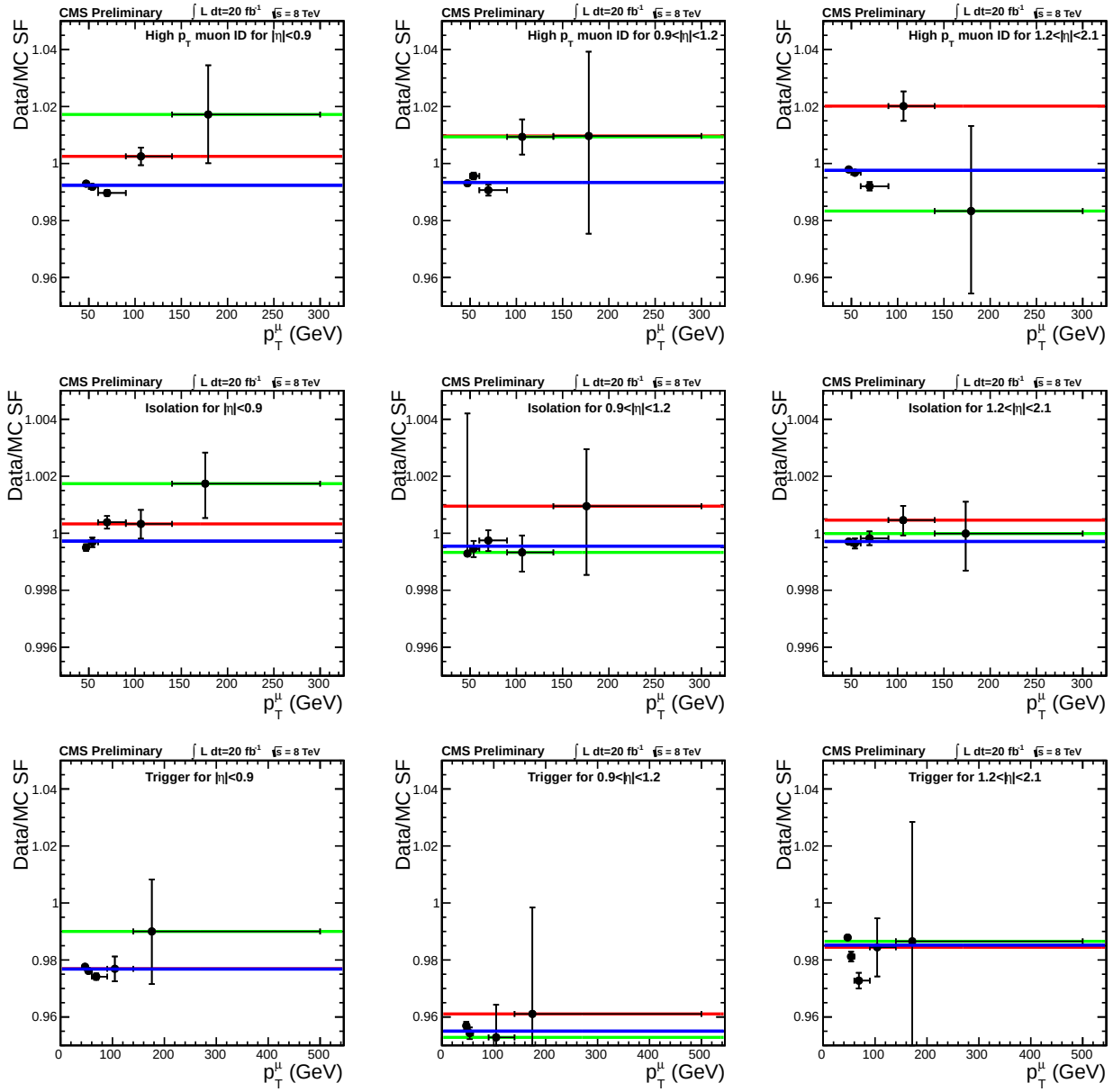

Figure 6.9: Scale factors for the different η regions (columns) and the three different selections (rows), depending on the p_T of the muon: The highest p_T bin (red), the second highest p_T bin (green)and the parametrisation of the distribution with a constant (blue) are marked with colored lines. The difference between these lines is taken as the systematic uncertainty on the extrapolation of the scale factor to high p_T. The mean value, used for the analysis was determined by the parametrisation. The shown errors are statistical, and the range of the y-axis is limited to a small interval around one.

- Unclustered energy: The unclustered energy (jets with $p_T < 10\,\text{GeV}$ and particle candidates not within a jet) is varied by $\pm 10\,\%$ [121].

- Jet energy resolution: The jet energy resolution (JER) in data is worse than in Monte Carlo as seen in measurements. To correct for this difference, Monte Carlo events can be corrected

$$p_T \to \max\left[0, p_T^{gen} + c \cdot \left(p_T - p_T^{gen}\right)\right] \tag{6.2}$$

with the correction factor c and the truth p_T^{gen}. This method works only for jets that can be matched to a jet on generator level. For all other jets, the reconstructed p_T can be smeared with a gaussian with the width

$$\sqrt{c^2 - 1} \cdot \sigma_{MC} \tag{6.3}$$

with the jet resolution in Monte Carlo events σ_{MC}. The correction factor c can be varied by $\pm 1\sigma$, resulting in a corresponding uncertainty on the JER. This correction factor was determined with 2011 data and is η dependent with the values listed in Tab. 6.4. The values are still valid for the 2012 data taking period. The whole JER correction is based on Ref. [122].

$\lvert\eta\rvert$ region	$0.0 - 0.5$	$0.5 - 1.1$	$1.1 - 1.7$	$1.7 - 2.3$	$2.3 - 5.0$
$c_{-1\sigma}$	0.990	1.001	1.032	1.042	1.089
$c_{+1\sigma}$	1.115	1.114	1.161	1.228	1.488

Table 6.4: Jet energy resolution correction factors.

- Jet energy scale: The jet energy scale can be measured in events where jets are balanced against photons or Z bosons, which can be measured more accurate than jets. The uncertainties of this method due to background events, initial and final state radiation and pile-up and extrapolation to higher jet energies result in the jet energy scale uncertainty. This uncertainty is shown in Fig. 6.10 for the $\eta = 0.0$ region, depending on the p_T of the jet as an example.

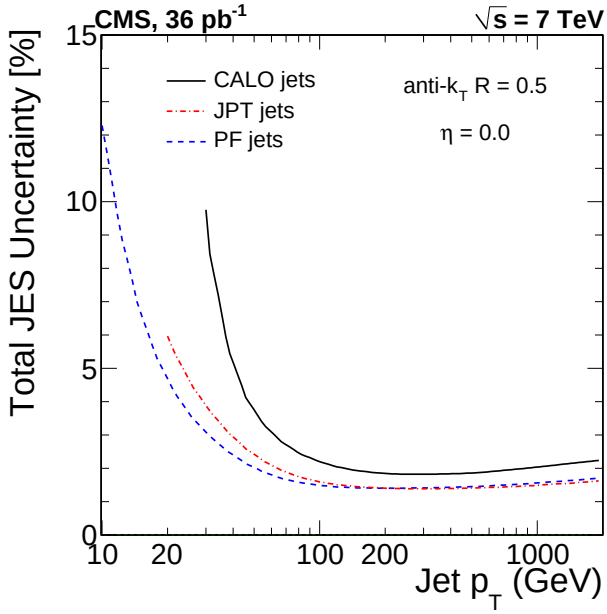

Figure 6.10: Jet energy scale uncertainty as a function of the jet p_T for anti-k_T jets at $\eta = 0.0$ with $R = 0.5$: Shown are the relative uncertainties for calorimeter jets (CALO), Jet-Plus-track jets (JPT, which are CALO jets with additional tracker information) jets and particle-flow (PF) jets [123]. These results from 2010 were confirmed with newer (2011 and 2012) measurements. For the calculation of $\not{E}_T$, the particle-flow jets are used.

The systematic uncertainties due to $\not{E}_T$ are 0.5 % (electrons), 0.5 % (taus), 1.7 % (unclustered energy), 2.3 % (jet energy resolution) and 0.6 % (jet energy scale) on the integrated number of events with $M_T > 220\,\text{GeV}$.

6.5.4 *Parton distribution functions:*

The determination of the systematic uncertainties due to the PDFs depends on the method of the PDF determination (This description is based on Ref. [124]). There are two different possibilities which are used to determine PDF sets, the Hessian approach (MSTW, Cteq) and the Monte Carlo approach (NNPDF).

For the Hessian approach the central value is determined by minimizing a suitable log-likelihood χ^2-function, while the uncertainties are determined by diagonalizing the Hessian matrix of second derivatives of the χ^2 minimum and then determining the range of each orthogonal Hessian eigenvector which corresponds to a predicted increase of the χ^2 function with respect to the minimum. For each of these cases (mean, variation up and down for each eigenvector) a PDF set is given. These different PDF sets are then used to get a combined uncertainty on the variable x

$$\Delta x^+_{max} = \sqrt{\sum_{i=1}^{N} \left[\max\left(x_i^+ - x_0, x_i^i - x_o, 0\right)\right]^2} \tag{6.4}$$

$$\Delta x^-_{max} = \sqrt{\sum_{i=1}^{N} \left[\max\left(x_0 - x_i^+, x_o - x_i^-, 0\right)\right]^2} \tag{6.5}$$

with the mean value x_o and the value $x_i^\pm$ for the $\pm$ variation of the eigenvector i. These uncertainties were calculated with 68 % C.L. (confidence level). This takes the uncertainties of the PDF determination into account. To take the uncertainty on the strong coupling constant α_S into account, PDF sets with an up and down variation of α_S are provided. The difference to the mean x_0 results in Δx_{α_S}. Both uncertainties are combined to the PDF uncertainty

$$\Delta_x = \sqrt{\Delta x^2_{PDF} + \Delta^2_{\alpha_S}} \tag{6.6}$$

For the Monte Carlo approach, the PDF sets are determined by producing a Monte Carlo sample of N_{rep} pseudo-data replicas. From each data replica, a PDF replica is constructed by minimizing a χ^2 function.

PDF central values, uncertainties and correlations are then determined by taking the means, variances and covariances of these replica PDF sets. The standard deviation of x can than be calculated from the variance $V(x)$:

$$\sigma_x = V(x)^{\frac{1}{2}} = \left(\frac{N_{rep}}{N_{rep}-1}\left(\langle x^2\rangle - \langle x\rangle^2\right)\right)^{\frac{1}{2}} = \left(\frac{1}{N_{rep}-1}\sum_{k=1}^{N_{rep}}(x_k - x_0)^2\right)^{\frac{1}{2}} \tag{6.7}$$

with the expectation value $\langle x\rangle$ of x and the value of the k-th replica x_k.

To account for the α_S uncertainties in the Monte Carlo approach, different replica sets are provided for different values of α_S. To take these uncertainties into account, the expectation value of x is calculated via

$$\langle x \rangle = \frac{1}{N_{rep}} \sum_{j=1}^{N_\alpha} \sum_{k_j=1}^{N^j_{rep}} w^j_{\alpha_S} \cdot x \left(PDF^{(k_j,j)}, \alpha^j_S \right) \tag{6.8}$$

with the k_j's replica of the PDF obtained with the j's α^j_S value. The total number of PDF sets N_{rep} is summed over the number of replicas per α_S value N^j_{rep} which are weighted under the assumption that α_S is gaussianly distributed by

$$w^j_{\alpha_S} = 100 \cdot \exp\left(-\frac{\left(\alpha^j_S - \alpha^0_S\right)^2}{2\delta^2_{\alpha_S}} \right) \tag{6.9}$$

with α^0_S as the central $\alpha_S = 0.119$ (at the energy scale M_Z) value and $\delta_{\alpha_S} = 0.002$ the uncertainty of α_S.

The systematic uncertainties are calculated for the three PDF sets (CT10, MSTW and NNPDF). The deviation of these NLO error PDFs to the LO PDF (cteq6l1) which was used to generate most background samples is shown in Fig. 6.11 in green (CT10), blue (MSTW) and cyan (NNPDF). The difference between the central values of CT10 and cteq6l1 is corrected for the *W* background by the *W* k-factor (shown in red in Fig. 5.2-left).

To not account only the systematic uncertainties of one PDF set but also the uncertainty due to a choice of one PDF set, the envelope of all three PDF sets (shown in red in Fig. 6.11) is calculated and the relative deviation of the envelope from the envelope mean is used as the systematic uncertainty due to the PDF sets.

6.5.5 *Pile-up reweighting:*

The uncertainty on the pile-up reweighting comes from the uncertainty of the data distribution of the number of interactions. This distribution is calculated from the instantaneous luminosity and the total inelastic cross section, which results in two sources of uncertainty. The uncertainty on the luminosity is 2.5 % (see luminosity uncertainty), while the total inelastic cross section is optimized for a good data/Monte Carlo agreement for $Z \to \mu\mu$ events resulting in a combined uncertainty of 3.9 % on the number of interactions. To get an uncertainty for the analysis, the data pile-up distribution is calculated first with the best fit value for the total inelastic cross section of 69.4 mb and once with 73 mb [125].

6.5.6 μ *resolution:*

The muon resolution was measured with cosmic muons (Fig. 4.1). The measured values agree with the simulation in Monte Carlo[126]. The value of the resolution is 8.3 % with a uncertainty of 0.6 % for a muon with $p_T > 350$ GeV. To smear the Monte Carlo to a resolution of 8.3 % + 0.6 % = 8.9 % an additional p_T smearing of 3.2 % is necessary[4], therefore the muon p_T was randomly smeared, with a gaussian with a width of $0.032 \cdot p_T$.

4 Under the assumption that the resolutions are gaussian distributed.

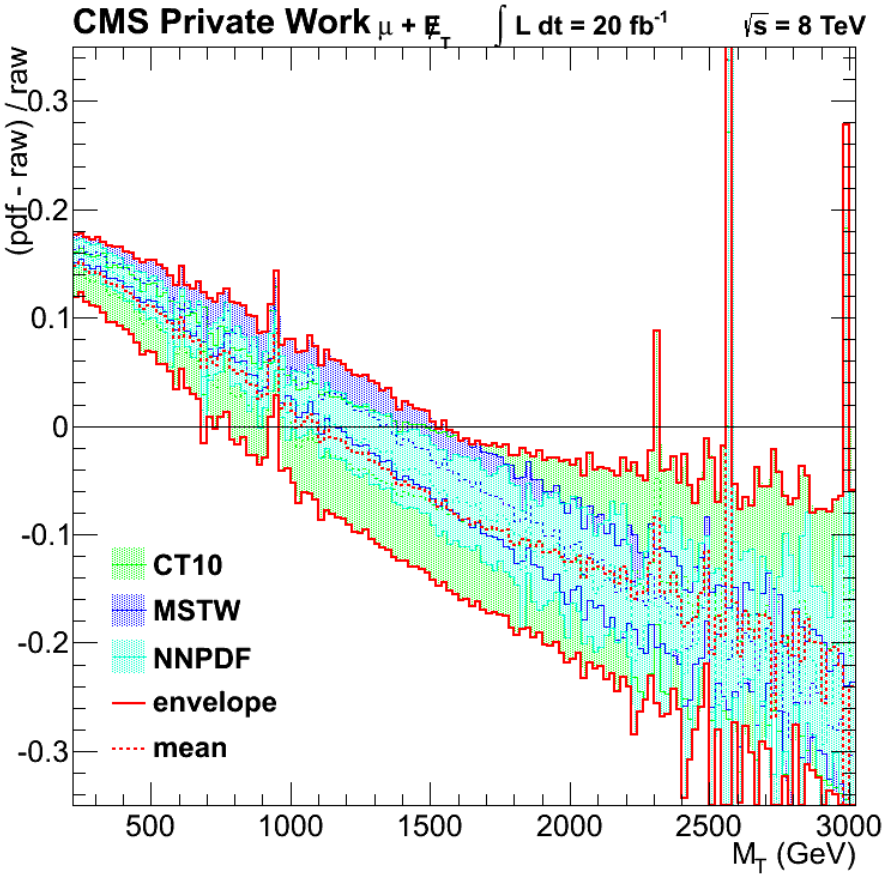

Figure 6.11: PDF uncertainties: The difference between the M_T distribution is shown as the ratio $(pdf - raw)/raw$ for the complete Monte Carlo background. This is calculated from PDF set (mostly LO cteq6l1) raw used to generate the sample and the three NLO PDF sets pdf, which used to evaluate the PDF uncertainties. The mean of each PDF set is shown as a dashed line, while the envelope of the 68 % C.L. uncertainties is shown as a solid line. The difference between the LO expectation and the CT10 mean is corrected for the main W background through the W k-factor. The overall uncertainty is taken as the envelope of all three PDF sets and shown in a red solid line, while the overall mean is shown as a red dashed line. The various statistical fluctuations are compensated by a parametrisation of the different distributions (Sec. 5.2.2).

6.5.7 *k-factor:*

For the calculation of a combined k-factor of electroweak and QCD corrections, two different approaches are possible, an additive or a multiplicative combination (Sec. 5.2.1). Both approaches are parametrised with a second order polynomial, to avoid fluctuations. The mean of the two parametrisation is used as the central value and the final k-factor. For the uncertainty half the difference between the two parametrisation is used as the systematic uncertainty on the k-factor. Effects due to higher order corrections are not considered in this analysis. They are expected to be $\sim 1.3\,\%$ (Electroweak corrections for $M_T > 1\,\text{TeV}$ and $\sqrt{s} = 14\,\text{TeV}$) [127] and $\sim \mathcal{O}(1\,\%)$ (QCD corrections) [110]. These corrections are smaller than the effect due to the different combination methods.

6.5.8 μ *scale:*

The muon momentum scale was measured with cosmic ray muons by the end-point method (details on the method can be found in Ref. [128]). In this measurement the curvature offset $\kappa = q/p_T$ was determined[5], which would affect positively charged muons different than negative muons. This offset would result in a shift of q/p_T

$$\frac{q}{p_T} \rightarrow \frac{q}{p_T} + \kappa \tag{6.10}$$

The negative muons would have a systematically lower (higher) momentum, while positive muons would have a systematically higher (lower) momentum for a negative (positive) κ. To measure κ, the fact that no muon should have zero curvature (or infinite momentum) is used, cosmic muons with zero curvature can therefore used to measure the curvature offset.

The effect by this offset can be seen in Fig. 6.12b, where a curvature bias of 50 % at 1 TeV was simulated in Monte Carlo events. Due to the curvature bias, the minimum of the distribution is not at zero, but shifted depending on κ. A measurement with cosmic data is shown in Fig. 6.12a. Interesting for this analysis is not the value of κ, but the uncertainty on the measurement, which results in the systematic uncertainty on the muon momentum scale. The latest measurement of κ is shown in Fig. 6.13, with the resulting $\kappa = (0.05 \pm 0.05)\ 1/TeV$. The final uncertainty of 5 %/TeV is then used to shift the muon p_T accordingly up and down.

With this shifted p_T, also $\not{E}_T$ is corrected (Sec. 4.2.3) and the whole analysis is redone and the maximal difference to the final M_T distribution is used as the systematic uncertainty due to the uncertainty of the muon momentum scale.

6.5.9 *Combined uncertainty*

The different sources of systematic uncertainties are then combined to an overall uncertainty. For this combination it is assumed that all systematic uncertainties are uncorrelated. For systematic effects which consists out of an up and down shift, the maximal deviation from the main M_T distribution is taken as the uncertainty for the combination. The $\not{E}_T$ uncertainties are combined by adding the different components in quadrature. The same happens with the scale factor systematic uncertainties from the tag-and-probe method and from the extrapolation of the scale factor. The relative difference to the final M_T distribution is shown for the background in Fig. 6.14 as colored lines as a function of M_T. For the combined uncertainty, all systematic uncertainties are added in quadrature and the result is shown in Fig. 6.14 as a black line. The luminosity uncertainty is not included in this plot, because it simply scales the background and does not depend on M_T and is not included in the combined uncertainty.

6.6 LIMIT SETTING

No significant deviation from the Standard Model expectation was found in the final M_T distribution (Fig. 6.5), and an exclusion limit is set on the two models for new physics, W' and Dark Matter. This limit setting is done with a Bayesian approach, which is explained in the following[6]. The idea is to quantify which part of the parameter space of the new physics

5 Such a curvature offset or bias can be induced by the alignment of the detector.

6 The practical implementation of this limit calculation is done in the Higgs combination tool [129] on top of RooStats [130].

model can be excluded by the observation of a good agreement between data and Monte Carlo simulation. This summary is based on Ref. [131].

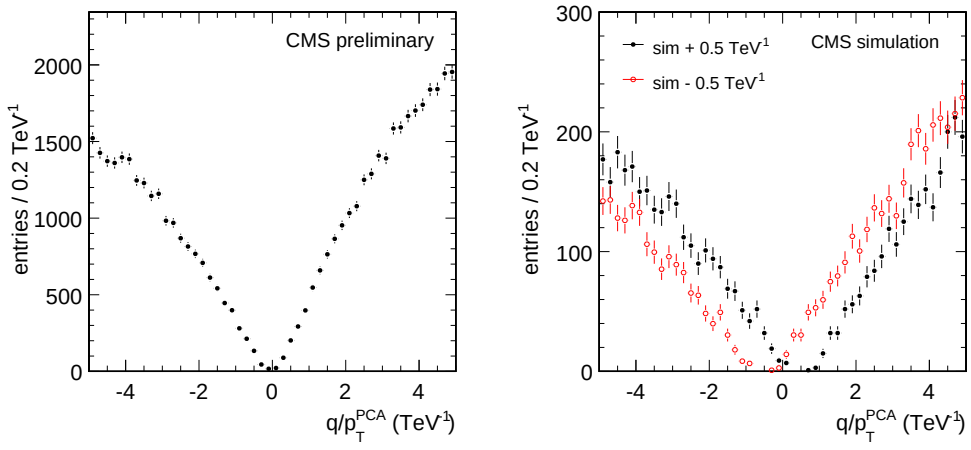

(a) The q/p_T spectrum observed in data in 2010: This distribution shows the expected asymmetry between positive and negatively charged muons from cosmic rays. The curvature offset from zero is small and can not be seen by eye.

(b) Curvature bias in Monte Carlo events: In this simulation a bias of $\pm 50\,\%$ at 1 TeV is introduced in the simulation. The offset of the minimum of the distribution from zero is clearly visible.

Figure 6.12: Cosmic ray muons end-point method: Shown is the q/p_T distribution for data (left) and two Monte Carlo examples (right). p_T^{PCA} is the muon momentum calculated at the point of closest approach to the nominal collision point [128].

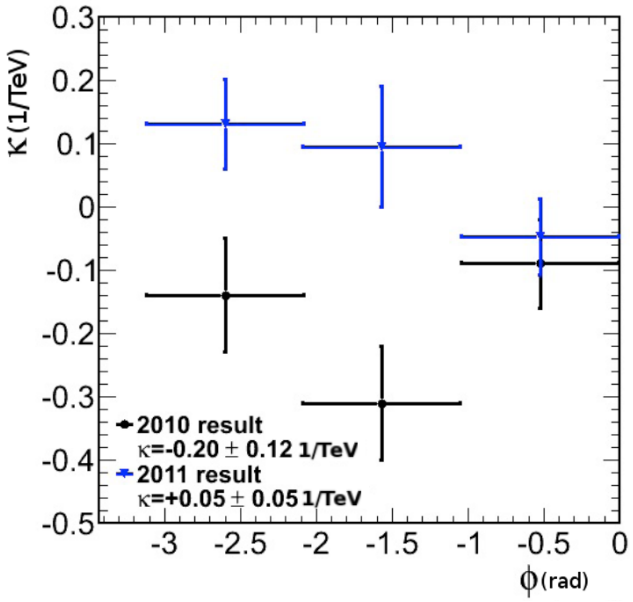

Figure 6.13: Curvature bias result: The curvature bias κ is shown for two different data taking periods (2010 in black and 2011 in blue) depending on ϕ. Both results were obtained with cosmic muon data and the improvement in 2011 is due to improved alignment. To get a overall value for κ, a constant was fitted to the data points, and the results are given as text in the plot. The 2011 value $\kappa = (+0.05 \pm 0.05)\ 1/\mathrm{TeV}$ is used in the analysis [132].

The Bayesian approach is based on Bayes' theorem on probabilities

$$P(A \mid B) = \frac{P(B \mid A) \cdot P(A)}{P(B)} \tag{6.11}$$

with the probability for A happening $P(A)$ and the conditional probability of A happening, when B already happened $P(A \mid B)$. In bayesian statistics $P(A)$ can be interpreted as the degree of believe in the hypothesis A. With that assumption, Eq. 6.11 can be interpreted as

$$P(\text{theory} \mid \text{data}) \propto P(\text{data} \mid \text{theory}) \cdot P(\text{theory}) \tag{6.12}$$

the probability of the theory being true given the data, is proportional to the probability that the data is observed given the theory, times the probability or degree of believe in the theory. $P(\text{data} \mid \text{theory})$ is called the likelihood and $P(\text{theory})$ the prior probability of the theory. Because probabilities have to be normalized to unity, the proportionality in Eq. 6.12 can be transformed to a equation.

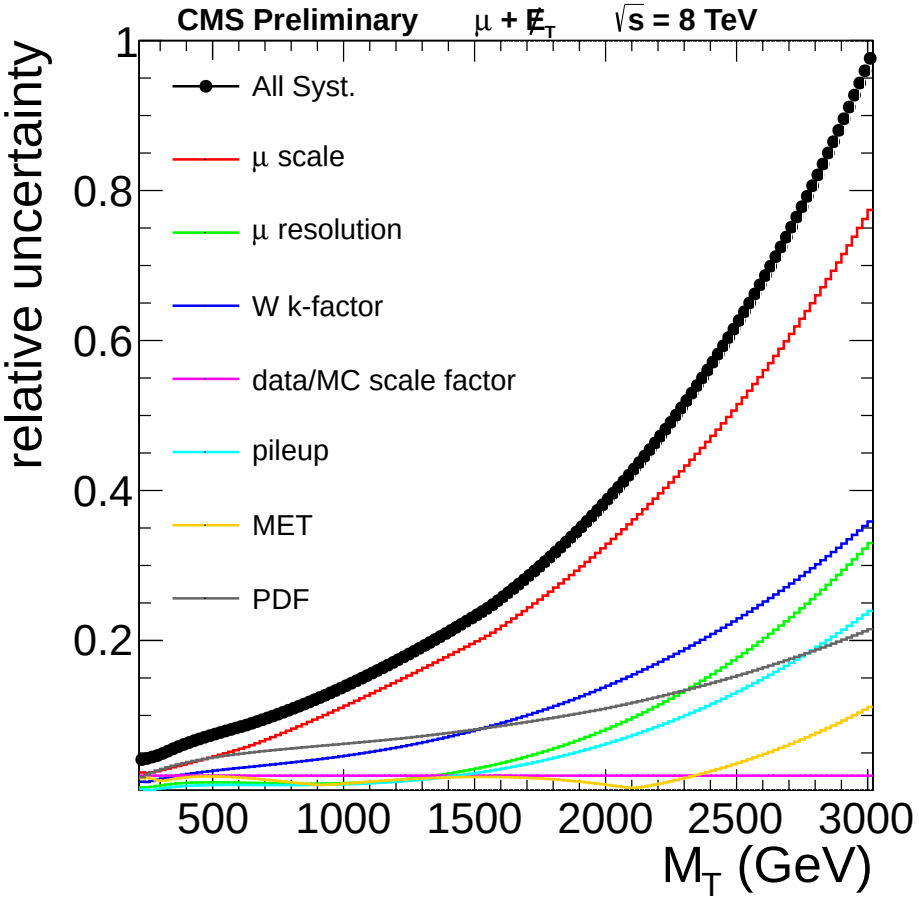

Figure 6.14: Systematic uncertainties: The relative deviation from the main M_T distribution is shown as a function of M_T for the different systematic uncertainties. The combined systematic uncertainty is shown as black markers and is driven mainly by the muon scale uncertainty at high M_T and by the PDF uncertainty at low M_T.

The theory is represented by one parameter, the signal strength modifier

$$\mu_{excl} = \frac{\sigma_{excluded}}{\sigma_{theory}} \tag{6.13}$$

which is used to calculated $\sigma_{excluded}$. The theory is excluded if $\mu_{excl} < 1$ and because μ_{excl} depends on model parameters like the W' or χ masses, it can be used to set an exclusion limit on this mass.

The probability of Eq. 6.12 can be expressed as a function of μ and the number of observed data events n_{obs}

$$P(\mu \mid n_{obs}) = \frac{L(n_{obs} \mid \mu) \cdot \pi(\mu)}{\int L(n_{obs} \mid \mu') \cdot \pi(\mu')\, d\mu'} = \frac{L(n_{obs} \mid \mu) \cdot \pi(\mu)}{C} \tag{6.14}$$

with the likelihood $L(n_{obs} \mid \mu)$, the prior probability $\pi(\mu)$ and the normalization C. The likelihood of observing n_{obs} events, with the expectation of b background events and $\mu \cdot s$ signal events is given by the poisson probability

$$L(n_{obs} \mid \mu) = \frac{(\mu \cdot s + b)^{n_{obs}}}{n_{obs}!} e^{-(\mu \cdot s + b)} \tag{6.15}$$

The prior probability is chosen to be uniform for $\mu \geqslant 0$ and zero otherwise because there is no knowledge on μ and every non negative value has therefore the same probability.

$$\pi(\mu) \begin{cases} 0 & \mu < 0 \\ 1 & \mu \geqslant 0 \end{cases} \tag{6.16}$$

The next step is to use the probability of Eq. 6.14 by integrating the probability from minus infinity to an upper limit, to calculate $\mu_{excl} = \mu_{95}$. This is done by setting the integral equal to 0.95

$$0.95 = \int_{-\infty}^{\mu_{95}} P(\mu \mid n_{obs})\, d\mu = \frac{1}{C} \int_{-\infty}^{\mu_{95}} L(n_{obs} \mid \mu) \cdot \pi(\mu)\, d\mu \tag{6.17}$$

in which case μ_{95} corresponds to a 95 % confidence level and determines the upper limit on μ and therefore the excluded signal strength modifier limit.

In this calculation, the statistical uncertainties are considered by the poisson probability. To account for the systematic uncertainties, additional nuisance parameters ν have to be introduced. Two types of systematic uncertainty can be distinguished, multiplicative uncertainties (like the luminosity) and shape uncertainties (like the muon momentum scale). Both cases have to be treated differently and are explained in the following:

- For a multiplicative uncertainty the probability in Eq. 6.14 depends on μ and and the nuisance parameter g because an additional prior probability $\pi(g)$ has to be introduced for each nuisance parameter. For these systematic uncertainties, a log-normal distribution is used as the prior probability which is a typical choice for non-negative quantities. The log-normal distribution is defined by

$$P_{g,\sigma_g}(x) = \frac{1}{x\sqrt{2\pi}\sigma_g} e^{-\frac{(\ln(x)-g)^2}{2\sigma_g^2}} \tag{6.18}$$

  depending on the mean of the nuisance parameter g and its uncertainty σ_g.

- For uncertainties that change the shape of the distribution, like muon momentum scale, not only the central value x^0 is known, but also x^+ and x^- which correspond to an up-

and a downward shift of the muon momentum scale. For each of these uncertainties, a 'morphing' parameter f is introduced, which is distributed like a gaussian with the mean $\mu_f = 0$ and the width $\sigma_f = 1$ [133]. The number of expected events x^0 is then extrapolated quadratically for $|f| < 1$ and linearly beyond this range

$$x(f) = \begin{cases} \frac{f(f-1)}{2} x^- - (f-1)(f+1) x^0 + \frac{f(f+1)}{2} x^+ & |f| < 1 \\ \frac{x^+ + x^-}{2} + f \cdot \frac{x^+ - x^-}{2} & \text{else.} \end{cases} \tag{6.19}$$

The number of background and signal events in Eq. 6.14 is then replaced by $x(f)$ and the prior probability for $x(f)$ is a gaussian, with the mean $\mu_f = 0$ and the width $\sigma_f = 1$. To incorporate more than one systematic shape uncertainty, the different deviations from x^0 can be added linearly.

To eliminate the dependence on the nuisance parameters $\nu = (g_1, \ldots, g_n, f_1, \ldots, f_m)$, the probability has to be integrated over ν

$$P(\mu \mid n_{obs}) = \int P(\mu, \nu \mid n_{obs}) \, d\nu \tag{6.20}$$

This integration is not analytically solvable and because of the high number of dimensions $\nu = (\nu_1, \cdots, \nu_n)$ the Markov-Chain Monte Carlo (MCMC) method is used. This method performs a random walk, to sample a multi-dimensional distribution $P(x = (x_1, \cdots, x_n))$. The algorithm starts at a point x^0 and chooses a random point x^t, if $P(x^t)$ is larger than $P(x^0)$, x^t is the next staring point. If $P(x^t)$ is smaller than $P(x^0)$, then x^t is the next starting point, with the probability $P(x^t)/P(x^0)$, else x^0 stays the starting point. By this procedure, the distribution $P(x)$ is sampled, because points with a high probability are chosen more often than points with a low probability. If this procedure is repeated many times and x is recorded, the histogram of x will converge to $P(x)$. More details on MCMC and its variations can be found in Ref. [134].

This presented way of calculating a limit works for one bin[7], where all events above a certain threshold are taken into account for the limit calculation[8]. But in this approach, only the information of the event number above the threshold is used. To take into account information of the shape of the signal and background distribution and to consider the region below the threshold, the limit has to be generalized to a shape based or multi-bin limit. For this approach the M_T spectrum is not integrated above a M_T-threshold, but divided into different bins according to the detector resolution. This binning is also used to display the final M_T-distribution in Fig. 6.5.

Multiple bins can be considered into the limit calculation by multiplying the different likelihoods in Eq. 6.17 resulting in

$$0.95 = \int_{-\infty}^{\mu_{95}} \pi(\mu) \prod_{i \in \text{bins}} L_i(n_{obs} \mid \mu) \, d\mu \tag{6.21}$$

This method of multiplying likelihoods can also be used to combine different channels, for example the muon and electron channel. Detailed information on a comparison between

7 This so called single-bin limit was used in previous publications [5].
8 The choice for a threshold is not obvious and needs to be optimized, the threshold is ~ 1000 GeV.

the multi-bin and the single-bin limit and on the influence of the bin size can be found in Ref. [60].

This calculation of the limit gives the observed limit, which corresponds to the measured data. Also interesting is its comparison with the expected limit, which is expected if only the Standard Model and no new physics is observed. For the calculation of the expected limit, the number of observed events is replaced by a diced number of events, based on the number of background events expected for the same luminosity. The values for the systematic uncertainty $x^{\pm}$ are also diced according to their uncertainty. This procedure of recalculating the limit with new event numbers according to the background expectation is repeated ~ 600 times. The median of this distribution of limits is taken as the expected limit and also the one and two sigma bands can be computed and correspond to the 68 % and 95 % intervals.

7

RESULTS

There is no indication for new physics in the final M_T distribution (Fig. 6.5), and limits are set on the W' and Dark Matter model. In this section, the resulting limits on W' (Sec. 7.1) and Dark Matter (Sec. 7.2) are presented. For both signal models, a combination of the results with the electron channel is performed. The electron selection is very briefly summarized in Sec. A.5 and the analysis is explained in detail in Ref. [60].

7.1 W′

For the SSM W' model, the limit is shown in Fig. 7.1 as a cross section limit as a function of $M_{W'}$ for the muon channel.

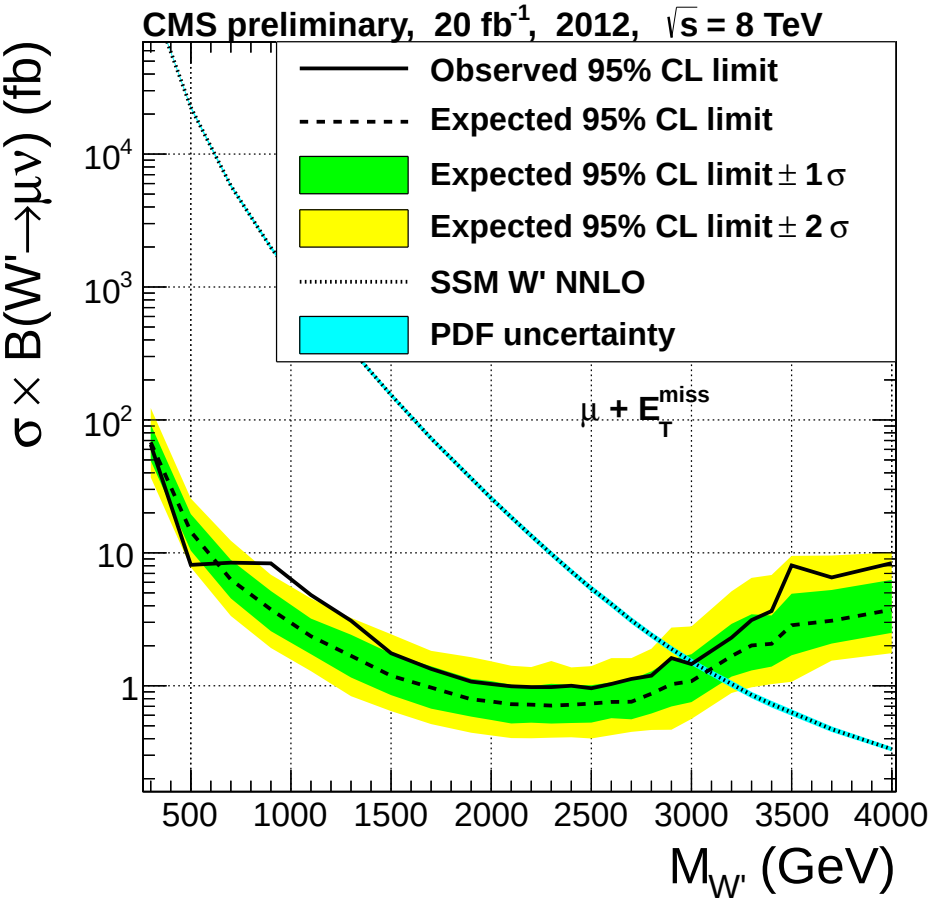

Figure 7.1: Cross section limit on the SSM W' model in the muon channel: The expected limit is shown as a dashed line with $\pm 1, 2\,\sigma$ bands in green and yellow. The observed limit is shown as a solid line. Cross sections larger than the limit are excluded with 95 % C.L.. The theoretical W' cross section is shown with its PDF uncertainties in cyan. The intersection between the theory expectation and the observed limit marks the mass limit of $M_{W'} < 3\,\text{TeV}$ and an expected exclusion of $M_{W'} < 3.1\,\text{TeV}$.

To derive a mass limit, the cross section limit is compared with the theoretical cross section expectation. If the cross section limit excludes the theoretical cross section, this W' mass is excluded. This results in a mass exclusion limit from the muon channel of $M_{W'} < 3\,\text{TeV}$. The expected limit is a smooth function of M_T and is driven by the signal efficiency (Fig. 6.8)[1]. The observed limit shows some features, driven by the data distribution. The biggest disagreement between Monte Carlo prediction and data measurement is at $M_T \sim 900\,\text{GeV}$ and can also be seen in the cross section limit for $M_{W'} \sim 900\,\text{GeV}$, which is more than two sigma weaker than expected. This was not seen in a previous analysis (Ref. [58]) which already excluded this W' mass and also indicates a statistical fluctuation. For most of the W' masses, the agreement between the observed and expected limit is better than one sigma.

To gain sensitivity, a combination with the electron channel is performed. The result is shown in Fig. 7.2.

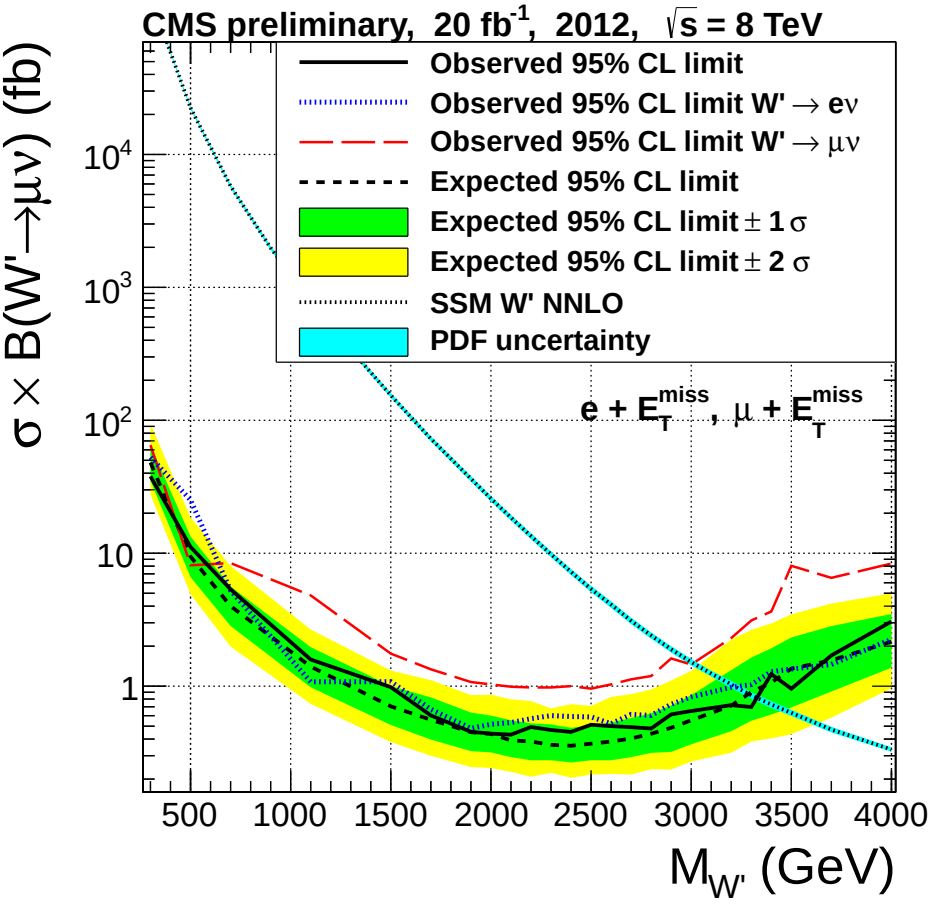

Figure 7.2: Cross section limit on the SSM W' model in the combined muon and electron channel: The observed and expected limit are shown in black lines and the $\pm 1, 2\,\sigma$ for the expected limit are shown for the combined channel. The observed limit in the muon channel (red dashed line) and in the electron channel (blue dotted line) are shown as a comparison. The mass limit for the combined channels is $M_{W'} < 3.35\,\text{TeV}$ with an expected exclusion of $M_{W'} < 3.3\,\text{TeV}$.

In the combination, the deviation between expected and observed limit is everywhere smaller than one sigma. The comparison between the electron and muon channel shows

1 The limit is weaker for W' masses with a lower signal efficiency and vice versa.

that the exclusion limit in the electron channel is stronger than in the muon channel due to the higher signal efficiency in the electron channel, but the combination of both channels improves the limit over most of the $M_{W'}$ range. The W' mass limit for the combined channels is

$$M_{W'} < 3.35\,\text{TeV at } 95\,\%\,\text{C.L.} \tag{7.1}$$

and therefore the most stringent constraint set on a SSM W' model up to now.

7.2 DARK MATTER

For the Dark Matter model, the cross section limits are shown in Fig. 7.3 as a function of the Dark Matter mass M_χ. The limits are provided in terms of the proton-proton (pp) cross section and are calculated for the spin independent vector coupling (Fig. 7.3-bottom row) , the spin dependent axial-vector coupling (Fig. 7.3-top row) and the three different values of ξ, (columns). For the Dark Matter model, the limit is always calculated for the combination of electron and muon channel, because the coupling to the final state lepton happens via the W boson, and is therefore independent of the Dark Matter model.

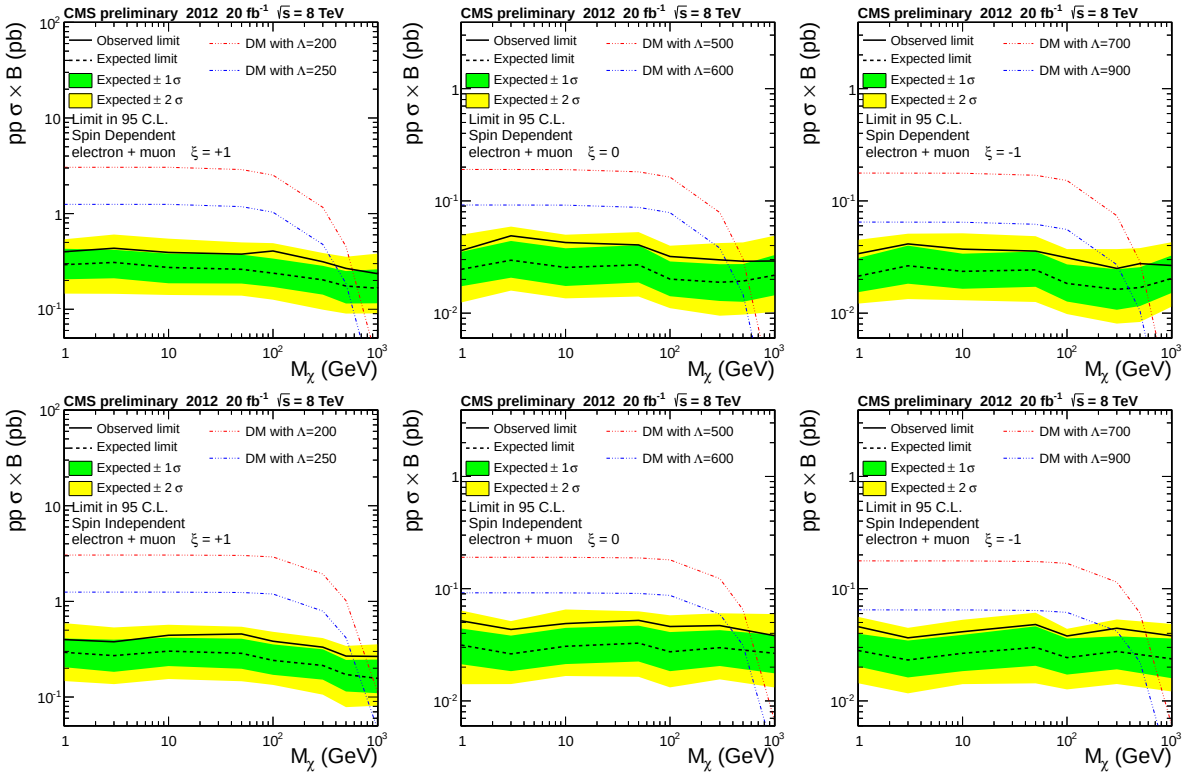

Figure 7.3: Dark Matter proton-proton cross section limit: The cross section limit is shown for spin dependent axial-vector coupling (top-row), the spin independent vector coupling (bottom row), $\xi = +1$ (left column), $\xi = 0$ (middle column) and $\xi = -1$ (right column) as a function of M_χ with 95 % C.L.. The dependence of the limit on the coupling and M_χ is very small, as expected from the signal shape, which does not differ with coupling or M_χ. As the signal shape changes with ξ, the limit gets stronger from $\xi = +1$ to $\xi = 0, -1$ because the signal extents to higher M_T where the background is lower and the signal exclusion is stronger. As a comparison, the theoretical cross section is shown in each limit plot for two example values of Λ. All observed limits agree with the expected limits better than two sigmas.

The different cross section limits are rather independent of M_χ, as the signal shape does not change much for different M_χ (see Fig. 5.7). Also the difference between vector and axial-vector coupling in the signal shape is quite small, resulting in comparable limits for both couplings. The limits differ for different values for ξ. For ξ = +1 the signal spectrum falls more steeply, and hence only the low and medium M_T-ranges contribute to the search. For the two cases of ξ = 0,-1 a possible signal would extend to higher M_T. This is reflected in a similar behavior of the limit as a function of M_χ for these. The expected limit changes from 300 fb for destructive interference to 30 fb for the no interference case and to 20 fb for constructive interference.

For all six limits, the observed limit is within the two σ band of the expected limit. As a comparison, for each limit the theoretical cross section for two values of Λ is shown. The intersection of the theoretical cross section and the observed cross section limit can be used to calculate a limit on Λ. This limit recalculation is explained in the following section.

7.2.1 *Limit transformation*

The limit on the proton-proton cross section for the Dark Matter model can be translated into a limit on the interaction scale Λ and on the Dark Matter-Nucleon cross section. The recalculation and the results are presented in this section.

The excluded cross sections translate into a limit on the parameter Λ, shown in Fig. 7.4 for two examples (all six limits on Λ are shown in Fig. 7.7), by using the cross section for the produced sample and the formula:

$$\Lambda^4_{obs} = \frac{\sigma_{gen} \cdot \Lambda^4_{gen}}{\sigma_{obs}}. \tag{7.2}$$

As can be seen in Fig. 5.6, the Dark Matter production cross sections steeply decreases for masses of $M_\chi > 500\,\text{GeV}$ due to limited phase space, which is necessary to produce a pair of $> 500\,\text{GeV}$ particles plus a real W-boson. For lower masses, the cross section is flat with respect to M_χ therefore $\Lambda < 260\,\text{GeV}$ can be excluded up to $M_\chi = 200\,\text{GeV}$ for destructive interference ($\xi = +1$) and $\Lambda < 600\,\text{GeV}$ for no interference ($\xi = 0$) in M_χ up to 200 GeV. The constructive interference case ($\xi = -1$) can exclude $\Lambda < 1200\,\text{GeV}$ up to $M_\chi = 100\,\text{GeV}$. While the difference between vector-like and axial-vector-like coupling is small for low M_χ in all interference cases, a difference can be observed in the high M_χ region above 100 GeV. The cross section for vector-like coupling is larger than the axial-vector coupling for higher values of M_χ.

These exclusion limits are not easily comparable with those derived from direct searches such as Xenon [135] or CDMS [136], because the cross section in direct searches is given for a Dark Matter-Nucleon interaction. Therefore, the limit has to be recalculated into a limit of the excluded nucleon cross section for a given Λ and M_χ. This recalculation is based on Ref. [137].

For the scattering cross section off a nucleon N (proton or neutron) the quark content of this nucleon $\langle N|\bar{q}C_\mu q|N\rangle$ for each coupling has to be known ($C_\mu = \gamma_\mu$ for vector and $C_\mu = \gamma_\mu\gamma_5$ for axial-vector coupling). The resulting nucleon Dark Matter interaction terms are

$$\mathcal{L}_V = f_q^N \frac{1}{\Lambda^2} \left(\bar{N}\gamma_\mu N\right)\left(\bar{\chi}\gamma_\mu\chi\right) \tag{7.3}$$

$$\mathcal{L}_{AV} = \Delta_q^N \frac{1}{\Lambda^2} \left(\bar{N}\gamma_\mu\gamma_5 N\right)\left(\bar{\chi}\gamma_\mu\gamma_5\chi\right) \tag{7.4}$$

The effective cross section terms for low Dark Matter velocities are

$$\sigma_{AV}^N = \sigma_{SD}^N = \frac{3\mu^2}{\pi\Lambda^4} \cdot \left(\sum_q \xi_q \cdot \Delta_q^N\right)^2 \text{ and } \sigma_V^N = \sigma_{SI}^N = \frac{\mu^2}{\pi\Lambda^4} \cdot \left(\sum_q \xi_q \cdot f_q^N\right)^2 \tag{7.5}$$

where $\mu = \frac{m_\chi m_p}{m_\chi + m_p}$ is the reduced mass of the WIMP-Nucleon (proton or neutron) system and $\Lambda^4 = \Lambda_d^4 + \Lambda_u^4$. The interference parameter ξ_q is equal to ξ for $q = d$ and equal to 1 for all other quarks. The form factors Δ_q^N and f_q^N characterize the nucleon structure and follow from $\langle N|\bar{q}C_\mu q|N\rangle$.

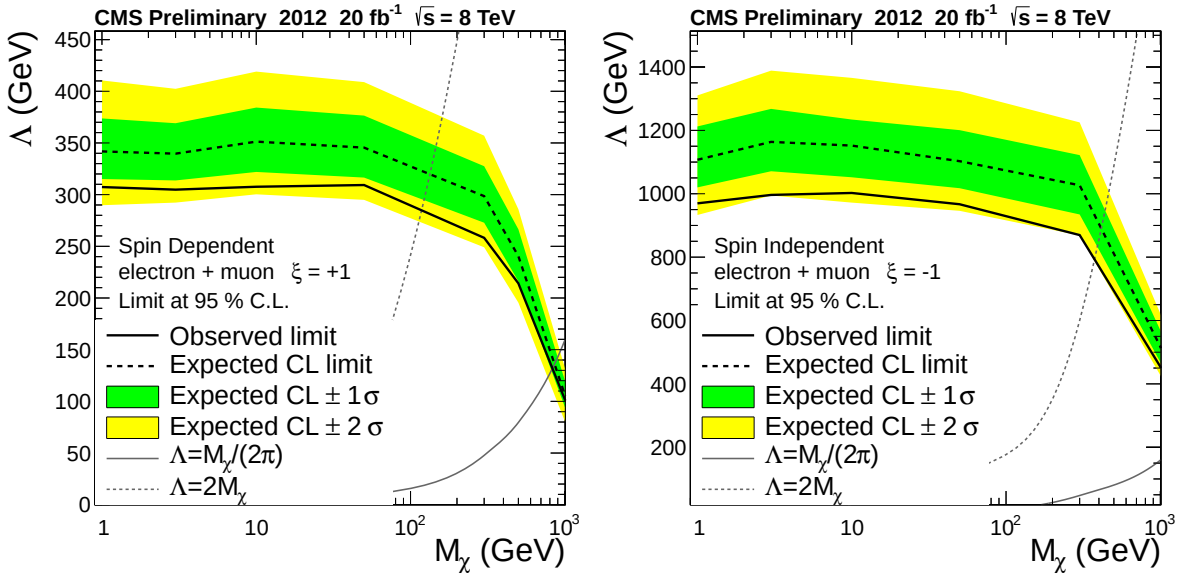

Figure 7.4: Dark Matter Λ limit: Shown are two examples for a limit on the interaction scale Λ, all six limits are shown in Fig. 7.7. The left plot shows the limit for the spin dependent axial-vector coupling and $\xi = +1$, while the right plot shows the limit for the spin independent vector coupling and $\xi = -1$. The limit is derived from the proton-proton cross section limit by recalculating it into a limit on Λ. This limit is proportional to the theoretical cross section and therefore the limit shape is comparable to the cross section as a function of M_χ (Fig. 5.6). All values for Λ smaller than the limit are excluded with 95 % C.L.. In addition two lines show the region of validity (above the gray lines) of the theory and are explained in detail in Sec. 7.2.2.

The vector coupling is sensitive to the number of quarks minus the number of antiquarks, which are exactly the number of valence quarks. This results in $f_u^p = f_d^n = 2$, $f_d^p = f_u^n = 1$ and $f = 0$ for other quarks. The vector coupling is the only coupling without theoretical uncertainties for going from the quark interaction to the nucleon interaction [138].

The axial-vector form factors are $\Delta_u^p = \Delta_d^n = 0.842 \pm 0.012$, $\Delta_d^p = \Delta_u^n = -0.427 \pm 0.013$ and $\Delta_s^p = \Delta_s^n = -0.085 \pm 0.018$. These numbers are measured in deep-inelastic scattering experiments, where polarized positrons scatter off polarized hydrogen targets [139].

The sum over the quark types results in $f^N = \left(\sum_q f_q^N\right)^2 = 3$ and $\Delta^N = \left(\sum_q \Delta_q^N\right)^2 = 0.33$ for $\xi = +1$. The cross section limits are traditionally shown in units of cm^2, in Fig. 7.5 for the

spin dependent coupling and in Fig. 7.6 for for the spin independent, with a 90% confidence level.

For a comparison with other collider searches the mono-jet [66] result is also shown, where instead of a W boson a gluon is radiated, resulting in one jet recoiling against $\not{E}_T$. The mono-jet limit is about two orders of magnitude better than the limit of the combined electron and muon channel due to a higher production cross section in the mono-jet channel for $\xi = +1$. The mono-jet channel is not sensitive to interference effects, therefore the analysis in the electron and muon channel is still an important channel[2].

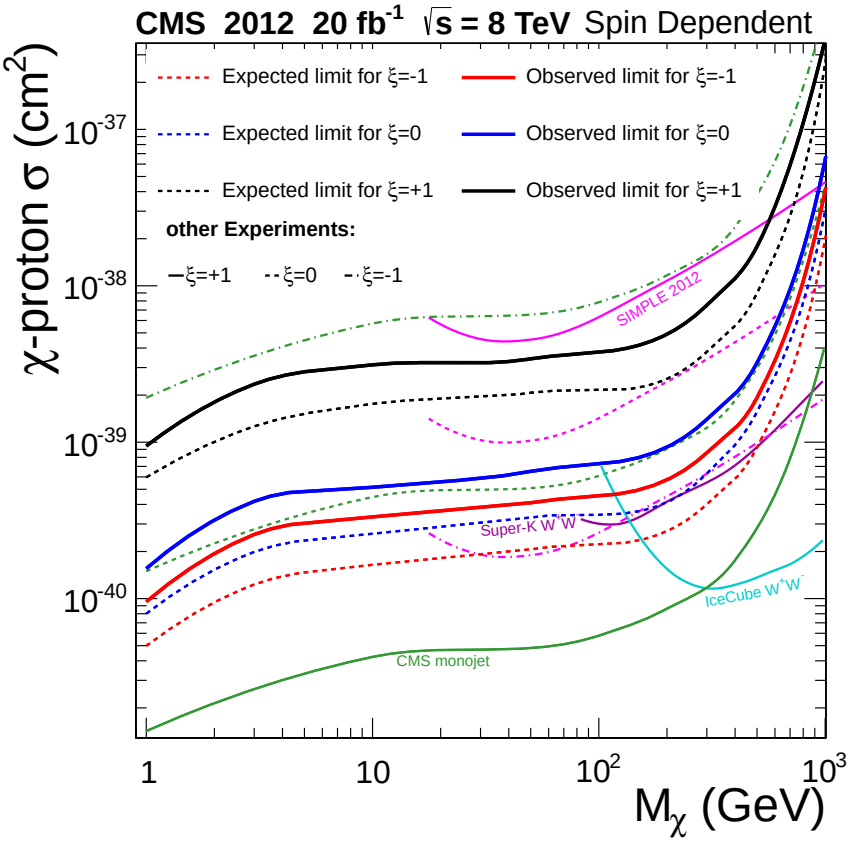

Figure 7.5: Spin dependent Dark Matter-proton cross section limit: The Dark Matter-nucleon cross section limit is shown for the spin dependent axial-vector coupling. The limit is calculated with 90 % C.L. to compare it to other searches for Dark Matter. The CMS mono-jet limit is shown as a comparison for a collider search (green lines), where instead of a W boson a gluon is produced. Due to the higher production cross section, the limit is more strict for $\xi = +1$. The Super-K and IceCube limits are shown as indirect detection limits. The other limits that are shown are from the direct detection experiment SIMPLE.

Different direct detection experiments are shown as a comparison (Simple [140], Xenon 100(2012) [135], CoGeNT [141] and CDMSII [136]) which are more sensitive for a spin independent coupling and a Dark Matter mass of $M_\chi > 5\,\text{GeV}$. For low masses and a spin independent coupling and for the spin dependent coupling the limits determined in the electron and muon and also the mono-jet channel are more strict than the direct detection limit and also the coupling to second generation quarks can only be studied at the high energies at

2 The difference for the three values of ξ in the mono-jet channel are due to the recalculation in a Dark Matter-proton cross section.

the LHC. The direct detection experiments suffer under large systematic uncertainties from astrophysical assumptions such as the Dark Matter velocity and density. These effects are not taken into account for the direct detection limits, but have no effect on the searches of the LHC. The limits from other experiments were determined with $\xi = +1$, to compare them to this analysis also the limits for $\xi = 0, -1$ were calculated. This calculation is explained in Sec. A.6 in the appendix.

For the spin dependent coupling two limits of indirect detection experiments (Super-K [142] and IceCube [143]) are shown as comparison which calculate a more strict limit than the electron and muon channel for Dark Matter masses $M_\chi > 100\,\text{GeV}$, but assume a total decay into W^+W^- pairs.

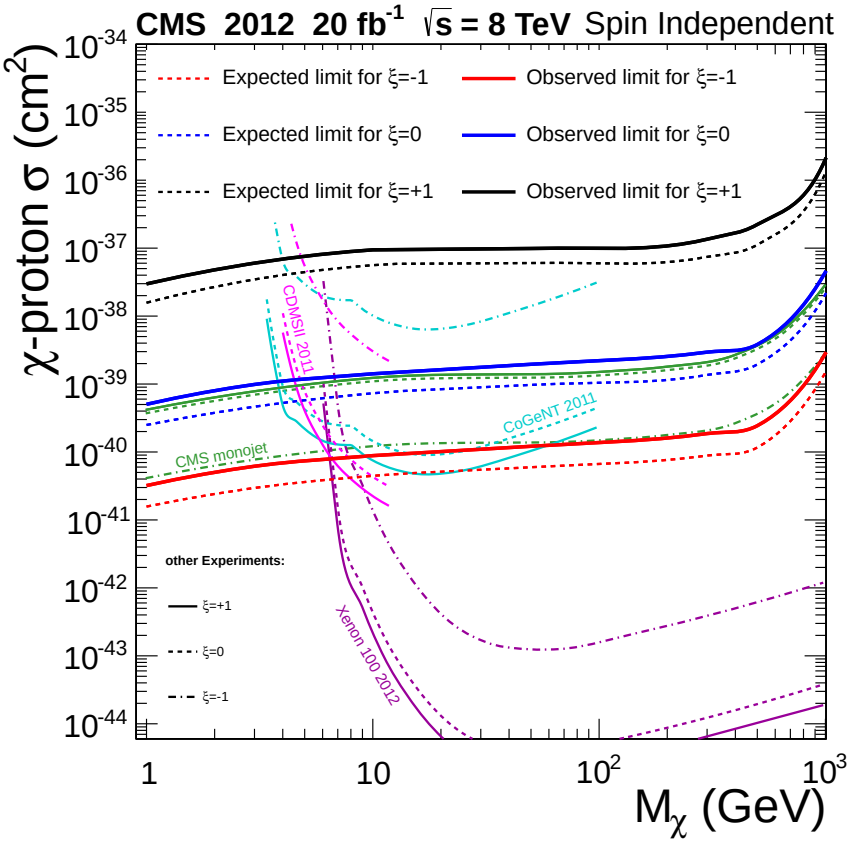

Figure 7.6: Spin independent Dark Matter-proton cross section limit: The Dark Matter-nucleon cross section limit is shown for the spin independent vector coupling. The limit is calculated with 90 % C.L. to compare it to other searches for Dark Matter. The CMS mono-jet limit is shown as a comparison for a collider search (green lines). The other limits that are shown are from direct detection experiments (Xenon 100, CoGeNT and CDMS) and are more strict than the collider limits for Dark Matter masses $M_\chi \gtrsim 5\,\text{GeV}$.

7.2.2 *Limitations of the Theory*

As the theory used to describe Dark Matter is an effective field theory it has some limitations. The theory is only valid when the mediator mass is much larger than the typical energy of the reaction. It is not obvious what would happen in regions of parameter space where the theory is not valid. It could under- or over-estimate the processes. The energy scale Λ can be identified with basic theory parameters via $\Lambda \sim M_\phi/\sqrt{g_{SM} g_\chi}$ where M_ϕ is the mass of

the exchanged particle ϕ, and g_{SM} and g_χ are the couplings. The first requirement for the theory to be valid is that $M_\phi > 2m_\chi$. For the theory to be perturbatively expandable at least $g_{SM}g_\chi \lesssim (4\pi)^2$ has to be fulfilled. These arguments combined results in the requirement for the theory to be valid it has to fulfill $m_\chi \lesssim 2\pi\Lambda$. To compare it with a stricter requirement on the couplings, $g_{SM}g_\chi \lesssim 1$ has also been calculated, which results in the requirement $m_\chi \lesssim \Lambda/2$. Both of these theory limitations are shown in Fig. 7.4 and Fig. 7.7 as gray lines (solid for $m_\chi \lesssim 2\pi\Lambda$, and dashed for $m_\chi \lesssim \Lambda/2$).

7.2.2.1 *Relic density*

To compare the results not only with direct detection experiments but also with cosmological observations of the relic Dark Matter density, a calculation based on Ref. [144, 63] is necessary. This calculation is based on some assumptions. Without them, the calculation is no longer valid. No effects due to resonances or coannihilation are taken into account [145], the reaction is dominated by either vector or axial-vector coupling, the mediating particle is much heavier than χ and only decays to fermion antifermion pairs are considered, neglecting final states with gauge or Higgs bosons. The idea is to calculate the value for Λ depending on M_χ preferred by the measurement of the relic density $\Omega_\chi h^2$ (h is related to the Hubble constant via $H_0 = 100h\,\mathrm{km\,s^{-1}\,Mpc^{-1}}$).

The calculation starts with the couplings of two Dark Matter particles χ to two Standard Model fermions f and the substitution $\frac{1}{\Lambda^2} = \frac{G}{\sqrt{2}}$

$$\mathcal{L}_V = \frac{G_f}{\sqrt{2}}\bar{\chi}\gamma^\mu\chi\bar{f}\gamma_\mu f \tag{7.6}$$

$$\mathcal{L}_{AV} = \frac{G_f}{\sqrt{2}}\bar{\chi}\gamma^\mu\gamma^5\chi\bar{f}\gamma_\mu\gamma_5 f \tag{7.7}$$

The first step is to calculate the annihilation cross section to fermion-antifermion pairs as a function of the square of the center of mass energy s

$$\sigma_V = \frac{1}{32\pi}\sum_f G_f^2 c_f \sqrt{\frac{s-4m_f^2}{s-4M_\chi^2}}\left[s + 4M_\chi^2 + \frac{\left(s-4M_\chi^2\right)\left(s-4m_f^2\right)}{3s} + 4m_f^2\right] \tag{7.8}$$

$$\sigma_{AV} = \frac{1}{32\pi}\sum_f G_f^2 c_f \sqrt{\frac{s-4m_f^2}{s-4M_\chi^2}}\left[s - 4M_\chi^2 + \frac{\left(s-4M_\chi^2\right)\left(s-4m_f^2\right)}{3s} + 4m_f^2\right] \tag{7.9}$$

where the sum is over the final state fermions and c_f is the color factor, 3 for quarks and 1 for leptons. To determine the density of relic WIMPs, the Boltzmann equation has to be solved which describes the time evolution of the number density n_χ of the WIMPs

$$\frac{dn_\chi}{dt} + 3Hn_\chi = -\langle\sigma|v|\rangle\left[(n_\chi)^2 - \left(n_\chi^{eq}\right)^2\right] \tag{7.10}$$

where $H \equiv \dot{a}/a = \sqrt{8\pi\rho/3M_{Pl}}$ is the Hubble constant and $\langle\sigma|v|\rangle$ is the thermally averaged WIMP annihilation cross section. In thermal equilibrium, the number density of WIMPs is given by

$$n_\chi^{eq} = g\left(\frac{M_\chi T}{2\pi}\right)^{\frac{3}{2}}\exp\left(-\frac{M_\chi}{T}\right) \tag{7.11}$$

where $g = 2$ is the number of degrees of freedom of a fermionic WIMP. Since we are considering cold thermal relics, freeze-out occurred when WIMPs were non-relativistic and had velocities much smaller than unity. Substituting $s \approx 4M_\chi^2 + M_\chi^2 v^2$ to Eqs. 7.8 & 7.9, and expanding in powers of the relative velocity between two annihilating WIMPs up to order v^2, we find

$$\sigma_V |v| \approx \frac{1}{4\pi} \sum_f G_f^2 c_f M_\chi^2 \sqrt{1 - \frac{m_f^2}{M_\chi^2}} \left[\left(2 + \frac{m_f^2}{M_\chi^2}\right) + \frac{1}{12}\left(1 - \frac{m_f^2}{M_\chi^2}\right) v^2 \right] \tag{7.12}$$

$$\sigma_{AV} |v| \approx \frac{1}{4\pi} \sum_f G_f^2 c_f M_\chi^2 \sqrt{1 - \frac{m_f^2}{M_\chi^2}} \left[\frac{m_f^2}{M_\chi^2} + \frac{1}{12}\left(2 - \frac{m_f^2}{M_\chi^2}\right) v^2 \right] \tag{7.13}$$

Numerical solutions of the Boltzmann equation yield a relic density of

$$\Omega_\chi h^2 \approx \frac{1.04 \times 10^9 x_F}{M_{Pl}\sqrt{g_*}\,(a + 3b/x_F)} \tag{7.14}$$

where $x_F = m_\chi / T_F$, T_F being the temperature at freeze-out, g_* is the number of relativistic degrees of freedom at freeze-out ($g_* \approx 92$ for $T_F = \mathcal{O}(10\,GeV)$), and a and b are the terms in $\sigma |v| = a + bv^2 + \mathcal{O}(v^4)$. WIMPs with electroweak scale masses and couplings generically freeze out at temperatures in the range of approximately $x_F \approx 20 - 30$.

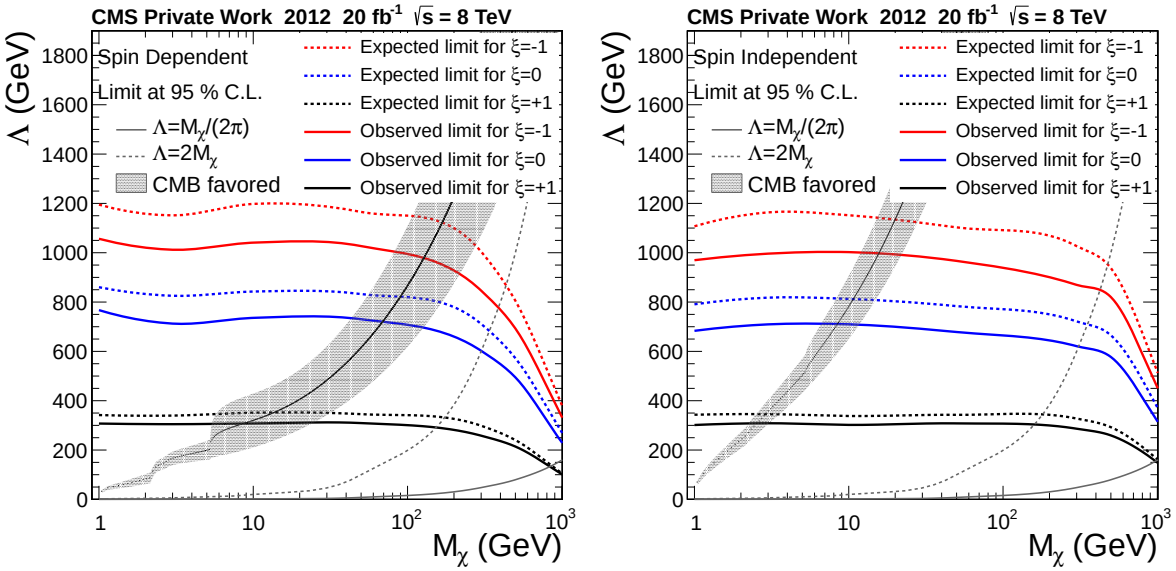

Figure 7.7: Dark Matter limit of Λ against M_χ for the three $\xi = 0, \pm 1$ values. The left Plot shows the limit for the spin dependent coupling, the right one for spin independent coupling. The expected limits are shown as a dashed line, the observed limits are shown as a solid line. The validity limits of the theory are shown as gray lines. The regions favored by the CMB observation [47] are shown as grey shaded regions.

Assuming that $G_f = G$ does not depend on the Standard Model fermion, Eq. 7.14 can be solved for G and therefore for Λ. With the newest measurement of the relic Dark Matter density $\Omega_\chi h^2 = 0.1187 \pm 0.0017$ via the cosmic microwave background (CMB)[47] one gets the preferred Λ values shown in Fig. 7.7 (labeled as CMB favored). To estimate an error on this calculation, the parameters in the calculation are varied within their known accuracy.

8 CONCLUSION

In this thesis, the results of a search for new physics in the final state with one muon and missing transverse energy in proton-proton collisions was performed. The muon and $\not{E}_T$ reconstruction, identification and correction were improved compared to previous analyses. The amount of data used for this analysis corresponds to $20\,\text{fb}^{-1}$ at a center of mass energy of $\sqrt{s} = 8\,\text{TeV}$. The background expectation was derived from Monte Carlo simulation, and the systematic uncertainties on the background and the simulation of signal processes were studied in detail.

Two models of new physics beyond the Standard Model were studied in this analysis, the production of new heavy charged vector bosons W' and the pair production of two Dark Matter particles recoiling against a Standard Model W boson. No indications for new physics were found and limits were set on the two studied models, with a bayesian, shape sensitive approach.

The W' boson is excluded with 95 % C.L. for $M_{W'} < 3\,\text{TeV}$ (with an expected exclusion of $M_{W'} < 3.1\,\text{TeV}$) in the muon channel and for $M_{W'} < 3.35\,\text{TeV}$ (with an expected exclusion of $M_{W'} < 3.3\,\text{TeV}$) in the combination of the muon and electron channel. These are the strongest limits on this SSM W' model at the moment.

The limits on the Dark Matter model can be set on the proton-proton production cross section, on the interaction scale Λ and on the Dark Matter-nucleon cross section. The limit also depends on the studied coupling (spin dependent axial-vector or spin independent vector coupling) and the interference parameter ξ ($\xi = +1$: destructive interference, $\xi = 0$: no interference and $\xi = -1$: constructive interference). The limits set on the Dark Matter model also depend on the mass of the Dark Matter particle and are listed for the example of $M_\chi = 1\,\text{GeV}$ with 95 % C.L. in Tab. 8.1.

coupling	ξ	pp cross section (pb)	Λ (GeV)	DM-N cross section (cm^{-2})
axial-vector	-1	$3.5 \cdot 10^{-2}$ $(2 \cdot 10^{-2})$	1050 (1200)	10^{-40} $(6 \cdot 10^{-41})$
	0	$3.5 \cdot 10^{-2}$ $(2.5 \cdot 10^{-2})$	750 (850)	$2 \cdot 10^{-40}$ (10^{-40})
	$+1$	$3 \cdot 10^{-1}$ $(2 \cdot 10^{-1})$	300 (350)	$1.5 \cdot 10^{-39}$ $(8 \cdot 10^{-40})$
vector	-1	$4.5 \cdot 10^{-2}$ $(3 \cdot 10^{-2})$	975 (1125)	$3 \cdot 10^{-41}$ $(2 \cdot 10^{-41})$
	0	$5 \cdot 10^{-2}$ $(3 \cdot 10^{-2})$	700 (800)	$5 \cdot 10^{-40}$ $(2.5 \cdot 10^{-40})$
	$+1$	$4 \cdot 10^{-1}$ $(3 \cdot 10^{-1})$	300 (350)	$2 \cdot 10^{-38}$ $(1.5 \cdot 10^{-38})$

Table 8.1: Limits on the Dark Matter model: The limits on the proton-proton (pp) cross section, the interaction scale Λ and the Dark Matter-Nucleon (DM-N) cross section are listed depending on the coupling and parameter ξ for the example mass of $M_\chi = 1\,\text{GeV}$. The observed limit is listed, while the expected limit is given in brackets.

This analysis was published in combination with the electron channel in Ref. [6] for the W' model and in Ref. [7] for the Dark Matter model.

APPENDIX

A

APPENDIX

A.1 EVENT DISPLAYS

Event			M_T (GeV)	$\not{E}_T$ (GeV)	muon		
Run	Lumi Section	Event			p_T (GeV)	η	ϕ
208307	287	445184756	2122 ± 256	1081 ± 126	1041.2 ± 125.6	-0.27	-0.86

Table A.1: Details on the event with the highest recorded M_T in 2012.

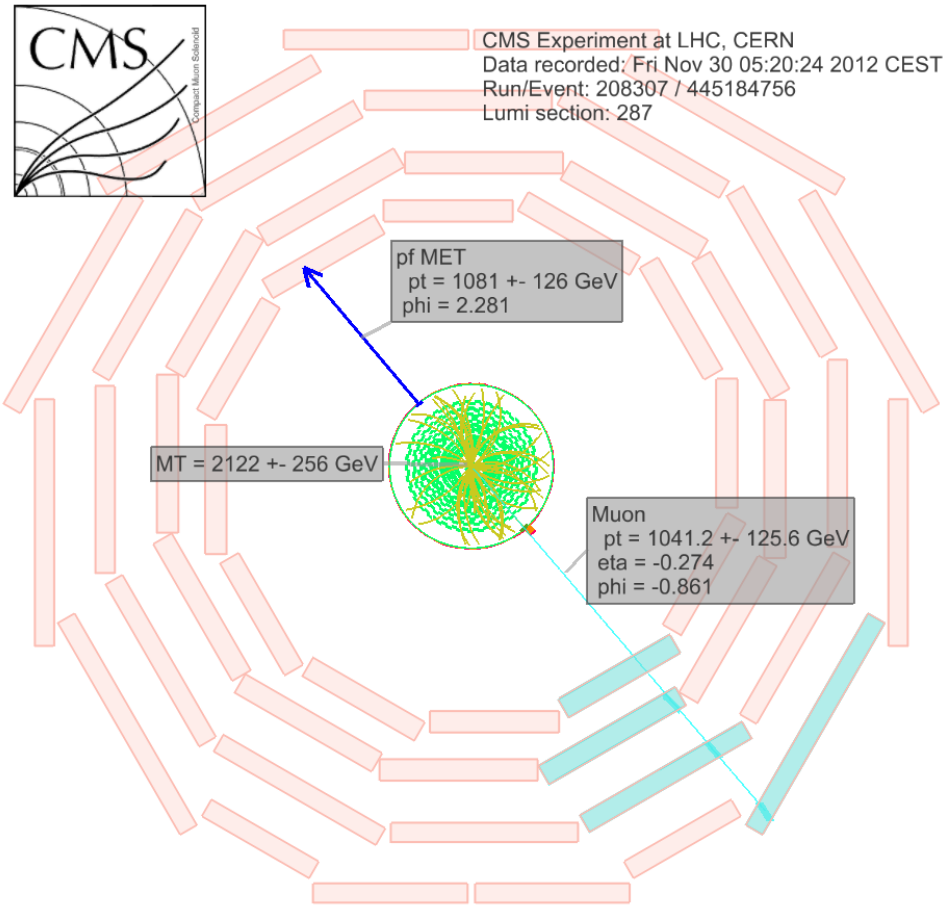

Figure A.1: Event display of the event with the highest recorded M_T in 2012, shown in the $r-\phi$ plane. All objects in the event with energies > 1 GeV are shown.

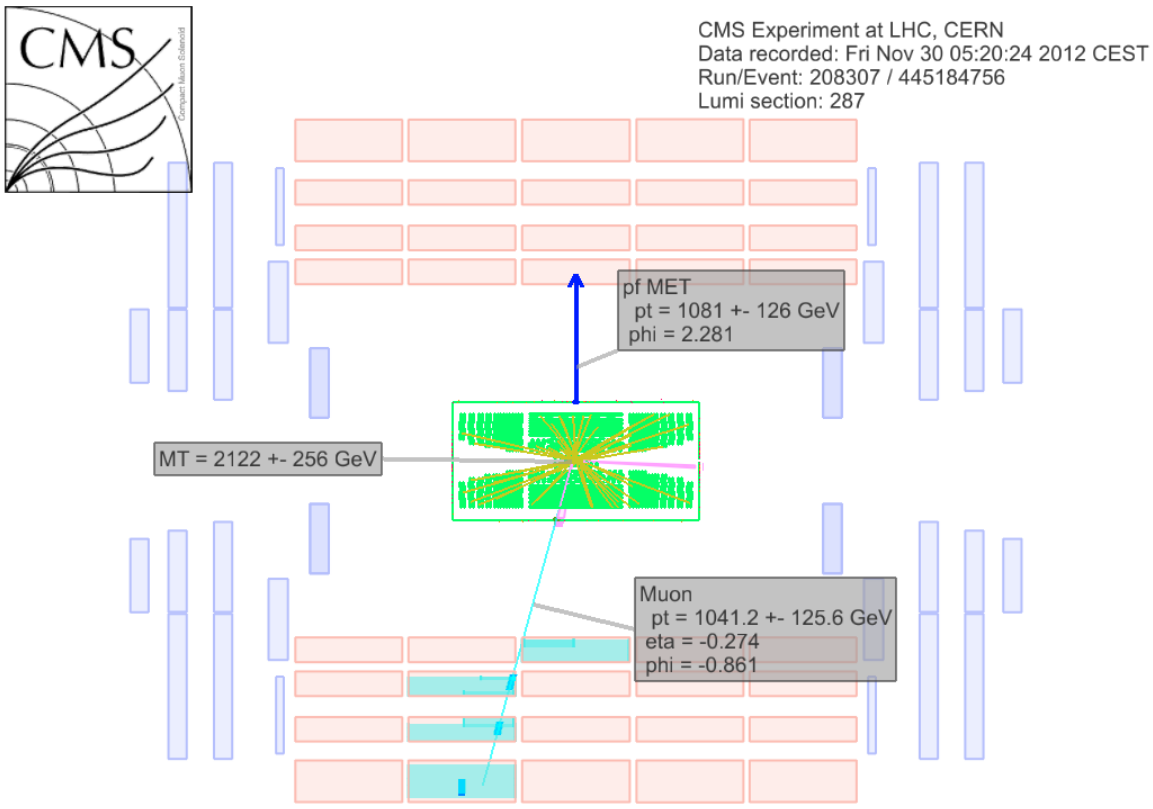

Figure A.2: Event display of the event with the highest recorded M_T in 2012, shown in the $r-z$ plane. All objects in the event with energies $> 1\,\text{GeV}$ are shown.

A.2 MONTE CARLO SAMPLES

A.2.1 *Background Monte Carlo*

process	generator	kinematic cuts	cross section (pb^{-1})	order	k-factor	number of events
$W \to \mu\nu$	PYTHIA	no cuts	9130	LO	binned (NLO)	$\sim 76\text{M}$
$W \to \mu\nu$	PYTHIA	$500 > \hat{p}_T > 100\,\text{GeV}$	1.457	LO	binned (NLO)	$\sim 1\text{M}$
$W \to \mu\nu$	PYTHIA	$\hat{p}_T > 500\,\text{GeV}$	0.001525	LO	binned (NLO)	$\sim 1\text{M}$
$W \to \tau\nu$	PYTHIA	no cuts	9130	LO	binned (NLO)	$\sim 48\text{M}$
$W \to \tau\nu$	PYTHIA	$500 > \hat{p}_T > 100\,\text{GeV}$	1.457	LO	binned (NLO)	$\sim 1\text{M}$
$W \to \tau\nu$	PYTHIA	$\hat{p}_T > 500\,\text{GeV}$	0.001525	LO	binned (NLO)	$\sim 1\text{M}$
$Z/\gamma \to \mu\mu$	POWHEG	$m_{\mu\mu} > 20\,\text{GeV}$	1871	NLO	1.024 (NNLO)	$\sim 48\text{M}$
$Z/\gamma \to \mu\mu$	POWHEG	$m_{\mu\mu} > 120\,\text{GeV}$	11.89	NLO	1.024 (NNLO)	$\sim 100\text{k}$
$Z/\gamma \to \mu\mu$	POWHEG	$m_{\mu\mu} > 200\,\text{GeV}$	1.485	NLO	1.024 (NNLO)	$\sim 100\text{k}$

Table A.2: Background samples used in the analysis. The order of the cross section is given in the fifth column. Multiplying the cross section with the k-factor corrects to the order given for the k-factor.

process	generator	kinematic cuts	cross section (pb^{-1})	order	k-factor	number of events
$Z/\gamma \to \mu\mu$	POWHEG	$m_{\mu\mu} > 400\,\mathrm{GeV}$	0.1086	NLO	1.024 (NNLO)	~ 100k
$Z/\gamma \to \mu\mu$	POWHEG	$m_{\mu\mu} > 500\,\mathrm{GeV}$	0.04415	NLO	1.024 (NNLO)	~ 100k
$Z/\gamma \to \mu\mu$	POWHEG	$m_{\mu\mu} > 700\,\mathrm{GeV}$	0.01024	NLO	1.024 (NNLO)	~ 100k
$Z/\gamma \to \mu\mu$	POWHEG	$m_{\mu\mu} > 800\,\mathrm{GeV}$	0.005491	NLO	1.024 (NNLO)	~ 100k
$Z/\gamma \to \mu\mu$	POWHEG	$m_{\mu\mu} > 1000\,\mathrm{GeV}$	0.001796	NLO	1.024 (NNLO)	~ 100k
$Z/\gamma \to \mu\mu$	POWHEG	$m_{\mu\mu} > 1500\,\mathrm{GeV}$	0.0001705	NLO	1.024 (NNLO)	~ 100k
$Z/\gamma \to \mu\mu$	POWHEG	$m_{\mu\mu} > 2000\,\mathrm{GeV}$	0.00002208	NLO	1.024 (NNLO)	~ 100k
$Z/\gamma \to \tau\tau$	PYTHIA	$m_{\tau\tau} > 20\,\mathrm{GeV}$	1510	LO	1.268 (NNLO)	~ 19M
$Z/\gamma \to \tau\tau$	PYTHIA	$200 > m_{\tau\tau} > 100\,\mathrm{GeV}$	34.92	LO	1.268 (NNLO)	~ 2M
$Z/\gamma \to \tau\tau$	PYTHIA	$400 > m_{\tau\tau} > 200\,\mathrm{GeV}$	1.181	LO	1.268 (NNLO)	~ 1M
$Z/\gamma \to \tau\tau$	PYTHIA	$800 > m_{\tau\tau} > 400\,\mathrm{GeV}$	0.087	LO	1.268 (NNLO)	~ 1M
$Z/\gamma \to \tau\tau$	PYTHIA	$m_{\tau\tau} > 800\,\mathrm{GeV}$	0.0045	LO	1.268 (NNLO)	~ 1M
$t\bar{t}$	MC@NLO	no cuts	211.1	NLO	1.16 (NNLO)	~ 33M
$t \to b\ell\nu$ (s-Channel)	POWHEG	no cuts	2.82	NLO	1.38 (approx. NNLO)	~ 260k
$t \to b\ell\nu$ (t-Channel)	POWHEG	no cuts	47.0	NLO	1.18 (approx. NNLO)	~ 100k
$t \to b\ell\nu$ (tW-Channel DR)	POWHEG	no cuts	10.7	NLO	1.04 (approx. NNLO)	~ 500k
$\bar{t} \to b\ell\nu$ (s-Channel)	POWHEG	no cuts	1.57	NLO	1.12 (approx. NNLO)	~ 140k
$\bar{t} \to b\ell\nu$ (t-Channel)	POWHEG	no cuts	25.0	NLO	1.23 (approx. NNLO)	~ 2M
$\bar{t} \to b\ell\nu$ (tW-Channel DR)	POWHEG	no cuts	10.7	NLO	1.04 (approx. NNLO)	~ 500k
WW	PYTHIA	no cuts	33.6	LO	1.67 (NLO)	~ 10M
WZ	PYTHIA	no cuts	12.6	LO	2.56 (NLO)	~ 10M
ZZ	PYTHIA	co cuts	5.2	LO	1.59 (NLO)	~ 10M
WW	PYTHIA	$\hat{p}_T > 500\,\mathrm{GeV}$	0.005235	LO	1.67 (NLO)	~ 1M
WZ	PYTHIA	$\hat{p}_T > 500\,\mathrm{GeV}$	0.001695	LO	2.56 (NLO)	~ 1M
ZZ	PYTHIA	$\hat{p}_T > 500\,\mathrm{GeV}$	0.001065	LO	1.59 (NLO)	~ 1M
QCD μ enriched	PYTHIA	$\hat{p}_T > 20\,\mathrm{GeV}$, $p_T^\mu > 15\,\mathrm{GeV}$	134680	LO	-	~ 10M
QCD μ enriched	PYTHIA	$30 > \hat{p}_T > 20\,\mathrm{GeV}$, $p_T^\mu > 5\,\mathrm{GeV}$	1865500	LO	-	~ 10M
QCD μ enriched	PYTHIA	$50 > \hat{p}_T > 30\,\mathrm{GeV}$, $p_T^\mu > 5\,\mathrm{GeV}$	806298	LO	-	~ 10M
QCD μ enriched	PYTHIA	$80 > \hat{p}_T > 50\,\mathrm{GeV}$, $p_T^\mu > 5\,\mathrm{GeV}$	176188	LO	-	~ 10M
QCD μ enriched	PYTHIA	$120 > \hat{p}_T > 80\,\mathrm{GeV}$, $p_T^\mu > 5\,\mathrm{GeV}$	40448	LO	-	~ 10M
QCD μ enriched	PYTHIA	$170 > \hat{p}_T > 120\,\mathrm{GeV}$, $p_T^\mu > 5\,\mathrm{GeV}$	7463.9	LO	-	~ 8M
QCD μ enriched	PYTHIA	$300 > \hat{p}_T > 170\,\mathrm{GeV}$ $p_T^\mu > 5\,\mathrm{GeV}$	2299.8	LO	-	~ 8M
QCD μ enriched	PYTHIA	$470 > \hat{p}_T > 300\,\mathrm{GeV}$ $p_T^\mu > 5\,\mathrm{GeV}$	151.81	LO	-	~ 8M
QCD μ enriched	PYTHIA	$600 > \hat{p}_T > 470\,\mathrm{GeV}$, $p_T^\mu > 5\,\mathrm{GeV}$	11.796	LO	-	~ 4M
QCD μ enriched	PYTHIA	$800 > \hat{p}_T > 600\,\mathrm{GeV}$, $p_T^\mu > 5\,\mathrm{GeV}$	2.6902	LO	-	~ 4M
QCD μ enriched	PYTHIA	$1000 > \hat{p}_T > 800\,\mathrm{GeV}$, $p_T^\mu > 5\,\mathrm{GeV}$	0.3688	LO	-	~ 4M
QCD μ enriched	PYTHIA	$\hat{p}_T > 1000\,\mathrm{GeV}$, $p_T^\mu > 5\,\mathrm{GeV}$	0.0849	LO	-	~ 4M

Table A.3: Background samples used in the analysis (cont.). The order of the cross section is given in the fifth column. Multiplying the cross section with the k-factor corrects to the order given for the k-factor.

A.2.2 *Signal Monte Carlo*

Mass (GeV)	decay channels	LO cross section (pb^{-1})	NNLO k-factor	number of events
300	μ, τ	106.3	1.347	20 008
500	μ, τ	16.6	1.363	20 008
700	μ, τ	4.418	1.351	20 008
900	μ, τ	1.518	1.347	20 008
1100	μ, τ	$6.035 \cdot 10^{-1}$	1.331	20 008
1300	μ, τ	$2.632 \cdot 10^{-1}$	1.317	20 008
1500	μ, τ	$1.221 \cdot 10^{-1}$	1.293	20 008
1700	μ, τ	$5.928 \cdot 10^{-2}$	1.257	20 008
1900	μ, τ	$2.977 \cdot 10^{-2}$	1.230	20 008
2000	μ, τ	$2.132 \cdot 10^{-2}$	1.214	20 008
2100	μ, τ	$1.538 \cdot 10^{-2}$	1.199	20 008
2200	μ, τ	$1.116 \cdot 10^{-2}$	1.194	20 008
2300	μ, τ	$8.157 \cdot 10^{-3}$	1.172	20 008
2400	μ, τ	$6.001 \cdot 10^{-3}$	1.164	20 008
2500	μ, τ	$4.443 \cdot 10^{-3}$	1.140	20 008
2600	μ, τ	$3.323 \cdot 10^{-3}$	1.152	20 008
2700	μ, τ	$2.504 \cdot 10^{-3}$	1.153	20 008
2800	μ, τ	$1.905 \cdot 10^{-3}$	1.145	20 008
2900	μ, τ	$1.462 \cdot 10^{-3}$	1.148	20 008
3000	μ, τ	$1.135 \cdot 10^{-3}$	1.151	20 008
3100	μ	$8.899 \cdot 10^{-4}$	1.178	20 008
3200	μ, τ	$7.081 \cdot 10^{-4}$	1.187	20 008
3300	μ	$5.667 \cdot 10^{-4}$	1.207	20 008
3400	μ	$4.617 \cdot 10^{-4}$	1.220	20 008
3500	μ, τ	$3.796 \cdot 10^{-4}$	1.242	20 008
3700	μ	$2.657 \cdot 10^{-4}$	1.278	20 008
4000	μ, τ	$1.674 \cdot 10^{-4}$	1.331	20 008

Table A.4: W' signal samples used in the analysis, all were generated with PYTHIA.

Mass (GeV)	cross section $\left(\mathrm{pb}^{-1}\right)$	number of events
1	0.111	60 000
3	0.111	60 000
5	0.111	60 000
10	0.111	60 000
50	0.111	60 000
100	0.093	60 000
300	0.043	60 000
500	0.0166	60 000
1000	0.0010	60 000
1500	$3.425 \cdot 10^{-5}$	60 000
2000	$5.622 \cdot 10^{-7}$	60 000

(a) Axial-vector coupling

Mass (GeV)	cross section $\left(\mathrm{pb}^{-1}\right)$	number of event
1	0.111	60 000
3	0.111	60 000
5	0.111	60 000
10	0.107	60 000
50	0.111	60 000
100	0.107	60 000
300	0.071	60 000
500	0.037	60 000
1000	0.0042	60 000
1500	$2.26 \cdot 10^{-4}$	60 000
2000	$5.57 \cdot 10^{-6}$	60 000

(b) Vector coupling

Table A.5: Dark Matter signal samples used in the analysis, all were generated with MADGRAPH.

A.3 BACKGROUND FIT QUALITY

distribution	χ^2	χ^2/NDOF
final background	315.6	1.95
PDF up	472.8	2.92
PDF down	272.8	1.68
k-factor up	285.6	1.76
k-factor down	281.4	1.74
μ momentum scale up	276.3	1.71
μ momentum scale down	303.5	1.87
μ momentum resolution	333.7	2.06
pileup	280.7	1.73
Scale factor	321.5	1.98
Projection	325.6	2.01

distribution	χ^2	χ^2/NDOF
MET Jet energy scale up	241.6	1.49
MET Jet energy scale down	290.7	1.79
MET Jet energy resolution up	344.8	2.12
MET Jet energy resolution down	274.4	1.69
MET Electron energy scale up	247.7	1.53
MET Unclustered energy down	311.7	1.92
MET Tau energy scale up	244.2	1.51
MET Tau energy scale down	245.5	1.52
MET Unclustered energy up	249.0	1.54
MET Electron energy scale down	244.9	1.51

Table A.6: Background fit quality: The quality of the fit to the different systematic and final M_T distributions. The distribution, the χ^2 and the χ^2/NDOF is listed for every fit (the number of degrees of freedom for all fits is NDOF = 162).

A.4 CONVENTIONS AND UNITS

A.4.1 *Coordinate system*

The origin of the CMS coordinate system is the nominal collision point in the center of the experiment [10]. The y-axis is defined as pointing vertically upwards, and the x-axis is pointing radially inward toward the center of the LHC. The z-axis is therefore defined along the beam axis. In the x-y-plane, the radial coordinate r and the azimuthal angle ϕ (starting at the x-axis) is measured. The polar angle θ is measured in the y-z-plane from the z-axis. The polar angle is most of the times expressed via the pseudorapidity η which is defined as $\eta = -\ln\tan(\theta/2)$, because differences in η are Lorentz invariant.

A.4.2 *Conventions*

Definition of quantities used in this analysis:

- p_T
  p_T is the momentum perpendicular to the beam axis. It is defined by $p_T = p \cdot \sin\theta$.
- $\not{E}_T$
  The missing transverse energy $\not{E}_T$ (or E_T^{miss}) represents the vector sum of $\overrightarrow{E_T}$ of all not measured particles. The particles leave the detector, but the momentum and energy perpendicular to the beam axis must be zero, because it was zero before the collision. With the conservation of momentum it must be zero afterwards.
- M_T
  The transverse mass M_T is defined by

$$M_T = \sqrt{2 \cdot p_T \cdot \not{E}_T \cdot (1 - \cos\Delta\phi)} \tag{A.1}$$

  where $\Delta\phi$ is the azimuthal angle between p_T and $\not{E}_T$.

A.4.3 *Natural units*

Throughout this whole analysis, natural units in the sense that

$$\hbar = c = k_B = 1 \tag{A.2}$$

with the reduced Planck constant $\hbar$, the speed of light c and the Boltzmann constant k_B are used. With this convention, the relevant quantities for this analysis, momenta, masses and energies can all be expressed in eV.

A.5 ELECTRON SELECTION

The electron analysis is documented in detail in Ref. [60] and is based on the same principles as this analysis with the muon replaced by an electron. The most important difference is the electron selection, which is summarized in Tab. A.7.

In the electron channel the HEEP (High Energy Electron Pairs) selection v4.1 "light" [146] is used, which is optimized for the selection of high energy electrons by exploiting the shower

shape of the electromagnetic shower and information from the tracker. The quantity "ρ" is the average energy density in the event caused by pileup. It is used to subtract the energy deposited by PU in a isolation cone. The inner layer lost hits selection serves to reject photon conversions.

Quantity	HEEP v4.1	
	EB ($0 < \lvert\eta\rvert < 1.442$)	EE ($1.56 < \lvert\eta\rvert < 2.5$)
SC E_T	100 GeV	100 GeV
$\lvert\Delta\eta\rvert$	0.005	0.007
$\lvert\Delta\phi\rvert$	0.06	0.06
H/E	0.05	0.05
$\sigma_{i\eta i\eta}$	-	0.03
$E^{2\times5}/E^{5\times5}$	> 0.94 or $E^{1\times5}/E^{5\times5} > 0.83$	-
EM + Had Depth 1 Iso	$< \rho \cdot 0.28 + 2 + 0.03 \cdot E_T$	$< \rho \cdot 0.28 + 1 + 0.03 \cdot E_T$ ($p_T > 50$ GeV) $< \rho \cdot 0.28 + 2.5$ ($p_T < 50$ GeV)
Tracker Isolation	5 GeV	5 GeV
Inner layer lost hits	$\leqslant 1$	$\leqslant 1$
$\lvert d_{xy}\rvert$	< 0.02 cm	< 0.05 cm

Table A.7: HEEP selection

A.6 LIMIT RECALCULATION

The limits from other experiments that are shown for comparison are all determined for $\xi = +1$ and need to be recalculated for $\xi = 0, -1$ for a complete comparison. This recalculation is explained in the following sections for the mono-jet and direct detection limits.

A.6.1 *Mono-jet limit*

The mono-jet Dark Matter-Nucleon cross section limit can be calculated from the proton-proton cross section limit. As there is no interference in the mono-jet channel, the proton-proton cross section limit is the same for $\xi = +1$ and $\xi = -1$ and a factor two weaker for $\xi = 0$, because only half of the initial quarks participate in the reaction.

A.6.2 *Direct detection limit*

For direct detection experiments the measured spin independent Dark Matter-Nucleon cross section depends on the detector material is given by

$$\sigma_N^{SI}(\xi) = \frac{\mu^2}{\pi\Lambda^4}\left(Z \cdot \lambda_p + (A - Z)\,\lambda_n\right)^2 \tag{A.3}$$

with the reduced mass of the Dark Matter-Nucleon system μ, the interaction scale Λ and the structure functions for the proton and neutron $\lambda_{p,n}$ [138]. This formula can be used to recalculated the Dark Matter-Nucleon cross section to a Dark Matter-proton cross section

(which is identical to the Dark Matter-neutron cross section for $\xi = +1$) which is independent of the material.

The basic assumption for direct detection limits is

$$\frac{\sigma_p^{theo}(\xi)}{\sigma_N^{theo}(\xi)} = \frac{\sigma_p^{obs}(\xi)}{\sigma_N^{obs}} \Rightarrow \sigma_N^{obs} \cdot \frac{\sigma_p^{theo}(\xi)}{\sigma_N^{theo}(\xi)} = \sigma_p^{obs}(\xi) \tag{A.4}$$

with the cross section expected from the theory σ^{theo} and the observed cross sections σ^{obs} for a Dark Matter-Nucleon interaction σ_N and for a Dark Matter-proton interaction σ_p. Eqn. A.4 can be used to translate the observed Dark Matter-Nucleon cross section into a observed Dark Matter-proton cross section. The ratio of Eqn. A.4 calculated for $\xi \neq +1$ and $\xi = +1$ gives the correction factor

$$\frac{\sigma_p(\xi \neq +1)}{\sigma_p(\xi = +1)} = C = \frac{\sigma_N^{theo}(\xi = +1)}{\sigma_p^{theo}(\xi = +1)} \cdot \frac{\sigma_p^{theo}(\xi \neq +1)}{\sigma_N^{theo}(\xi \neq +1)} \tag{A.5}$$

with the formula for the spin independent nucleon cross section of Eqn. A.3 follows the correction factor. All terms $\frac{\mu^2}{\pi\Lambda^4}$ cancel and only the ratio

$$C^{SI} = \left(\frac{Z \cdot \lambda_p^{\xi=+1} + (A-Z)\lambda_n^{\xi=+1}}{\lambda_p^{\xi=+1}} \cdot \frac{\lambda_p^{\xi\neq+1}}{Z \cdot \lambda_p^{\xi\neq+1} + (A-Z)\lambda_n^{\xi\neq+1}} \right)^2 \tag{A.6}$$

remains. This equation can be solved with $\lambda_N = \sum_q \xi_q f_q^N$, the structure coefficients f_q^N ($f_u^p = f_d^n = 2$, $f_d^p = f_u^n = 1$ and $f = 0$ for other quarks) and the interference parameter ξ_q, which is equal to ξ for $q = d$ and equal to 1 for all other quarks. This results in the correction factor for $\xi = +1 \longrightarrow \xi = 0$ and for $\xi = +1 \longrightarrow \xi = -1$:

$$C_{\xi=0}^{SI} = \left(\frac{2 \cdot A}{Z + A} \right)^2 \text{ and } C_{\xi=-1}^{SI} = \left(\frac{A}{2 \cdot Z - A} \right)^2 \tag{A.7}$$

A similar calculation for the spin dependent cross section can be done,

$$\sigma_N^{SD}(\xi) = \frac{4\mu^2}{\pi\Lambda^4} \cdot \frac{J_A + 1}{J_A} \left(\Delta_p S_p^A + \Delta_n S_n^A \right)^2 \tag{A.8}$$

with the angular momentum J_A of the nucleon A and the spin expectation values $S_{p,n}^A$ for a nucleus A for the proton and neutron. The resulting correction factors are

$$C_{\xi=0}^{SD} = \left(\frac{0.757 \cdot \left(S_p^A + S_n^A\right)}{0.7575 \cdot S_p^A - 0.512 \cdot S_n^A} \right)^2 \text{ and } C_{\xi=-1}^{SD} = \left(\frac{1.184 \cdot \left(S_p^A + S_n^A\right)}{1.184 \cdot S_p^A - 1.354 \cdot S_n^A} \right)^2 \tag{A.9}$$

For the direct detection experiments the detector material is not exactly one element or one isotope, therefore A and Z (or S_p^A and S_n^A) have to be calculated as weighted means of the material mixture.

A.7 CUTFLOW

Sample	Trigger	High p_T muon ID	Single μ	$p_T/\not{E}_T$	$\Delta\phi$	$p_T > 110\,\text{GeV}$
$W \to \mu\nu$	$2.28 \cdot 10^7$	$9.66 \cdot 10^6$	$1.86 \cdot 10^6$	$1.55 \cdot 10^6$	$1.24 \cdot 10^6$	$1.74 \cdot 10^4$
$W \to \tau\nu$	$3.11 \cdot 10^5$	$1.61 \cdot 10^5$	$1.20 \cdot 10^4$	$1.09 \cdot 10^4$	$9.26 \cdot 10^3$	326
QCD	$5.77 \cdot 10^7$	$2.09 \cdot 10^6$	$2.13 \cdot 10^4$	$1.14 \cdot 10^4$	$8.25 \cdot 10^3$	87.8
Top	$1.28 \cdot 10^5$	$9.03 \cdot 10^4$	$8.61 \cdot 10^4$	$6.45 \cdot 10^4$	$2.75 \cdot 10^4$	$2.76 \cdot 10^3$
DY	$8.34 \cdot 10^6$	$5.01 \cdot 10^6$	$8.79 \cdot 10^4$	$5.68 \cdot 10^4$	$4.74 \cdot 10^4$	237
Diboson	$1.24 \cdot 10^5$	$9.19 \cdot 10^4$	$1.65 \cdot 10^4$	$1.21 \cdot 10^4$	$8.46 \cdot 10^3$	651
data	$6.87 \cdot 10^7$	$2.03 \cdot 10^7$	$2.49 \cdot 10^6$	$1.99 \cdot 10^6$	$1.57 \cdot 10^6$	$2.26 \cdot 10^4$
W'	410	387	370	351	347	339
DM	$2.41 \cdot 10^4$	$2.07 \cdot 10^4$	$1.71 \cdot 10^4$	$1.46 \cdot 10^4$	$1.22 \cdot 10^4$	$5.63 \cdot 10^3$

Table A.8: Cutflow of Fig. 5.1a as table.

A.8 EFFECT OF $\not{E}_T$ CORRECTIONS

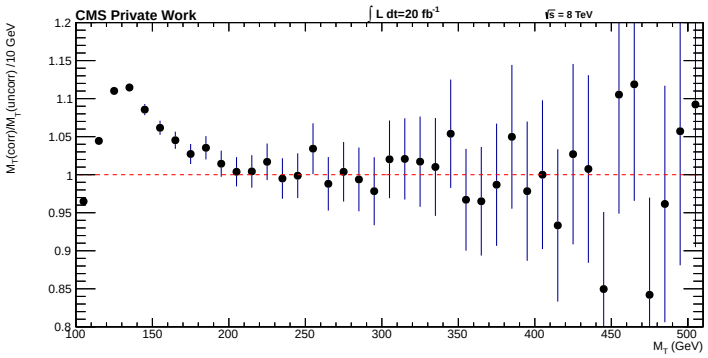

Figure A.3: Ratio of M_T calculated with the corrected $\not{E}_T$ and calculated with uncorrected $\not{E}_T$ for data events.

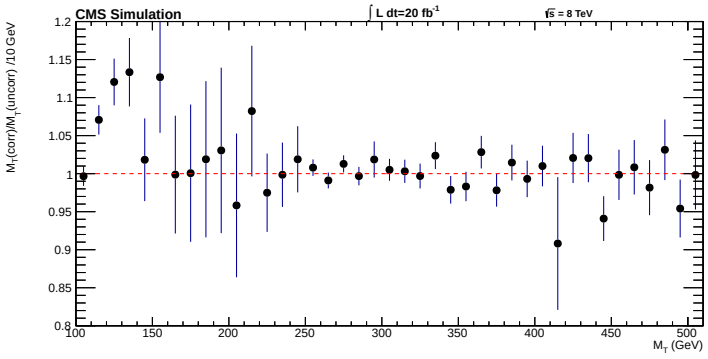

Figure A.4: Ratio of M_T calculated with the corrected $\not{E}_T$ and calculated with uncorrected $\not{E}_T$ for all Monte Carlo events.

a.9 CONTROL PLOTS

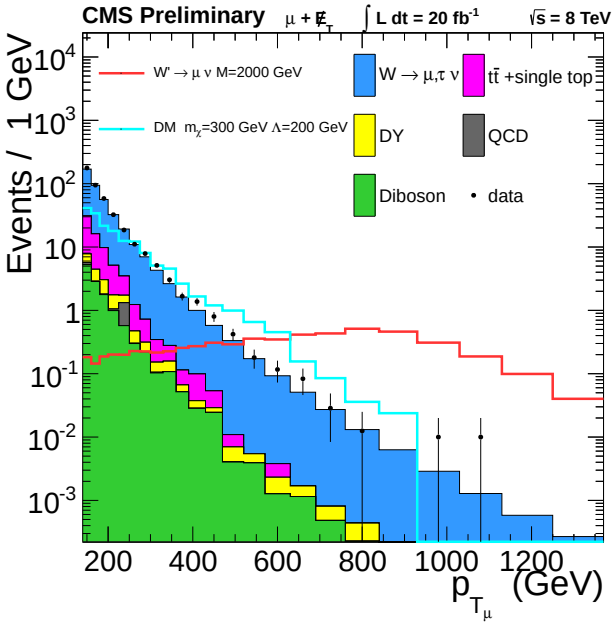

(a) Distribution of the muon p_T, for all events that are in the final M_T distribution. The same binning as for the M_T distribution is used, and corresponds to the muon p_T resolution of ~ 10 %.

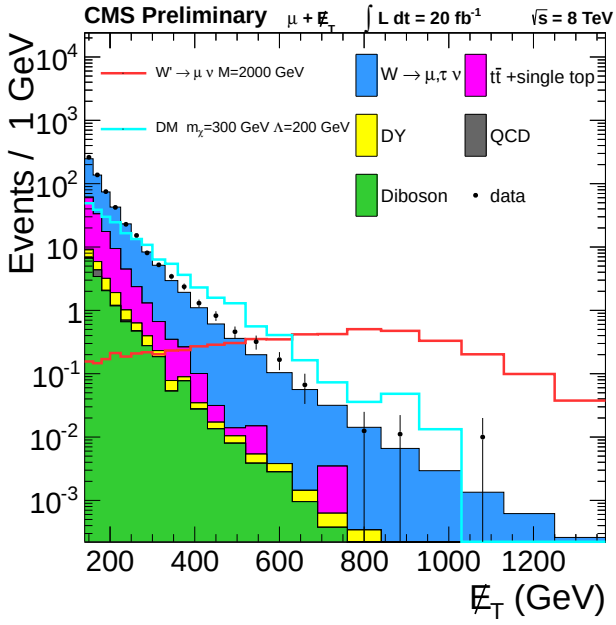

(b) Distribution of $\not{E}_T$ for all events, that end up in the final M_T distribution. The binning is the same as for the muon p_T, because the $\not{E}_T$ resolution is mainly driven by the muon p_T resolution.

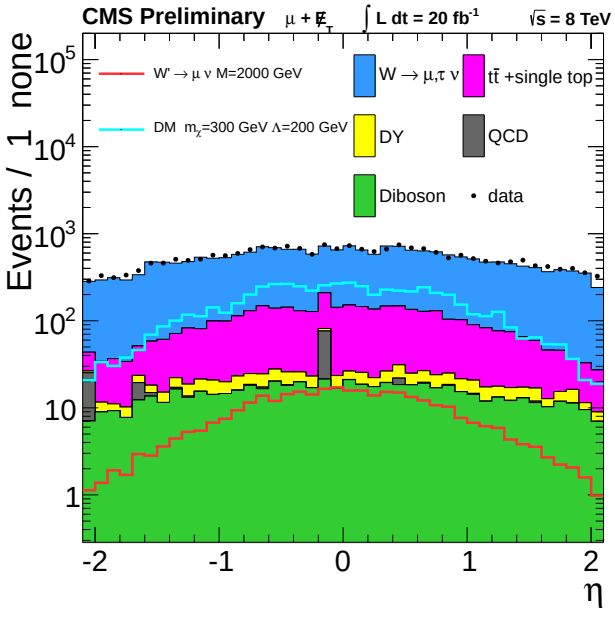

(c) Distribution of the pseudorapidity η for all muons, that end up in the final M_T distribution. The whole acceptance region $-2.1 < \eta < 2.1$ is shown.

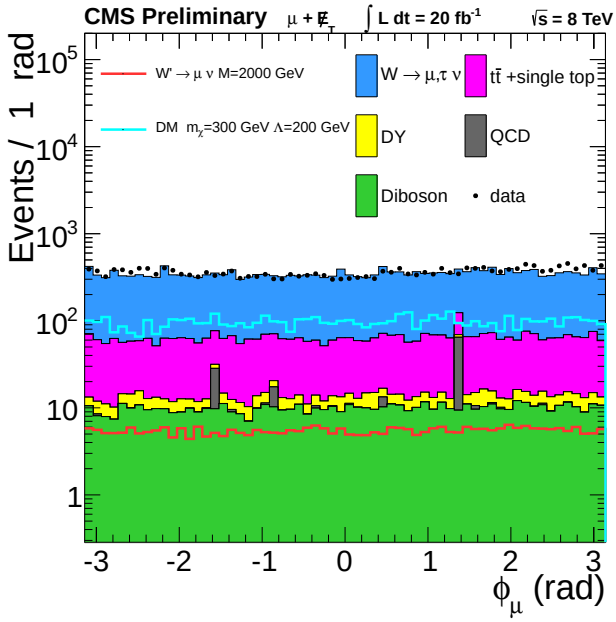

(d) The ϕ distribution for all muons, that end up in the final M_T distribution is shown.

Figure A.5: Control Plots for events from the whole M_T spectrum. Systematic uncertainties are not shown for the plots.

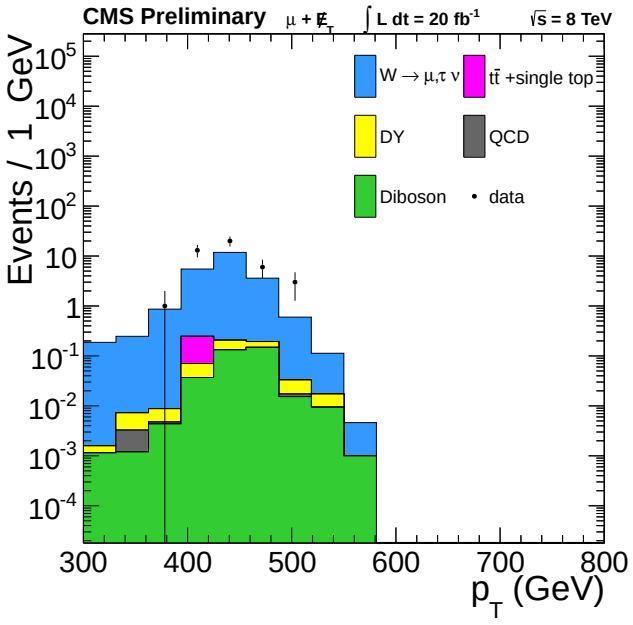

(a) Distribution of the p_T of the muon.

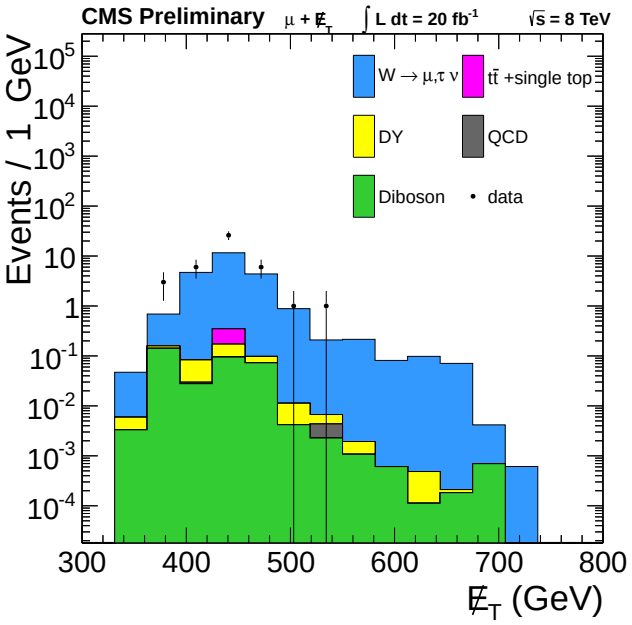

(b) $\not{E}_T$ distribution

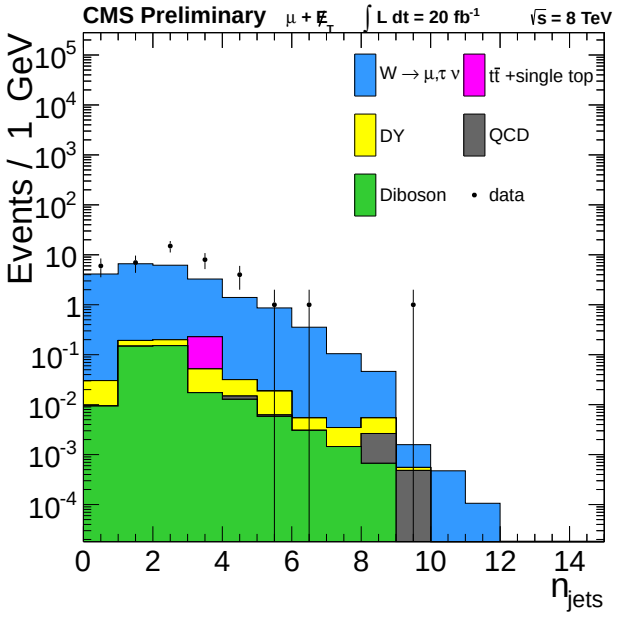

(c) The distribution of the number of jets in the events.

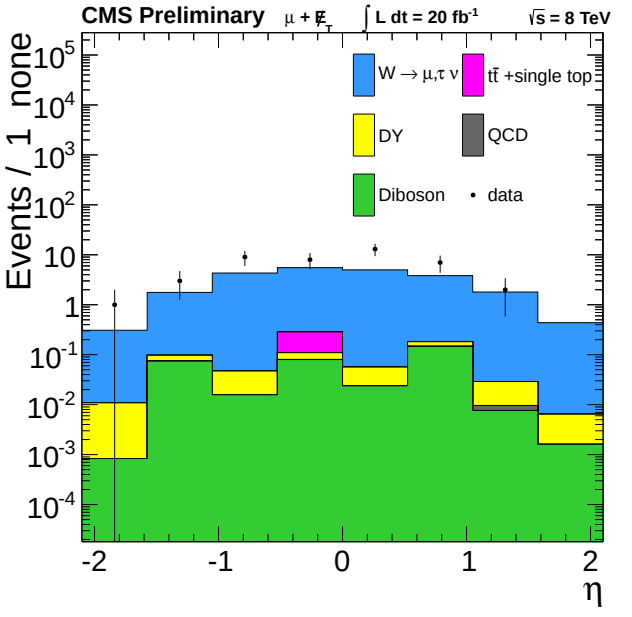

(d) η distribution of the muon.

Figure A.6: Control Plots for events in the range $840 < M_T < 920\,\text{GeV}$, the M_T region with the biggest data/Monte Carlo deviation. Systematic uncertainties are not shown for this distributions.

BIBLIOGRAPHY

[1] CDF Collaboration. Search for a New Heavy Gauge Boson W′ with Electron + missing E_T Event Signature in $p\bar{p}$ collisions at $\sqrt{s}$=1.96 TeV (2010). URL http://arxiv.org/abs/1012.5145. Submitted to *Phys. Rev. Lett.* (Cited on pages 1 and 20.)

[2] Abazov, V. M. *et al.* Search for W′ bosons decaying to an electron and a neutrino with the Do detector. *Phys. Rev. Lett.* **100**, 031804 (2008). URL http://arxiv.org/abs/0710.2966. (Cited on pages 1 and 20.)

[3] CMS Collaboration. Search for a heavy gauge boson W' in the final state with an electron and large missing transverse energy in pp collisions at $\sqrt{s} = 7$ TeV. *Phys.Lett.* **B698**, 21–39 (2011). URL http://arxiv.org/abs/1012.5945. (Cited on page 1.)

[4] CMS Collaboration. Search for a W' boson decaying to a muon and a neutrino in pp collisions at $\sqrt{s} = 7$ TeV. *Phys.Lett.* **B701**, 160–179 (2011). URL http://arxiv.org/abs/1103.0030. (Cited on page 1.)

[5] CMS Collaboration. Search for leptonic decays of W' bosons in pp collisions at $\sqrt{s} = 7$ TeV. *JHEP* **1208**, 023 (2012). URL http://arxiv.org/abs/1204.4764. (Cited on pages 1 and 68.)

[6] CMS Collaboration. Search for leptonic decays of W′ bosons in pp collisions at sqrt(s)=8 TeV. *CMS Physics Analysis Summary* **EXO-12-060** (2013). URL http://cds.cern.ch/record/1522476?ln=de. (Cited on pages 1 and 79.)

[7] CMS Collaboration. Search for dark matter in the mono-lepton channel with pp collision events at center-of-mass energy of 8 TeV . *CMS Physics Analysis Summary* **EXO-13-004** (2013). URL http://cds.cern.ch/record/1563245?ln=de. (Cited on pages 1 and 79.)

[8] Evans, L. & Bryant, P. LHC Machine. *Journal of Instrumentation* **3**, S08001 (2008). URL http://stacks.iop.org/1748-0221/3/i=08/a=S08001. (Cited on page 2.)

[9] Lefèvre, C. The CERN accelerator complex. Complexe des accélérateurs du CERN (2008). URL http://cds.cern.ch/record/1260465?ln=en. (Cited on page 2.)

[10] CMS Collaboration. The CMS experiment at the CERN LHC. *Journal of Instrumentation* **3**, S08004 (2008). URL http://stacks.iop.org/1748-0221/3/i=08/a=S08004. (Cited on pages 3, 4, 6, and 88.)

[11] CMS Collaboration. The performance of the CMS muon detector in proton-proton collisions at $\sqrt{s}$ = 7 TeV at the LHC. *CMS Physics Analysis Summary* **MUO-11-001** (2013). (Cited on pages 5, 7, and 29.)

[12] Bird, I. *et al.* LHC computing Grid. Technical design report (2005). (Cited on page 8.)

[13] Griffiths, D. *Introduction to Elementary Particles*. Physics textbook (Wiley, 2008). URL http://books.google.de/books?id=w9Dz56myXm8C. (Cited on page 9.)

[14] Langacker, P. Structure of the standard model (1995). URL http://arxiv.org/abs/hep-ph/0304186. (Cited on page 9.)

[15] Halzen, F. & Martin, A. *Quarks and leptons: an introductory course in modern particle physics* (Wiley, 1984). URL http://books.google.de/books?id=zwDvAAAAMAAJ. (Cited on page 9.)

[16] Weinberg, S. What is quantum field theory, and what did we think it is? (1996). URL http://arxiv.org/abs/hep-th/9702027. (Cited on page 9.)

[17] Weinberg, S. A model of leptons. *Phys. Rev. Lett.* **19**, 1264–1266 (1967). URL http://link.aps.org/doi/10.1103/PhysRevLett.19.1264. (Cited on page 9.)

[18] Salam, A. Weak and electromagnetic interactions. In Svartholm, N. (ed.) *Elementary particle theory*, 367–377 (Almquist & Wiksell). (Cited on page 9.)

[19] Pati, J. C. & Salam, A. Lepton number as the fourth 'color'. *Phys. Rev.* **D10**, 275 (1974). (Cited on page 9.)

[20] Glashow, S. L. Partial-symmetries of weak interactions. *Nuclear Physics* **22**, 579 – 588 (1961). URL http://www.sciencedirect.com/science/article/pii/0029558261904692. (Cited on page 9.)

[21] Higgs, P. W. Broken symmetries, massless particles and gauge fields. *Phys.Lett.* **12**, 132–133 (1964). (Cited on page 10.)

[22] Higgs, P. W. Broken Symmetries and the Masses of Gauge Bosons. *Phys.Rev.Lett.* **13**, 508–509 (1964). (Cited on page 10.)

[23] Higgs, P. W. Spontaneous symmetry breakdown without massless bosons. *Phys. Rev.* **145**, 1156–1163 (1966). URL http://link.aps.org/doi/10.1103/PhysRev.145.1156. (Cited on page 10.)

[24] Englert, F. & Brout, R. Broken Symmetry and the Mass of Gauge Vector Mesons. *Phys.Rev.Lett.* **13**, 321–323 (1964). (Cited on page 10.)

[25] Guralnik, G., Hagen, C. & Kibble, T. Global Conservation Laws and Massless Particles. *Phys.Rev.Lett.* **13**, 585–587 (1964). (Cited on page 10.)

[26] Kibble, T. W. B. Symmetry breaking in non-abelian gauge theories. *Phys. Rev.* **155**, 1554–1561 (1967). URL http://link.aps.org/doi/10.1103/PhysRev.155.1554. (Cited on page 10.)

[27] CMS Collaboration. Observation of a new boson at a mass of 125 GeV with the CMS experiment at the LHC. *Phys.Lett.* **B716**, 30–61 (2012). URL http://arxiv.org/abs/1207.7235. (Cited on page 10.)

[28] CMS Collaboration. Combination of standard model Higgs boson searches and measurements of the properties of the new boson with a mass near 125 GeV. *CMS Physics Analysis Summary* **HIG-13-005** (2013). URL http://cds.cern.ch/record/1542387?ln=en. (Cited on page 10.)

[29] Standard model of elementary particles (2013). URL http://en.wikipedia.org/wiki/File:Standard_Model_of_Elementary_Particles.svg. (Cited on page 10.)

[30] Baak, M. *et al.* The Electroweak Fit of the Standard Model after the Discovery of a New Boson at the LHC. *Eur.Phys.J.* **C72**, 2205 (2012). URL http://arxiv.org/abs/1209.2716. (Cited on pages 11 and 12.)

[31] J. Stirling. MSTW PDFs: key plots URL http://mstwpdf.hepforge.org/plots/plots.html. (Cited on page 12.)

[32] Kibble, T. W. B. Englert-Brout-Higgs-Guralnik-Hagen-Kibble mechanism. *Scholarpedia* **4**, 6441 (2009). URL http://www.scholarpedia.org/article/Englert-Brout-Higgs-Guralnik-Hagen-Kibble_mechanism. (Cited on page 13.)

[33] Particle Data Group. Review of Particle Physics (RPP). *Phys.Rev.* **D86**, 010001 (2012). (Cited on pages 14, 22, and 38.)

[34] Placakyte, R. Parton Distribution Functions (2011). URL http://arxiv.org/abs/1111.5452. (Cited on page 15.)

[35] Altarelli, G. QCD evolution equations for parton densities **4**, 7124 (2009). URL http://www.scholarpedia.org/article/QCD_evolution_equations_for_parton_densities. (Cited on page 15.)

[36] Martin, A., Stirling, W., Thorne, R. & Watt, G. Parton distributions for the LHC. *Eur.Phys.J.* **C63**, 189–285 (2009). URL http://arxiv.org/abs/0901.0002. (Cited on page 15.)

[37] Martin, A., Stirling, W., Thorne, R. & Watt, G. Uncertainties on alpha(S) in global PDF analyses and implications for predicted hadronic cross sections. *Eur.Phys.J.* **C64**, 653–680 (2009). URL http://arxiv.org/abs/0905.3531. (Cited on page 15.)

[38] Lai, H.-L. *et al.* New parton distributions for collider physics. *Phys.Rev.* **D82**, 074024 (2010). URL http://arxiv.org/abs/1007.2241. (Cited on page 15.)

[39] Pumplin, J. *et al.* New generation of parton distributions with uncertainties from global QCD analysis. *JHEP* **07**, 012 (2002). URL http://arxiv.org/abs/hep-ph/0201195. (Cited on page 15.)

[40] Ball, R. D. *et al.* Parton distributions with LHC data. *Nucl.Phys.* **B867**, 244–289 (2013). URL http://arxiv.org/abs/1207.1303. (Cited on page 15.)

[41] The Les Houches Accord PDF Interface URL http://projects.hepforge.org/lhapdf/. (Cited on page 15.)

[42] CMS Collaboration. Inclusive W/Z cross section at 8 TeV. *CMS Physics Analysis Summary* **SMP-12-011** (2012). URL http://cds.cern.ch/record/1460098?ln=en. (Cited on page 15.)

[43] Ellis, J., Espinosa, J., Giudice, G., Hoecker, A. & Riotto, A. The Probable Fate of the Standard Model. *Phys.Lett.* **B679**, 369–375 (2009). URL http://arxiv.org/abs/0906.0954. (Cited on page 17.)

[44] Degrassi, G. *et al.* Higgs mass and vacuum stability in the Standard Model at NNLO. *JHEP* **1208**, 098 (2012). URL http://arxiv.org/abs/1205.6497. (Cited on page 17.)

[45] Ade, P. *et al.* Planck 2013 results. XXII. Constraints on inflation (2013). URL http://arxiv.org/abs/1303.5082. (Cited on page 17.)

[46] Farrar, G. R. & Shaposhnikov, M. E. Baryon asymmetry of the universe in the standard model. *Phys. Rev. D* **50**, 774–818 (1994). URL http://link.aps.org/doi/10.1103/PhysRevD.50.774. (Cited on page 17.)

[47] Ade, P. *et al.* Planck 2013 results. XVI. Cosmological parameters (2013). URL http://arxiv.org/abs/1303.5076. (Cited on pages 17, 18, and 78.)

[48] Peebles, P. & Ratra, B. The Cosmological constant and dark energy. *Rev.Mod.Phys.* **75**, 559–606 (2003). URL http://arxiv.org/abs/astro-ph/0207347. (Cited on page 17.)

[49] Bertone, G., Hooper, D. & Silk, J. Particle dark matter: Evidence, candidates and constraints. *Phys.Rept.* **405**, 279–390 (2005). URL http://arxiv.org/abs/hep-ph/0404175. (Cited on page 17.)

[50] Begeman, K., Broeils, A. & Sanders, R. Extended rotation curves of spiral galaxies: Dark haloes and modified dynamics. *Mon.Not.Roy.Astron.Soc.* **249**, 523 (1991). (Cited on page 18.)

[51] Clowe, D. *et al.* A direct empirical proof of the existence of dark matter. *The Astrophysical Journal Letters* **648**, L109 (2006). URL http://stacks.iop.org/1538-4357/648/i=2/a=L109. (Cited on page 18.)

[52] Kamionkowski, M. WIMP and axion dark matter (1997). URL http://arxiv.org/abs/hep-ph/9710467. (Cited on page 19.)

[53] Jungman, G., Kamionkowski, M. & Griest, K. Supersymmetric dark matter. *Physics Reports* **267**, 195 – 373 (1996). URL http://www.sciencedirect.com/science/article/pii/0370157395000585. (Cited on pages 19 and 21.)

[54] Mohapatra, R. N. & Pati, J. C. Left-right gauge symmetry and an "isoconjugate" model of CP violation. *Phys. Rev. D* **11**, 566–571 (1975). URL http://link.aps.org/doi/10.1103/PhysRevD.11.566. (Cited on page 19.)

[55] Schmaltz, M. & Tucker-Smith, D. Little Higgs review. *Ann.Rev.Nucl.Part.Sci.* **55**, 229–270 (2005). URL http://arxiv.org/abs/hep-ph/0502182. (Cited on page 19.)

[56] Georgi, H. & Glashow, S. L. Unity of all elementary-particle forces. *Phys. Rev. Lett.* **32**, 438–441 (1974). URL http://link.aps.org/doi/10.1103/PhysRevLett.32.438. (Cited on page 19.)

[57] Altarelli, G., Mele, B. & Ruiz-Altaba, M. Searching for new heavy vector bosons in $p\bar{p}$ colliders. *Z. Phys.* **C45**, 109 (1989). (Cited on page 19.)

[58] CMS Collaboration. Search for a W' boson decaying to a muon and a neutrino in pp collisions at $\sqrt{s} = 7$ TeV. *Phys.Lett.* **B701**, 160–179 (2011). URL http://arxiv.org/abs/1103.0030. (Cited on pages 20 and 71.)

[59] Aad, G. *et al.* Search for a heavy gauge boson decaying to a charged lepton and a neutrino in 1 fb-1 of pp collisions at sqrt(s) = 7 TeV using the ATLAS detector. *Phys. Lett.* **B705**, 28–46 (2011). URL http://arxiv.org/abs/1108.1316. (Cited on page 20.)

[60] Millet, P. *Search for new physics in pp collision events with one electron and missing transverse energy using CMS data*. Master's thesis, RWTH Aachen (2013). (Cited on pages 20, 69, 70, and 88.)

[61] Goodman, J. *et al.* Constraints on Light Majorana dark Matter from Colliders. *Phys.Lett.* **B695**, 185–188 (2011). URL http://arxiv.org/abs/1005.1286. (Cited on page 20.)

[62] Goodman, J. *et al.* Constraints on Dark Matter from Colliders. *Phys.Rev.* **D82**, 116010 (2010). URL http://arxiv.org/abs/1008.1783. (Cited on page 20.)

[63] Beltran, M., Hooper, D., Kolb, E. W. & Krusberg, Z. C. Deducing the nature of dark matter from direct and indirect detection experiments in the absence of collider signatures of new physics. *Phys.Rev.* **D80**, 043509 (2009). URL http://arxiv.org/abs/0808.3384. (Cited on pages 20 and 77.)

[64] Servant, G. & Tait, T. M. Is the lightest Kaluza-Klein particle a viable dark matter candidate? *Nucl.Phys.* **B650**, 391–419 (2003). URL http://arxiv.org/abs/hep-ph/0206071. (Cited on page 21.)

[65] Particle Data Group. Review of Particle Physics (RPP). *Phys.Rev.* **D86**, 010001 (2012). Chap. 24. (Cited on page 21.)

[66] CMS Collaboration. Search for new physics in monojet events in pp collisions at sqrt(s)= 8 TeV. *CMS Physics Analysis Summary* **EXO-12-048** (2013). (Cited on pages 22 and 75.)

[67] Chatrchyan, S. *et al.* Search for Dark Matter and Large Extra Dimensions in pp Collisions Yielding a Photon and Missing Transverse Energy. *Phys.Rev.Lett.* **108**, 261803 (2012). URL http://arxiv.org/abs/1204.0821. (Cited on page 22.)

[68] CMS Collaboration. Muon Reconstruction in the CMS Detector. *CMS Analysis Note* **AN-08-097** (2009). (Cited on pages 25 and 27.)

[69] CMS Collaboration. Design and Implementation of the Muon High-Level Trigger in CMS. *CMS Physics Analysis Summary* **MUO-10-003** (2011). (Cited on page 25.)

[70] Fruhwirth, R. Application of Kalman filtering to track and vertex fitting. *Nucl.Instrum.Meth.* **A262**, 444–450 (1987). (Cited on page 25.)

[71] CMS Collaboration. *CMS TriDAS project: Technical Design Report, Volume 1: The Trigger Systems*. No. CERN/LHCC 2000-38 in Technical Design Report CMS. (Cited on page 26.)

[72] CMS Collaboration. Search for New High-Mass Resonances Decaying to Muon Pairs in the CMS Experiment. *CMS Analysis Note* **AN-07-038** (2008). (Cited on page 27.)

[73] Tucker, J. Tracker-plus-first-muon-station (TPFMS) reconstructor and the TMR cocktail. *Talk from May 6, 2010* URL https://indico.cern.ch/subContributionDisplay.py?subContId=3&contribId=0&confId=93943. (Cited on page 27.)

[74] Traczyk, P. TeV Muons & Picky Muon Reco. *Talk from May 6, 2010* URL https://indico.cern.ch/subContributionDisplay.py?subContId=2&contribId=0&confId=93943. (Cited on page 27.)

[75] Traczyk, P. & CMS Collaboration - MuonPOG . Muon object review. *Talk from November 28, 2012* URL https://indico.cern.ch/getFile.py/access?contribId=6&resId=0&materialId=slides&confId=172473. (Cited on page 27.)

[76] CMS Collaboration. Performance of CMS muon reconstruction in pp collision events at $\sqrt{s} = 7$ TeV. *Journal of Instrumentation* **7**, P10002 (2012). URL http://stacks.iop.org/1748-0221/7/i=10/a=P10002. (Cited on pages 28 and 29.)

[77] CMS Collaboration - MuonPOG . Baseline muon selections. *TWiki* (2013). URL https://twiki.cern.ch/twiki/bin/view/CMSPublic/SWGuideMuonId. (Cited on page 28.)

[78] Lohse, T. Vertex Reconstruction And Fitting. *Hera-B Notes* **95-013** (1995). (Cited on page 30.)

[79] CMS Collaboration. Missing transverse energy performance of the CMS detector. *Journal of Instrumentation* **6**, 9001 (2011). URL http://arxiv.org/abs/1106.5048. (Cited on page 31.)

[80] CMS Collaboration. Particle-Flow Event Reconstruction in CMS and Performance for Jets, Taus, and MET. *CMS Physics Analysis Summary* **PFT-09-001** (2009). (Cited on page 31.)

[81] CMS Collaboration - JetMET Group. Formulae for pfMET Type-I and Type-II Corrections. *TWiki* (2013). URL https://twiki.cern.ch/twiki/bin/viewauth/CMS/METType1Type2Formulae. (Cited on page 31.)

[82] CMS Collaboration - JetMET Group. Met optional filters. *TWiki* (2013). URL https://twiki.cern.ch/twiki/bin/viewauth/CMS/MissingETOptionalFilters. (Cited on page 31.)

[83] CMS Collaboration. Fake missing transverse momentum in the 2012 dataset. *CMS Analysis Note* **AN-12/268** (2013). (Cited on page 31.)

[84] CMS Collaboration - SUSY + JetMETGroup. Beam Halo Id in CMS. *TWiki* (2011). URL https://twiki.cern.ch/twiki/bin/viewauth/CMS/BeamHaloId. (Cited on page 31.)

[85] CMS Collaboration. Identification and filtering of uncharacteristic noise in the cms hadron calorimeter. *Journal of Instrumentation* **5**, To3014 (2010). URL http://stacks.iop.org/1748-0221/5/i=03/a=T03014. (Cited on page 31.)

[86] Temple, J. Hcal Laser Events in 2012 Data. *Talk from October 24, 2012* URL https://indico.cern.ch/getFile.py/access?contribId=1&resId=0&materialId=slides&confId=169318. (Cited on page 31.)

[87] CMS Collaboration - SUSY Group. ECAL Maksed Cell Issue Summary for SUSY Analyses. *TWiki* (2011). URL https://twiki.cern.ch/twiki/bin/view/CMS/SusyEcalMaskedCellSummary. (Cited on page 32.)

[88] CMS Collaboration - SUSY Group. SUSY RA2/Tracking failure. *TWiki* (2011). URL https://twiki.cern.ch/twiki/bin/view/CMS/SusyRA2NJetsInData2010#Tracking_failure. (Cited on page 32.)

[89] CMS Collaboration - TrackingPOG . Tracking POG/Filters. *TWiki* (2012). URL https://twiki.cern.ch/twiki/bin/view/CMS/TrackingPOGFilters#Filters. (Cited on page 32.)

[90] CMS Collaboration. Plans for Jet Energy Corrections at CMS. *CMS Physics Analysis Summary* **JME-07-002** (2008). (Cited on page 33.)

[91] CMS Collaboration. Plans for Jet Energy Corrections at CMS. *CMS Analysis Note* **AN-07-055** (2008). (Cited on page 33.)

[92] Veelken, C. Systematic MET Shift/ phi-Asymmetry. *Talk from April 02, 2012* URL https://indico.cern.ch/getFile.py/access?contribId=1&resId=0&materialId=slides&confId=174318. (Cited on page 33.)

[93] CMS Collaboration. Study of MET Performanca in events containing one Z boson decaying into two muons in 2012 Data. *CMS Analysis Note* **AN-12-333** (2013). (Cited on page 33.)

[94] CMS Collaboration. MET performance in 8 TeV data. *CMS Physics Analysis Summary* **JME-12-002** (2013). (Cited on page 33.)

[95] Tuura, L., Meyer, A., Segoni, I. & Ricca, G. D. Cms data quality monitoring: Systems and experiences. *Journal of Physics: Conference Series* **219**, 072020 (2010). URL http://stacks.iop.org/1742-6596/219/i=7/a=072020. (Cited on page 37.)

[96] Agostinelli, S. *et al.* GEANT4: A simulation toolkit. *Nucl. Instrum. Meth.* **A506**, 250–303 (2003). (Cited on page 37.)

[97] Allison, J. *et al.* Geant4 developments and applications. *IEEE Trans. Nucl. Sci.* **53**, 270 (2006). (Cited on page 37.)

[98] Sjöstrand, T., Mrenna, S. & Skands, P. Z. PYTHIA 6.4 Physics and Manual. *JHEP* **05**, 026 (2006). URL http://arxiv.org/abs/hep-ph/0603175. (Cited on page 38.)

[99] Alwall, J. *et al.* MadGraph/MadEvent v4: the new web generation. *JHEP* **09**, 028 (2007). (Cited on page 38.)

[100] Alioli, S., Nason, P., Oleari, C. & Re, E. A general framework for implementing NLO calculations in shower Monte Carlo programs: the POWHEG BOX. *JHEP* **1006**, 043 (2010). URL http://arxiv.org/abs/arXiv:1002.2581. (Cited on page 38.)

[101] Frixione, S., Nason, P. & Oleari, C. Matching NLO QCD computations with Parton Shower simulations: the POWHEG method. *JHEP* **0711**, 070 (2007). URL http://arxiv.org/abs/arXiv:0709.2092. (Cited on page 38.)

[102] Nason, P. A new method for combining NLO QCD with shower Monte Carlo algorithms. *JHEP* **11**, 040 (2004). URL http://arxiv.org/abs/hep-ph/0409146. (Cited on page 38.)

[103] Kidonakis, N. Differential and total cross sections for top pair and single top production (2012). URL http://arxiv.org/abs/1205.3453. (Cited on page 39.)

[104] Frixione, S. & Webber, B. R. Matching nlo qcd computations and parton shower simulations. *JHEP* **2002**, 029 (2002). URL http://stacks.iop.org/1126-6708/2002/i=06/a=029. (Cited on page 39.)

[105] Corcella, G. *et al.* HERWIG 6: An Event generator for hadron emission reactions with interfering gluons (including supersymmetric processes). *JHEP* **0101**, 010 (2001). URL http://arxiv.org/abs/hep-ph/0011363. (Cited on page 39.)

[106] Corcella, G. *et al.* HERWIG 6.5 release note (2002). URL http://arxiv.org/abs/hep-ph/0210213. (Cited on page 39.)

[107] Czakon, M., Fiedler, P. & Mitov, A. The total top quark pair production cross-section at hadron colliders through $O(\alpha_S^4)$. *Phys.Rev.Lett.* **110**, 252004 (2013). URL http://arxiv.org/abs/1303.6254. (Cited on page 39.)

[108] Olschewski, M. W' and contact interaction background determination. *Talk from August 10, 2012* URL https://indico.cern.ch/contributionDisplay.py?confId=203021&contribId=5. (Cited on page 41.)

[109] Carloni Calame, C., Montagna, G., Nicrosini, O. & Treccani, M. Higher order QED corrections to W boson mass determination at hadron colliders. *Phys.Rev.* **D69**, 037301 (2004). URL http://arxiv.org/abs/hep-ph/0303102. (Cited on page 41.)

[110] Balossini, G. *et al.* Combination of electroweak and QCD corrections to single W production at the Fermilab Tevatron and the CERN LHC. *JHEP* **1001**, 013 (2010). URL http://arxiv.org/abs/0907.0276. (Cited on pages 41 and 63.)

[111] CMS Collaboration. PDF Uncertainties and K-factor for the W' search at 8 TeV collisions. *CMS Analysis Note* **AN-12-172** (2012). (Cited on page 43.)

[112] Erdweg, S. Study for Sensitivity for W' to tau nu with CMS. *Bachelor Thesis, RWTH Aachen* (2011). (Cited on page 43.)

[113] Alwall, J., Herquet, M., Maltoni, F., Mattelaer, O. & Stelzer, T. MadGraph 5 : Going Beyond. *JHEP* **1106**, 128 (2011). URL http://arxiv.org/abs/1106.0522. (Cited on page 45.)

[114] Hof, C. Detection of New Heavy Charged Gauge Bosons with the future CMS Detector. *Diploma Thesis, RWTH Aachen* (2005). (Cited on page 49.)

[115] CMS Collaboration - Physics Validation. Instruction of Pileup Reweighting methods. *TWiki* (2013). URL https://twiki.cern.ch/twiki/bin/view/CMS/PileupMCReweightingUtilities. (Cited on page 52.)

[116] CMS Collaboration - MuonPOG . Single Muon efficiencies in 2012 Data. *CMS Detector Performance Note* **DP-2013-009** (2013). URL http://cds.cern.ch/record/1536406?ln=en. (Cited on page 52.)

[117] CMS Collaboration. CMS Luminosity Based on Pixel Cluster Counting - Summer 2013 Update. *CMS Physics Analysis Summary* **LUM-13-001** (2013). URL http://cds.cern.ch/record/1598864?ln=en. (Cited on page 57.)

[118] CMS Collaboration - MuonPOG . Tag and Probe. *TWiki* (2013). URL https://twiki.cern.ch/twiki/bin/viewauth/CMS/MuonTagAndProbe. (Cited on page 57.)

[119] CMS Collaboration. ECAL 2010 performance results. *CMS Detector Performance Note* **DP-2011-008** (2011). URL http://cds.cern.ch/record/1373389?ln=en. (Cited on page 58.)

[120] CMS Collaboration. Tau identification in CMS. *CMS Physics Analysis Summary* **TAU-11-001** (2011). URL http://cds.cern.ch/record/1337004?ln=en. (Cited on page 58.)

[121] CMS Collaboration - JetMET Group. Official Prescription for calculating uncertainties on MET. *TWiki* (2013). URL https://twiki.cern.ch/twiki/bin/view/CMS/MissingETUncertaintyPrescription. (Cited on page 59.)

[122] CMS Collaboration - JetMET Group. Jet Energy Resolution Measurement. *TWiki* (2013). URL https://twiki.cern.ch/twiki/bin/view/CMS/JetResolution. (Cited on page 60.)

[123] CMS collaboration. Determination of jet energy calibration and transverse momentum resolution in cms. *Journal of Instrumentation* **6**, P11002 (2011). URL http://stacks.iop.org/1748-0221/6/i=11/a=P11002. (Cited on page 60.)

[124] Alekhin, S. *et al.* The PDF4LHC Working Group Interim Report (2011). URL http://arxiv.org/abs/1101.0536. (Cited on page 61.)

[125] CMS Collaboration - Physics Validation group. Utilities for accessing pileup information for data. URL https://twiki.cern.ch/twiki/bin/view/CMS/PileupJSONFileforData. (Cited on page 62.)

[126] Pook, T. Muon resolution uncertainty in ADD. *Talk from November 26, 2013* URL https://indico.cern.ch/conferenceDisplay.py?confId=285147. (Cited on page 62.)

[127] Brensing, S., Dittmaier, S., Kramer, ., Michael & Muck, A. Radiative corrections to W^- boson hadroproduction: Higher-order electroweak and supersymmetric effects. *Phys.Rev.* **D77**, 073006 (2008). URL http://arxiv.org/abs/0710.3309. (Cited on page 63.)

[128] CMS Collaboration. Measurement of Momentum Scale and Resolution of the CMS Detector using Low-mass Resonances and Cosmic Ray Muons. *CMS Physics Analysis Summary* **TRK-10-004** (2010). URL http://cds.cern.ch/record/1279137?ln=en. (Cited on pages 64 and 65.)

[129] CMS Collaboration. Combined results of searches for the standard model Higgs boson in pp collisions at s=7 TeV. *Physics Letters B* **710**, 26–48 (2012). URL http://arxiv.org/abs/1202.1488. (Cited on page 64.)

[130] RooStats Collaboration. RooStats. *TWiki* (2011). URL https://twiki.cern.ch/twiki/bin/view/CMS/RooStats. (Cited on page 64.)

[131] Cowan, G. PDG Review on statistics (chap. 33). *JPG 37* **075021** (2012). (Cited on page 65.)

[132] Kypreos, T. Endpoint Results with the latest alignment. *Talk from January 23, 2012* URL https://indico.cern.ch/getFile.py/access?contribId=3&resId=0&materialId=slides&confId=173674. (Cited on page 65.)

[133] Conway, J. S. Incorporating Nuisance Parameters in Likelihoods for Multisource Spectra (2011). URL http://arxiv.org/abs/1103.0354. (Cited on page 68.)

[134] Neal, R. M. Probabilistic Inference using Markov Chain Monte Carlo Methods. Tech. Rep. CRG-TR-93-1, Dept. of Computer Science, University of Toronto (1993). (Cited on page 68.)

[135] Aprile, E. *et al.* Dark Matter Results from 225 Live Days of XENON100 Data. *Phys.Rev.Lett.* **109**, 181301 (2012). URL http://arxiv.org/abs/1207.5988. (Cited on pages 73 and 75.)

[136] CDMS Collaboration. Silicon Detector Dark Matter Results from the Final Exposure of CDMS II. *Phys.Rev.Lett.* (2013). URL http://arxiv.org/abs/1304.4279. (Cited on pages 73 and 75.)

[137] Bai, Y., Fox, P. J. & Harnik, R. The Tevatron at the Frontier of Dark Matter Direct Detection. *JHEP* **1012**, 048 (2010). URL http://arxiv.org/abs/1005.3797. (Cited on page 73.)

[138] Belanger, G., Boudjema, F., Pukhov, A. & Semenov, A. Dark matter direct detection rate in a generic model with micrOMEGAs 2.2. *Comput.Phys.Commun.* **180**, 747–767 (2009). URL http://arxiv.org/abs/0803.2360. (Cited on pages 74 and 89.)

[139] Airapetian, A. *et al.* Precise determination of the spin structure function g(1) of the proton, deuteron and neutron. *Phys.Rev.* **D75**, 012007 (2007). URL http://arxiv.org/abs/hep-ex/0609039. (Cited on page 74.)

[140] Felizardo, M. *et al.* Recent results from the SIMPLE dark matter search. *J.Phys.Conf.Ser.* **375**, 012011 (2012). (Cited on page 75.)

[141] Aalseth, C. E. *et al.* Results from a Search for Light-Mass Dark Matter with a p-Type Point Contact Germanium Detector. *Phys. Rev. Lett.* **106**, 131301 (2011). URL http://link.aps.org/doi/10.1103/PhysRevLett.106.131301. (Cited on page 75.)

[142] KAMIOKANDE Collaboration. Search for neutralino dark matter in Kamiokande. *Phys.Rev.* **D48**, 5505–5518 (1993). (Cited on page 76.)

[143] Abbasi, R. *et al.* Limits on a Muon Flux from Neutralino Annihilations in the Sun with the IceCube 22-String Detector. *Phys. Rev. Lett.* **102**, 201302 (2009). URL http://link.aps.org/doi/10.1103/PhysRevLett.102.201302. (Cited on page 76.)

[144] Gondolo, P. & Gelmini, G. Cosmic abundances of stable particles: Improved analysis. *Nuclear Physics B* **360**, 145 – 179 (1991). (Cited on page 77.)

[145] Griest, K. & Seckel, D. Three exceptions in the calculation of relic abundances. *Phys. Rev. D* **43**, 3191–3203 (1991). (Cited on page 77.)

[146] CMS Collaboration. HEEP selection with impact parameter (dxy) and photon conversion rejection. *CMS Analysis Note* **AN-12-391** (2012). (Cited on page 88.)

DECLARATION

Hiermit versichere ich, Sören Erdweg, dass ich die Arbeit selbstständig verfasst und keine anderen als die angegebenen Quellen und Hilfsmittel benutzt, sowie Zitate kenntlich gemacht habe.

Aachen, December 2013

Sören Erdweg